

Dissertation

**submitted to the
Joint Faculties for Natural Sciences and Mathematics
of the Ruperta Carola University
of Heidelberg, Germany**

**for the degree of
Doctor of Natural Sciences**

**presented by
Dipl. Phys. Frederik Rühr
born in Coburg, Germany**

Oral Examination: 29. January 2009

TeV Jets at ATLAS

- A Probe for New Physics

Referees: Prof. Dr. Karlheinz Meier
Prof. Dr. Carlo Ewerz

TeV Jets bei ATLAS und die Suche nach neuer Physik

Die Erzeugung von Teilchenjets ist der dominante physikalische Prozess am Large Hadron Collider (LHC) und wird entweder als Signal oder Untergrund einen hohen Stellenwert für viele Analysen einnehmen. Aus diesem Grund ist die präzise Messung von Jets eine wichtige Voraussetzung für mögliche Entdeckungen jenseits des Standardmodells der Teilchenphysik. Der erste Teil dieser Arbeit stellt eine neue Methode vor, mit der die Jet-Energieskala im TeV Bereich bereits mit ersten ATLAS Daten kalibriert werden kann. Dabei wird der hohe Jet-Wirkungsquerschnitt für eine Interkalibration benutzt.

Das darauf folgende Thema ist die Überprüfung der Gültigkeit der Quantenchromodynamik mittels inklusiver Jet-Messungen. Mehrere Analyseansätze werden anhand von simulierten Daten vorgestellt. Zuerst dient dabei eine effektive Theorie einer inneren Quarkstruktur als Maß für die Sensitivität auf neue Physik. Abschließend wird ein weiteres Modell hinzugezogen, das mögliche Auswirkungen von Quantengravitation unter Berücksichtigung zusätzlicher Raumdimensionen beschreibt. Dies unterstreicht die Bedeutung der Messung von Jets als ein wichtiges Werkzeug zur Untersuchung der Quantenchromodynamik und neuer Physik.

TeV Jets at ATLAS - A Probe for New Physics

The production of particle jets will be the dominant process at the Large Hadron Collider (LHC), and jets will thus be the signal or define the environment of many analyses at the ATLAS experiment. Their precise measurement is a vital requirement for many potential discoveries of new physics beyond the Standard Model. The first part of this thesis introduces a new method to constrain and correct errors of the energy measurement of jets in the TeV regime. The emphasis is on a very high reach in transverse jet momenta even with earliest ATLAS data. This is achievable by an intercalibration utilizing the large inclusive jet production cross section.

In the second part inclusive jet measurements are used to probe the validity of Quantum Chromodynamics (QCD). Several analyses are presented and their sensitivity is estimated using simulated data of an effective theory of a possible quark substructure. The search is then extended to effects of quantum gravity that could emerge at the LHC in scenarios of new physics, demonstrating that inclusive jet measurements are a powerful tool to probe QCD and a broad range of new physics models.

Contents

1	Introduction	1
2	Physics at the TeV-Scale	3
2.1	The Standard Model of Particle Physics	3
2.1.1	The Higgs Mechanism	5
2.1.2	The Hierarchy Problem	6
2.2	Feynman Diagrams and Process Amplitudes	7
2.3	Beyond the Standard Model	8
2.3.1	Quark Compositeness	8
2.3.2	Large Extra Dimensions and Micro Black Holes	10
2.4	Summary	13
3	The ATLAS Experiment at the Large Hadron Collider	15
3.1	The Large Hadron Collider at CERN	15
3.2	The ATLAS Detector	17
3.2.1	Inner Detector	18
3.2.2	ATLAS Calorimetry	18
3.2.3	Muon System	21
3.2.4	The ATLAS Trigger System	22
4	Jets at ATLAS	27
4.1	Jet Production at the LHC	27
4.1.1	Hard Quark and Gluon Interactions	28
4.1.2	From Parton to Particle Level	32
4.2	Jet Measurement and Reconstruction at ATLAS	38
4.2.1	Jet Algorithms	40
4.2.2	Jet Calibration	42
4.2.3	The ATLAS Detector Simulation	46
4.3	Jet Performance and QCD Benchmarks	48
4.3.1	Jet Energy Scale and Resolution	50
4.3.2	Precision of the Jet Axis	52
4.3.3	Inclusive Jet Spectra	54
4.3.4	Jet Angular Measurements	56

4.4	Summary	58
5	In-Situ Jet Calibration at the Highest Momentum Scales	61
5.1	In-situ Studies using $\gamma/Z + \text{Jet}$ Events	63
5.2	Multi-Jet Bootstrapping	64
5.2.1	Introduction	64
5.2.2	Study of the p_T -Balance Bias	68
5.2.3	Systematic Effects and their Influence on Multi-Jet Bootstrapping	75
5.2.4	Multi-Jet Bootstrapping Applied and Expected Results	88
5.3	Dijet Bootstrapping	95
5.3.1	Dijet Bootstrapping Applied	98
5.4	Summary	102
6	Jets and Physics Beyond the Standard Model - Compositeness	105
6.1	Statistics Introduction	106
6.1.1	Confidence Levels	106
6.1.2	Summary	109
6.2	Quark Compositeness	110
6.2.1	Monte Carlo Data	111
6.3	Inclusive Jet Spectra	112
6.3.1	Λ -fit of jet spectra	113
6.3.2	Analysis Prototypes	114
6.3.3	Expected Exclusion Limits	122
6.4	Jet Angular Distributions	125
6.4.1	Fit of the Λ Dependence of χ Spectra	128
6.4.2	Comparison of Analysis Prototypes	129
6.4.3	Exclusion Limits Using Angular Distributions	134
6.5	Discovery Reach of the Analysis	143
6.5.1	Basic Strategy	143
6.5.2	$3\text{-}\sigma$ Evidence for Compositeness and Confidence Intervals	144
6.6	Summary of the Expected Sensitivity to Quark Compositeness	146
7	Quantum Gravitational Dijet Signatures	149
7.1	General Study	150
7.1.1	Theory and Monte Carlo	150
7.1.2	Exclusion Limits Based on Angular Distributions	153
7.1.3	Strategy for Experimental Data	157
7.1.4	Discovery Considerations	157
7.1.5	Comparison Using χ Based Analyses	158
7.1.6	Study of the p_T Spectrum	162
7.1.7	Alternative Approaches	162
7.1.8	Conclusions	163
7.2	Summary	163

8 Summary and Outlook	165
Bibliography	167
Acknowledgements	169

Chapter 1

Introduction

The motivation for scientific endeavors is often not only to gain knowledge, but also understanding. When the Standard Model of Particle Physics evolved in the 1960s it proved to be extremely successful to gain an insight into the world of elementary particles at extremely small scales. Its predictions were confirmed by experimental results one after the other. But the paradigm slowly changed. After the discovery of the bottom quark in 1977 eighteen years passed until the discovery of its partner, the top quark, at an unexpected mass. The last particle missing for the completion of the Standard Model, the Higgs Boson, still remains to be found, more than 40 years after its prediction.

Even if a single light Higgs is discovered, the predictive and explanatory power of the Standard Model is largely spent. The paradigm of our time is the discovery of new unexpected effects, like e.g. neutrino mixing or dark matter. While the Standard Model could be extended to encompass at least some of these observations due to its flexibility, these could as well be the first threads coming loose of the fabric of the Standard Model, soon tearing it down under the strain of new discoveries.

The notion that interesting times lie ahead in physics is further reinforced by the the fact that the Large Hadron Collider (LHC) at CERN is finally complete and first proton-proton collisions at an unprecedented center-of-mass energy of up to 14 TeV are not far-off anymore.

The first chapter of this thesis gives a short physics motivation, introducing the Standard Model and alternatives beyond it, e.g. the intriguing possibility to discover extra dimensions and micro black holes at the LHC. The second chapter describes the precision instruments required to expand our knowledge, the LHC and the ATLAS experiment. Afterwards a short review of the current knowledge about the hard scattering of partons in proton-proton collisions, leading to measurable particle jets, is given. In addition the simulation framework of ATLAS is described and a set of jet measurements to probe perturbative QCD is introduced.

One crucial problem of jet physics is to constrain the experimental uncertainty on the measurement of their transverse momenta. An error can easily lead to a mistaken discovery of new physics, or make the discovery of real new physics impossible. To span the large gap between the momentum scale that can be verified in-situ with proven methods, and the very high scale of jets that will be measured even in a very early stage of data taking at ATLAS, a new method is described, which was developed during the work for this thesis. Utilizing events with multiple jets, an inter-calibration between low and high scales can be performed.

Chapter 6 is focused on a precision test of perturbative QCD and the Standard Model, by searching for any deviations that could be caused by new physics. Hypothesis of a composite structure of quarks and the null hypothesis of known physics are used to describe a set of analyses to test the sensitivity of ATLAS to quark compositeness. Exclusion limits on compositeness, even for the first ATLAS data and including an estimate of all systematic effects, are expected to be at least by a factor of 2 higher than the current best results.

Chapter 7 extends the analyses to an effective model of quantum gravity and micro black holes in an extra dimensions scenario. While a similar signature makes it challenging to distinguish this model from quark compositeness in the case of an evidence for new physics, the analysis is found to be very sensitive to the onset of quantum gravity. The expected exclusion limits if no signal is found surpass the current knowledge by at least a factor of 4 even during early data taking at ATLAS.

The last chapter of this thesis provides a summary of developed methods and obtained results.

Chapter 2

Physics at the TeV-Scale

This chapter will introduce the Standard Model of Particle Physics, including known problems and common solutions. Furthermore two effective models for physics beyond the Standard Model are presented, which are used for analyses in this thesis.

Only short introductions of the topics in this chapter can be given in the framework of this thesis. Detailed information can e.g. be found in [1] for the standard model, [2] for Supersymmetry, and [3] for extra dimensions and micro black holes.

2.1 The Standard Model of Particle Physics

The Standard Model is a theory that describes all known elementary particles and their interactions. But it is not a complete theory of fundamental interactions as it does not include gravity. It still is a very successful theory, so far all tests of the three interactions described, strong, weak and electromagnetic, have confirmed its predictions with very high precision.

Generations			
	I	II	III
Quarks	up down	charm strange	top bottom
Leptons	ν_e e^-	ν_μ μ^-	ν_τ τ^-

Table 2.1: Fermions in the Standard Model

The particle content of the Standard Model can be split into fermions and bosons that mediate the interactions between them. Fermions are considered to be point-like particles with spin $\frac{1}{2}$ following the Pauli Exclusion Principle. The

fermions are further subdivided based on the charges they carry and thus their interactions. Quarks carry a color charge and are subject to the strong force, while all fermions without a color charge are leptons. Lastly they can be grouped into three generations, mainly distinguished by their masses. Fermions of the first generation are stable and form all “normal” matter directly observable in the universe. The reason for the existence of the other families is in principle unknown¹. Based on indirect evidence, they were predicted by the Standard Model though, and their discovery is one of its great successes.

The quarks are subject to all three forces, while the weak force is the only one acting on all leptons. As the electron, muon and tau carry an electric charge, they are additionally subject to the electromagnetic force, in contrast to the neutrinos. All fermions, listed in table 2.1, additionally have an anti-particle, which has the same mass and spin, but opposite charges.

Mathematically, the Standard Model is a local non-abelian gauge field theory, based on the symmetry group $SU(3) \times SU(2) \times U(1)$. $SU(3)$ is the symmetry group of the strong interaction of Quantum Chromodynamics (QCD). The quarks form color triplets and interact with an octet of gluons carrying two color charges. The QCD Lagrangian can be written as:

$$\mathcal{L}_{\text{QCD}} = \bar{\psi}_i (i\gamma^\mu \partial_\mu - m_i) \psi_i - g G_\mu^a \bar{\psi}_i \gamma^\mu T_{ij}^a \psi_j - \frac{1}{4} G_{\mu\nu}^a G_a^{\mu\nu} \quad (2.1)$$

where i indexes the quark flavors and a the color states of the gluon. $\psi_i(x)$ is the quark field, $G_\mu^a(x)$ are the gluon fields. The gluon field tensor is:

$$G_{\mu\nu}^a = \partial_\mu G_\nu^a - \partial_\nu G_\mu^a - gf^{abc} G_\mu^b G_\nu^c \quad (2.2)$$

where f^{abc} are structure constants, defined by the commutation relations of the group tensors T_{ij}^a . The quark masses are defined by m_i and g is the strong coupling. The Lagrangian includes kinetic terms of the quark and gluon fields, the color interaction and gluon self coupling.

The electromagnetic and weak force are unified into the electroweak interaction of the $SU(2) \times U(1)$ gauge group. $SU(2)$ introduces three vector fields W_μ^a and $U(1)$ the B_μ field. The physical W bosons are a linear combination of W_μ^1 and W_μ^2 :

$$W_\mu^\pm = \frac{1}{\sqrt{2}} (W_\mu^1 \mp iW_\mu^2) \quad (2.3)$$

while the neutral vector boson Z and the photon A are linear combinations of W_μ^3 and B_μ :

$$Z_\mu = W_\mu^3 \cos \theta_W - B_\mu \sin \theta_W \quad (2.4)$$

$$A_\mu = W_\mu^3 \sin \theta_W + B_\mu \cos \theta_W \quad (2.5)$$

¹I.I. Rabi on the discovery of the muon: ‘Who ordered that?’

where θ_W is the weak mixing angle.

Summarizing, gluons are massless mediators of the strong force, acting on all colored particles, including gluon self coupling. The massless photon mediates the electromagnetic force between particles with an electric charge. The massive W^\pm and Z bosons mediate weak interactions.

The coupling to a W^\pm introduces a complication. In principal it flips the weak isospin that defines the quark and lepton doublets of the three generations. Thus it turns e.g. a μ into a ν_μ . For leptons this seems to be limited to one generation, while for quarks flavor changing is observed. This can be explained by the quark isospin eigenstates not being exactly the same as the mass eigenstates.

The Cabibbo-Kobayashi-Maskawa matrix (CKM matrix) contains the information on the mismatch between the eigenstates:

$$\begin{pmatrix} V_{ud} & V_{us} & V_{ub} \\ V_{cd} & V_{cs} & V_{cb} \\ V_{td} & V_{ts} & V_{tb} \end{pmatrix} \begin{pmatrix} d \\ s \\ b \end{pmatrix} = \begin{pmatrix} d_w \\ s_w \\ b_w \end{pmatrix} \quad (2.6)$$

where d, s and b are the mass eigenstates and d_w , s_w and b_w the isospin eigenstates. The central values of its coefficients are at the time of writing [4]:

$$V_{ij} = \begin{pmatrix} 0.97419 & 0.2257 & 0.00359 \\ 0.2256 & 0.97334 & 0.0415 \\ 0.00874 & 0.0407 & 0.999133 \end{pmatrix} \quad (2.7)$$

While being very successful, the Standard Model also has shortcomings. Firstly it has 19 free parameters even in its simplest form. But more importantly there is the problem of electroweak symmetry breaking. The electroweak symmetry must be broken to allow the W and Z bosons to be massive in contrast to the massless photons and gluons. With an unbroken symmetry all bosons would be massless.

2.1.1 The Higgs Mechanism

The Higgs Mechanism is commonly used to solve the problem of masses in the framework of the Standard Model. The mechanism introduces a field with a nonzero vacuum expectation value, breaking the symmetry property of the vacuum state. The Higgs field is a complex spinor of the group SU(2):

$$\phi = \begin{pmatrix} \phi^+ \\ \phi^0 \end{pmatrix} \quad (2.8)$$

In order to ensure that the vacuum is electrically neutral, only the neutral component of the Higgs field is assigned a real nonzero vacuum expectation value:

$$\langle 0|\phi|0\rangle = \begin{pmatrix} 0 \\ v \end{pmatrix} \quad (2.9)$$

As an isospin doublet of two complex fields the Higgs field has four degrees of freedom. Three of these four degrees of freedom mix with the W^\pm and Z , giving them masses. So there is one degree of freedom left in the Higgs doublet, giving rise to the prediction of a new massive scalar particle, the Higgs boson.

The Higgs mechanism is a requirement for the validity of the Standard Model, and it is well motivated. But the predicted Higgs boson has not been found yet.

2.1.2 The Hierarchy Problem

One problem concerning the Higgs boson is often perceived to be the Hierarchy Problem. Precision measurements of the W and top mass favor a Higgs boson with a mass below 200 GeV. For unitarity considerations and thus the validity of the Standard Model at current collider experiments, the Higgs mass is required to be below 1 TeV.

But large correction terms due to radiative corrections enter into its mass term. The fermion coupling to the Higgs boson is proportional to their mass, resulting in the largest corrections coming from the heavy quarks:

$$\Delta m_H^2 = -\frac{|\lambda_f|^2}{8\pi^2} [\Lambda_{UV}^2 + \dots] \quad (2.10)$$

where λ_f is the coupling to the Higgs boson and Λ_{UV} the ultraviolet cutoff, up to which the Standard Model is valid.

If there is no new physics up to the Planck Scale ($M_{Pl} \sim 10^{16}$ TeV) these corrections are quadratically divergent. To keep the Higgs mass below 1 TeV counter-terms would need to be inserted by hand at each order of perturbation theory. The assumptions that this fine-tuning, the cancellation of all terms with a precision of $\sim (M_{Pl}/M_{EW})^2 \sim 10^{-32}$, is unnatural or very unlikely is called the hierarchy problem.

If one accepts fine-tuning as a problem, new physics in the order of the Higgs scale is required to provide a natural cut-off or compensation for the mass terms.

Supersymmetry The model of Supersymmetry (SUSY) is one of the best motivated theories to solve the hierarchy problem. It could additionally solve the mystery of Dark Matter in our universe, and the problem that the three forces of the Standard Model are not unified into a single field at high scales. Furthermore it is a feature of most string theories.

In SUSY each Standard Model particle has a supersymmetric partner that differs in spin by $1/2$. Thus every boson is related to a fermion and vice versa. Bosons have a positive contribution to the Higgs mass corrections and fermions a negative one. Unbroken Supersymmetry thus leads to an exact cancellation of the quadratically divergent corrections to the Higgs mass. However as no supersymmetric particles with the same masses as Standard Model particles have been found, SUSY must be broken as well. There is no natural way to break SUSY at the Higgs scale, giving rise to the Hierarchy Problem of SUSY breaking.

Extra Dimensions Another solution are models that include finite extra spatial dimensions. These can allow an actual fundamental Planck scale in the TeV range, while the observed Planck scale is a result of the weak gravitational interaction perceived at distances that are large with respect to the size of the extra dimensions. The fundamental Planck scale then provides a natural cut-off for the Higgs mass corrections terms. The possibility of extra spatial dimensions is discussed in more detail later in this chapter.

Other Alternatives Another alternative is to interpret the Standard Model as a low scale or large distance effective theory of new different physics models. In this case new physics beyond the Standard Model would ideally occur far below the Planck Scale to avoid the Hierarchy Problem.

In summary the Standard Model is one of the most successful models of modern physics, but is not complete yet. And even if a Higgs boson is discovered below 1 TeV one has to accept fine-tuning to prevent its eventual failure. On the verge of first collisions at the Large Hadron Collider, the basic question is if there is just a light Higgs boson to be discovered, or if the Standard Model will show more cracks, like the already observed neutrino mixing, and start to crumble.

2.2 Feynman Diagrams and Process Amplitudes

Before continuing to two models of new physics beyond the Standard Model, it is convenient to shortly introduce the formalism of Feynman diagrams and rules.

Feynman developed a method to calculate rates for processes in any quantum field theory. The Feynman diagrams are a shorthand to describe a calculation for one process of a fixed order of perturbation theory. Figure 2.1 shows a few sample diagrams for jet production in QCD at leading order. Vertical displacement represents particle motion, while horizontally from left to right time proceeds. The diagrams consist of points, called vertices, and lines attached to the vertices. In figure 2.1 solid lines with an arrow to the right are quarks, with an arrow to the left anti-quarks and curly lines are gluons.

Higher order diagrams for one process are obtained by adding additional quarks or gluons, either real emissions with the particle line ending externally, or virtual emissions introducing loops into the diagram. Another way to classify diagrams is to call all diagrams where the kinematics are uniquely defined by external lines tree-level diagrams, all others loop-diagrams.

The definition of the leading order of a process depends on the definition of the final state. The rightmost diagram in figure 2.1 e.g. is a leading-order diagram for three jet production, but also a next-to-leading order contribution to dijet production. The order of calculations and perturbative QCD will be covered in more detail in chapter 4.

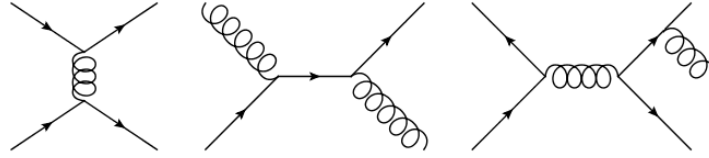


Figure 2.1: Examples of tree-level Feynman Diagrams for two and three jet production at a hadron collider

A crucial characteristic of Feynman Diagrams is that any given diagram has a definite amplitude. This amplitude can be calculated by the application of Feynman rules. Each vertex represents a factor from an interaction term of the Lagrangian, internal lines give a factor corresponding to a virtual particle's propagator while external lines carry energy and momentum. To obtain the total amplitude of a process, all possible diagrams for that process, to the desired order in perturbation theory, have to be added. Expected rates can be calculated from the absolute value of the total amplitude squared.

The Feynman rules for a given theory are very simple and can be derived from the Lagrangian, but increasingly complicated expressions result for higher order diagrams. One further complication is that there is an arbitrary momentum and energy flow in closed loops. In principal this leads to divergent results for the required integration over these parameters, making a renormalization necessary.

After renormalization, rates obtained with Feynman diagrams are in very good agreement to measurements.

2.3 Beyond the Standard Model

This section provides an introduction to two models of physics beyond the Standard Model. They were used in this thesis as a possible alternative to the null hypothesis of only Standard Model physics being present in data. Both Models represent an effective theory, meaning that they are no complete theory of new physics, but instead describe the onset of new physics close to the limit of pure QCD.

They were chosen as they result in a measurable change of inclusive jet cross sections, and jets are the focus of this thesis.

2.3.1 Quark Compositeness

A classical model resulting in a change of jet production cross sections is quark compositeness. The Standard Model does not predict the masses of fermions or the

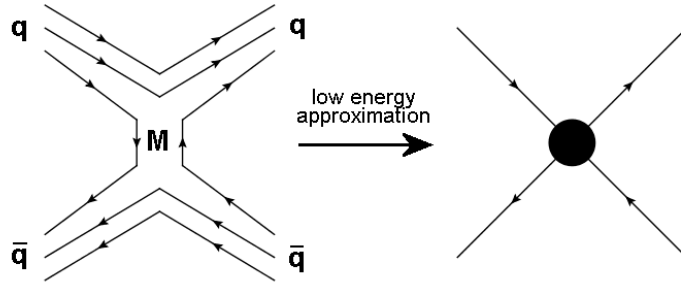


Figure 2.2: Simple sketch of a possible interaction between quark constituent and the approximation for $M < \Lambda$

number of their families, which follow a repetitive pattern. Furthermore the connection between electron and quark charges is not motivated and a large number of free parameters is required by the Standard Model.

The above may hint at a possible substructure and thus fermions being composite objects. The general approach of a substructure to simplify the classification of objects has been very successful in the past, e.g. concerning the structure of the atom, the next level of substructure of the atomic nuclei and lastly the partonic composition of hadrons.

There are many different models for compositeness, e.g. [5][6][7]. They commonly share the concept that if quarks and leptons consist of bound constituents, often named preons, new interactions should be measurable close to the scale of the binding energy, called Λ .

These new interactions can be described by an effective model, without a definition of their exact characteristics. This is done by a so-called four point interaction or contact interaction. For example a $2 \rightarrow 2$ process influenced by a new interaction between quarks is approximated by a single vertex where four lines meet if the center of mass energy of colliding particles $M < \Lambda$, as illustrated by figure 2.2.

For $M \ll \Lambda$ the new interaction is highly suppressed, and pure QCD jet production is observed. At the border between classical QCD behavior and the compositeness model the four-fermion interaction can be modeled by a Lagrangian \mathcal{L}_Λ :

$$\mathcal{L}_\Lambda = \frac{g^2}{2\Lambda^2} [\eta_{LL} (\bar{q}_L \gamma^\mu q_L) (\bar{q}_L \gamma_\mu q_L) + \eta_{RR} (\bar{q}_R \gamma^\mu q_R) (\bar{q}_R \gamma_\mu q_R) + 2\eta_{RL} (\bar{q}_R \gamma^\mu q_R) (\bar{q}_L \gamma_\mu q_L)] \quad (2.11)$$

The coefficients η_{ab} can be set to either 0, +1 or -1 to switch terms off or select their interference. A common choice is the left-left isoscalar model with destructive

interference, where $g^2 = 4\pi$ to indicate that the interaction is strong at Λ , and the η_{ab} coefficients are chosen to result in:

$$\mathcal{L}_{\Lambda_{LL}} = \frac{4\pi}{2\Lambda^2} (\bar{q}_L \gamma^\mu q_L) (\bar{q}_L \gamma_\mu q_L) \quad (2.12)$$

This effective Lagrangian is then added to the QCD Lagrangian:

$$\mathcal{L} = \mathcal{L}_{\text{QCD}} + \mathcal{L}_{\Lambda_{LL}} \quad (2.13)$$

The result are additional terms in a differential cross section $\frac{d\sigma}{dp_T}$, an interference term between the compositeness and QCD Lagrangian proportional to $\frac{1}{\Lambda^2}$ and a pure contact interaction term proportional to $\frac{1}{\Lambda^4}$. There are also additional terms in the differential cross section $\frac{d\sigma}{d\cos\theta^*}$, e.g.:

$$\frac{d\sigma_{q_i \bar{q}_i \rightarrow q_j \bar{q}_j}}{d\cos\theta^*} \sim \frac{1}{\Lambda^4} (1 + \cos\theta^*)^2 \quad i \neq j \quad (2.14)$$

In summary, a simple effective theory for an additional interaction between quarks is used. It is expected to result in a measurable difference to QCD jet production when the center of mass energy of the colliding partons approaches the compositeness scale Λ . The Monte Carlo samples which are introduced and used in chapter 6 of this thesis were obtained for a single specific effective model, assuming that only u and d quarks are composite, compositeness acts on left-handed particles only, and that the interference with QCD is destructive. Currently the best experimental limit on Λ_{qq} for quark-quark coupling in this model was obtained at the Tevatron, and excludes $\Lambda_{qq} < 2.7$ TeV with 95% confidence [8].

To introduce and describe the analyses in this thesis, only the above model and one effective model of the onset of quantum gravity were used exemplarily.

But the above framework can encompass a large number of models and concepts, though, and a search for compositeness is practically model independent. Looking for a difference of inclusive jet cross sections and QCD expectations is a very powerful tool to probe the general validity of QCD and the Standard Model, and parameter values of a large number of models can be excluded using experimental data.

2.3.2 Large Extra Dimensions and Micro Black Holes

Seen from a non-physicist point of view large extra dimensions are the most radical way to fix the hierarchy problem. Our everyday observation is that we are living in a world with three spatial dimensions. Hidden extra dimensions have long been only a topic of philosophy or science-fiction.

But the idea of finite extra dimensions reentered² the physics discussion with force about 30 years ago with the rise of string theory, which favors at least 6 extra dimensions. Unfortunately these extra dimensions would most likely be too small to be tested.

The ADD Model

This changed in 1998 when Arkani-Hamed, Dimopoulos and Dvali (ADD) [9] proposed that compactified extra dimensions could have a size of up to 1mm. Any force allowed to propagate into the extra dimensions would radically change its strength at distances smaller than the size of the extra dimensions. While the three forces described by the Standard Model are not allowed to propagate into the extra-dimensions, as they are experimentally tested to very small scales, there are no such limits for gravity. One consequence is that the observed Planck scale $M_{\text{Pl}} = \frac{1}{G_N} \sim 10^{16}$ TeV, a result of the small gravitational constant G_N measured at large distances and in three dimensions, is not the fundamental Planck Scale, termed M_D . The fundamental Planck scale could be as low as 1 TeV, and thus provides a natural cutoff scale for the Standard Model and solves the Hierarchy Problem.

But similarly to Supersymmetry the Hierarchy Problem is not fully negated. It is traded for a hierarchy of distances, of the electroweak symmetry breaking range $\sim 10^{-19}m$ to the much larger size of the extra dimensions. It is still a very compelling concept, and the currently unknown mechanisms of quantum gravity could explain the hierarchy of distances.

Micro Black Holes

One consequence of a Planck Scale M_D in the TeV regime is the possibility to produce black holes at particle accelerators. It is expected that this black hole production rapidly turns on close to M_D , providing a clear signal. Using semi-classical reasoning, a micro black hole is expected to be produced if two colliding particles come closer to each other than the Schwarzschild radius R_S given by their center of mass energy:

$$R_S = \frac{1}{\sqrt{\pi}M_D} \left[\frac{M_{\text{BH}}}{M_D} \frac{8\Gamma(\frac{n+3}{2})}{n+2} \right]^{\frac{1}{n+1}} \quad (2.15)$$

where M_{BH} is the mass of the black hole and n the number of extra dimensions [3]. Strictly seen the above is only valid for $M_{\text{BH}} \gg M_D$. In the limit of $M_{\text{BH}} \rightarrow M_D$ quantum gravity is expected to play a large role, and the semi-classical approach may be wrong.

²After the attempted unification of electromagnetism and general relativity via a fifth, spatial dimension by T. Kaluza and O. Klein in the 1920s

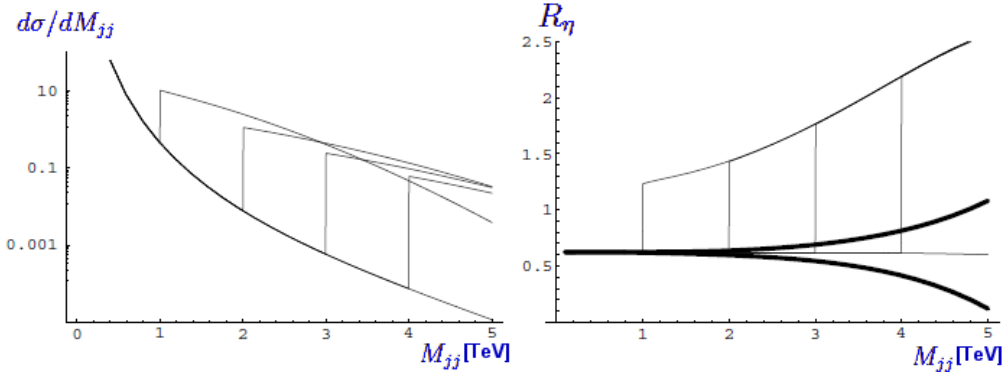


Figure 2.3: In the left plot $d\sigma/dM_{jj}$ is shown for the case of SM QCD background and a $n=6$ ADD model “black hole” behavior with $M_D = M_{BL} = 1, 2, 3$ and 4 TeV. The plot to the right shows the jet angular distribution using the ratio R_η of events, $R_\eta = [N_{events}(0 < |\eta| < 0.5)]/[N_{events}(0.5 < |\eta| < 1)]$ [10]

The black hole production cross section on parton level is considered to be purely geometrical:

$$\sigma(M_{BH}) \approx \pi R_S^2 \quad (2.16)$$

The expectation for such a semi-classical micro black hole is a decay via Hawking Radiation into a large number of isotropically distributed particles. This leads to spherical high energy and high multiplicity events in the detector that are believed to be impossible to miss, sometimes termed fireball events.

Dijet Black Holes and Quantum Gravity

A radically different paradigm concerning micro black hole decays was developed by Patrick Meade and Risa Randall and published in 2007 [10]. It is first argued that thermal black holes with a semi-classical behavior are highly suppressed and will occur only in a very limited parameter range of the models, if at all. Additionally if they are produced they are very unlikely to decay into a large numbers of particle. The number of emitted particles is only expected to be above 2 for black holes with $M_{BH} \geq 1.5M_D$. Due to the rapid fall of the total production cross section, caused by the rapidly falling chance to find partons with a high enough fraction of the protons momentum, most black holes are expected to be produced close to their production threshold, which is assumed to be M_D .

On the other hand a large excess of $2 \rightarrow 2$ scattering processes at the threshold is expected. As physics close to M_D is dominated by quantum gravity, the term micro black hole is treated more loosely as any quantum gravity effect or resonance.

n	M_D [TeV]		
	LEP	CDF	D0
2	1.60	1.18	0.884
3	1.20	0.99	0.864
4	0.94	0.91	0.836
5	0.77	0.86	0.820
6	0.66	0.83	0.797
7	-	-	0.797
8	-	-	0.797

Table 2.2: Lower limits on M_D at the 95% confidence level [11]

Figure 2.3 shows predicted spectra of the dijet invariant mass and an angular distribution.

In principle the framework and predictions are that of an effective theory of quantum gravity, treated similarly to a contact interaction like compositeness. The recommendation is thus to e.g. use compositeness-type analysis to look for quantum gravitational effects.

Experimental Limits

The current exclusion limits on the parameter M_D for n extra dimensions derived from accelerator experiments are shown in table 2.2 [11].

2.4 Summary

A short introduction to the Standard Model of Particles was provided. While it is a very successful theory the final particle predicted by it, the Higgs Boson, has still evaded discovery. Furthermore even if a light Higgs Boson is discovered at the LHC or Tevatron, the number of free parameters, the missing explanatory power, together with the Hierarchy problem and the exclusion of gravity strongly suggest that the Standard Model is not the final theory of particle physics.

The possible simplification of the Standard Model by the introduction of a quark substructure was shortly discussed. In this thesis the effective model given is treated more as a general approach to study possible deviations from perturbative QCD and the Standard Model than a complete theory, though. A search for compositeness-type signals in inclusive jet spectra is a precision test of QCD, and sensitive to a wide range of physics beyond the Standard Model. One radically different approach, an enhancement of the cross section of $2 \rightarrow 2$ parton interactions caused by quantum gravitational effects was sketched as an example.

The following chapters first provide the groundwork for jet physics and studies at the LHC and then present a new method to calibrate jets of the highest

momenta, which could be vital for many physics analyses at ATLAS.

Lastly, concluding this thesis, the effective models of quark compositeness and quantum gravity are used as hypotheses to present analyses based on inclusive jet production, building on all previous chapters.

Chapter 3

The ATLAS Experiment at the Large Hadron Collider

3.1 The Large Hadron Collider at CERN

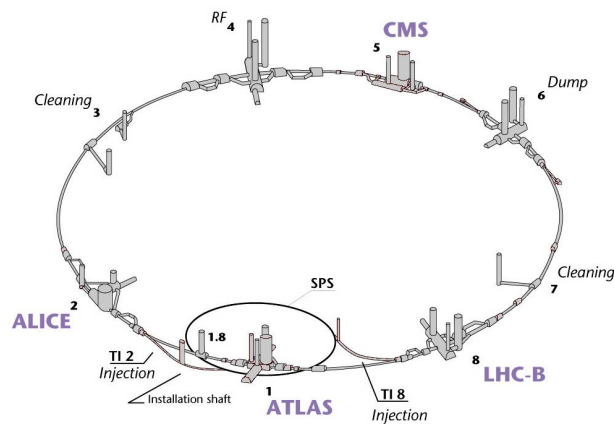


Figure 3.1: Sketch of the LHC, including access points

The Large Hadron Collider (LHC), built into the former LEP tunnel at the European Organization for Nuclear Research (CERN) site near Geneva, Switzerland, is an accelerator which will primarily¹ bring protons to head-on collisions at very high energies.

Bunches of protons, each containing about 10^{11} particles, are accelerated and stored in two separate counter-rotating circular beams, reaching an energy of up to 7 TeV each. Collisions occur at four interaction points, where the beam-lines

¹additionally heavy-ion(Pb) operation is foreseen

cross. The general purpose experiments ATLAS² and CMS³ occupy two of these points, ALICE⁴ and LHCb⁵ the other two.

In order to allow for a large discovery potential of these experiments, a high energy in the center-of-mass system is needed. With a planned proton energy of 7 TeV, the center-of-mass energy \sqrt{s} available in the proton-proton frame is 14 TeV. Only a part of this energy can be used to e.g. create new particles, though, as hard interactions take place between the protons' constituents, each carrying only a fraction of the proton energy. In contrast to e.g. electron-positron colliders the limiting factor of the beam energy is the ability to keep the particles on track. The inventive superconducting dipole magnets of the LHC beam line, with magnetic field strength up to 8.3 T, are one of the major engineering challenges of the project.

In order to get a high rate of interesting physics events and thus to utilize the discovery potential a high luminosity, the number of particles crossing a unit area per time, is essential. One way to achieve this goal are tight proton bunches with a large number of particles. But certain limits exist, like the repulsive force between protons, widening the bunches e.g. at the interaction points where the particle density is exceptionally high to achieve a high interaction rate. Thus to achieve the luminosity goals of the LHC, ranging from a luminosity of $\mathcal{L} = 10^{31} \text{cm}^{-2} \text{s}^{-1}$ for the very early operational phase, with the goal to increase it by a factor of $\sim 10^3$ in the long-term, a high number of bunches in the beam is required. Roughly three thousand⁶ bunches are stored, together with the speed of the protons being practically the speed of light and the circumference of 27km resulting in collisions occurring with a frequency of 40 MHz. Simultaneous passage of two bunches at an interaction point, occurring about every 25ns respectively, is called a bunch-crossing. The luminosity can be written as:

$$\mathcal{L} = fn \frac{N_1 N_2}{A} \quad (3.1)$$

where f is the revolution frequency, the N_i are the number of particles in each bunch, n the number of bunches in one beam and A the cross section of the beams at the interaction points. In addition to the unit $\text{cm}^{-2} \text{s}^{-1}$ it is useful to express the luminosity in $b^{-1} \text{s}^{-1}$, where one barn b is 10^{-28}m^2 . The so-called integrated luminosity is defined as:

$$\int \mathcal{L} dt \quad (3.2)$$

with the unit being b^{-1} . Cross sections σ for processes are often given as a fraction of a barn.

²A Toroidal LHC Apparatus

³Compact Muon Solenoid

⁴A Large Ion Collider Experiment

⁵Study of B-meson decays at the LHC

⁶plus 600 empty bunches due to the LHC filling process

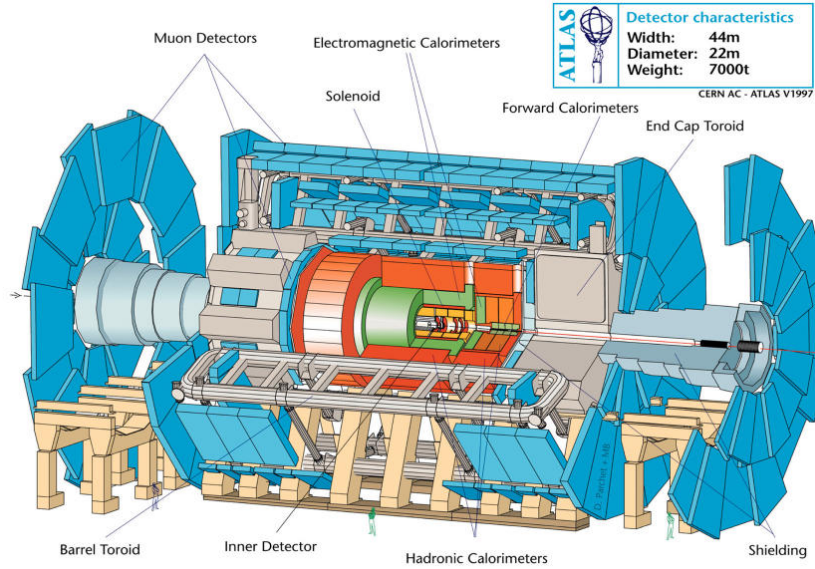


Figure 3.2: Schematic of the ATLAS detector

Thus the number N of expected events for a sample of data corresponding to a certain integrated luminosity is e.g.:

$$\frac{dN}{dp_T} = \frac{d\sigma}{dp_T} \int \mathcal{L} dt \quad (3.3)$$

As an example the expected total cross section for inclusive jet production with jet transverse momenta above 1.12 TeV is approximately 5.3 pb. A sample of for example 100 pb^{-1} of integrated luminosity is thus expected to result in 530 events.

At the design luminosity of $\mathcal{L} = 10^{34} \text{ cm}^{-2} \text{ s}^{-1}$ an average of 23 proton-proton interactions will take place in each bunch-crossing every 25 ns. This results in up to 10.000 tracks observed within 100ns, which is the typical duration of electronic signals in the detectors. One challenge of the LHC experiments is to identify and select the interesting physics events on top of this so-called "pileup" background. High granularity of the detectors, fast signals and powerful trigger systems are required for this task.

3.2 The ATLAS Detector

ATLAS is a general purpose experiment at the LHC, built by a collaboration of 165 institutes and more than 2000 physicists. ATLAS is designed to cover a large spectrum of LHC physics, e.g. searches for the Higgs Boson, supersymmetric particles, leptoquarks, and quark and lepton compositeness indicating extensions to the

Standard Model and new physics beyond it. But also high precision measurements of perturbative QCD and Standard Model parameters have a high priority.

The ATLAS approach to LHC measurements is a very precise electromagnetic calorimetry complemented by a full coverage hadronic calorimeter, high precision muon momentum measurements with an air-core toroid muon spectrometer and an efficient tracking system. The large acceptance in pseudorapidity η ⁷ with full coverage of the azimuthal angle ϕ and a very powerful, highly efficient trigger system provide high efficiencies for most interesting physics events at the LHC.

3.2.1 Inner Detector

Surrounded by a solenoid magnet with an axial magnetic field of 2 T, the inner detector's tasks are to reconstruct tracks and vertices of charged particles with a high efficiency and precision, as well as to provide information for particle identification. The inner detector consists of three layers and covers the range from $\eta = -2.5$ to $\eta = 2.5$.

Semiconductor pixel detectors form the innermost layer closest to the interaction point, their very high resolution allowing to determine whether a track originates from the primary proton-proton collision or from subsequent a decay process following it. The next layer consists of silicon microstrip detectors and supplements the track reconstruction with further high precision space points. In the outermost layer closest to the Calorimetry the Transition Radiation Tracker, a continuous straw tube detector, provides data for robust pattern reconstruction and particle identification.

The Inner Detector as a whole has to be radiation hard and provide a good spatial resolution, while having the smallest amount of material possible. Any detector material deteriorates its own momentum resolution and the energy measurement in the calorimeters.

3.2.2 ATLAS Calorimetry

The ATLAS calorimetry approach is twofold, matching its goals as a general purpose detector. An electromagnetic calorimeter is used for electron and photon identification and measurements, supplemented by a hadronic calorimeter for precise jet, isolated hadron and missing transverse energy measurements. Both calorimeters have 'barrel'⁸ sections to cover the central η region, as well as 'end-cap' modules for the high η regions to reach a very good coverage of up to $\eta = 3.2$. Forward calorimeters close to the beam line, in an extremely intense radiation environment, extend that coverage even further to η up to 4.9.

Due to the pileup caused by the high event rate, a fine granularity as well as a fast response are vital for all calorimeters, as they are a key component for many measurements in interesting physics channels. Given the high particle flux,

⁷defined as $-\ln \tan \frac{\theta}{2}$, where θ is the angle between an outgoing particle and the beam

⁸cylindrically shaped around the beam line

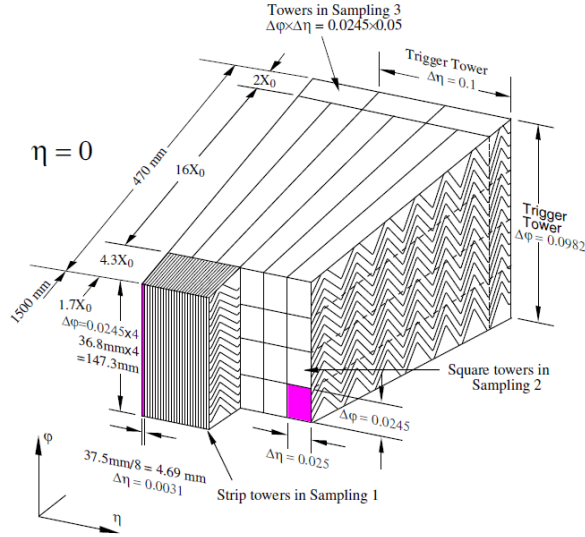


Figure 3.3: Sketch of the geometry of a barrel module of the electromagnetic calorimeter[12]

radiation hardness is also an issue and is achieved by detector modules with various approaches tailored to the local geometry and requirements.

The principal concept of calorimetry is that high energy particles cause a growing cascade of secondary particles by ionization, called a shower. During the progression of a shower the number of particles and the shower width increase, while the average energy per particle decreases, until a cutoff energy scale is reached where other losses start to outweigh the ionization losses and stop the cascade.

Electromagnetic Calorimeter

The electromagnetic calorimeter is a heterogeneous shower counter, also called a sampling calorimeter. Layers of passive and active material alternate. The passive or absorption material is used as a dense target for particles transversing the calorimeter, leading to the creation of showers. The active material samples a fraction of these showers to allow a deduction of the energy deposited in the calorimeter. The basic approach of the electromagnetic calorimeter is the use of liquid Argon (LAr) as sensitive material and lead as absorber material, resulting in an intrinsic radiation resistance. To achieve a seamless ϕ coverage, the electromagnetic barrel and end-cap calorimeters have an "accordion" structure, formed by stacked zigzag shaped lead absorbers with LAr gaps and an electrode structure in between, as shown on figure 3.3. The calorimeter includes a presampler to estimate the energy loss in the dead material of the cryostat and solenoid magnet in

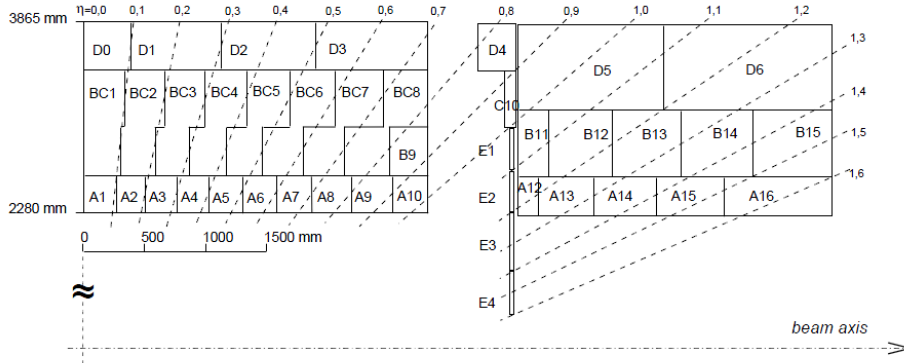


Figure 3.4: Segmentation in depth and η of the tile-calorimeter modules in the central (left) and extended (right) barrels. The bottom of the picture corresponds to the inner radius of the tile calorimeter [12].

front of it.

The total thickness of the electromagnetic calorimeter is 25 radiation lengths X_0^9 , thus containing the majority of the electron/photon energy. The total number of channels is of the order of 200,000.

Hadronic Calorimeter

For the detection and measurement of hadrons, which often pass through the electromagnetic calorimeter, it is surrounded by the hadronic calorimeter. Taking local requirements into account, this calorimeter uses different technologies in the barrel and end-cap regions. The barrel region is covered by the so-called TileCal barrel and two TileCal extended barrels, as shown in figure 3.4. These are analogously built sampling calorimeters with scintillating tiles embedded in an iron absorber matrix.

The Hadronic End Cap calorimeter makes use of the same LAr technology as the Electromagnetic Calorimeter, but copper instead of lead as absorbing material. The total amount of channels in the hadronic calorimeter is $\sim 21,000$.

Forward Calorimeter

The Forward LAr Calorimeter, closest to the beam line and thus exposed to an extreme particle flux, is built using a metallic tube and rod electrode structure embedded in copper for the inner section and tungsten otherwise, with a very small LAr gap. It covers the full ϕ range and $3.2 \leq |\eta| \leq 4.9$. The Forward

⁹ X_0 is the thickness of material over which electron energy is reduced to a fraction of $1/e$

Calorimeter is both used for electron/photon and isolated hadron/jet detection and measurements, and has about 11,000 readout channels.

Non-compensation and Response

The response of the calorimeter is defined as the ratio of average calorimeter signal to the energy of the particle having deposited that energy. The ATLAS calorimetry is called non-compensating, as the response to electromagnetic and hadronic showers differs by about 30%. As the composition of a jet is statistical in nature, and thus the ratio of electromagnetic to hadronic showers caused by a jet is not constant, the jet response is not constant either, and its average value requires a calibration. This topic is revisited later in the context of jet measurement.

Calorimeter Calibration Systems

The ATLAS calorimeters feature a built in calibration system adapted to the respective calorimeter type. In the case of LAr calorimeters, where the resulting signal is a direct measurement of the ionization charge, the calibration system consists of a charge injection system. The aim is to regularly calibrate the calorimeter using charge injection to a precision of 0.25% [12].

The hadronic TileCal calorimeters have the complication that the signal consists of photons from the scintillating tiles. While they also have a charge injection system at the readout stage, there are two factors that are expected to degrade with time, but cannot be calibrated using that system. Firstly the photon yield of the scintillating tiles, and secondly the response of the photomultiplier tubes to convert this signal to a charge. Hence to calibrate the response, two additional calibration systems are used:

- A laser system to calibrate the photomultipliers
- A calibration system using caesium sources to calibrate the photon yield of the tiles

The goal for the cell-to-cell linearity calibrated using the above systems is 3%.

3.2.3 Muon System

The outer frame of the ATLAS detector is dominated by the muon spectrometer, including its huge superconducting air-core toroid magnets. To utilize the promising discovery potential of physics channels with high energy final state muons,¹⁰ precise muon measurements and triggers are needed.

¹⁰f.e. the Higgs decay $H \rightarrow ZZ^* \rightarrow 4\mu$

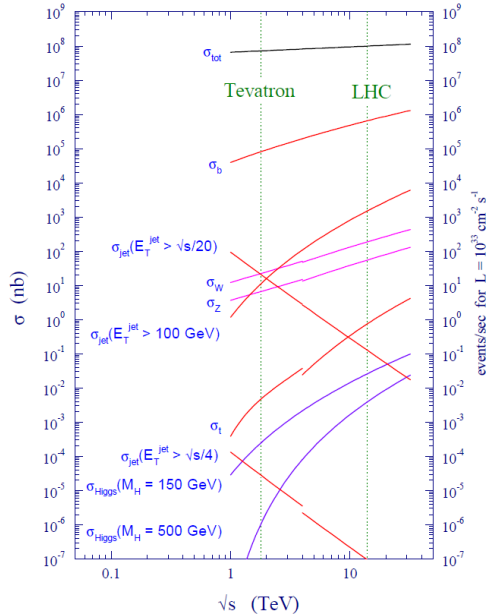


Figure 3.5: Standard Model cross sections at the Tevatron and LHC colliders. [13]

The strong toroidal magnetic field curves the muon tracks allowing to measure their energy and charge. This is done using Cathode Strip Chambers in the endcaps, where the radiation levels are high, and with Monitored Drift Tubes in the barrel region. Further coordinate measurements for track reconstruction and muon triggering is provided by Resistive Plate Chambers in the barrel and Thin Gap Chambers in the endcaps.

3.2.4 The ATLAS Trigger System

Trigger Challenges

As the production cross sections of the interesting processes are minuscule compared to the total inelastic cross section of the LHC, as shown on figure 3.5, there are stringent requirements for the trigger.

The rate of inelastic proton-proton interactions at the LHC at high design luminosity is of the order of 1 GHz, and the input rate of the trigger is 40 MHz, the bunch-crossing frequency. The difference of these two numbers results from the average number of events per bunch-crossing being significantly larger than 1 (~ 23 at high luminosity).

Events can only be stored at a rate of the order of 10^2 Hz, still resulting in huge amounts of data as one event is about 1.5 MByte in size. As a consequence the trigger has to lower the event rate by about seven orders of magnitude.

The ATLAS trigger system is designed to overcome two major challenges. The

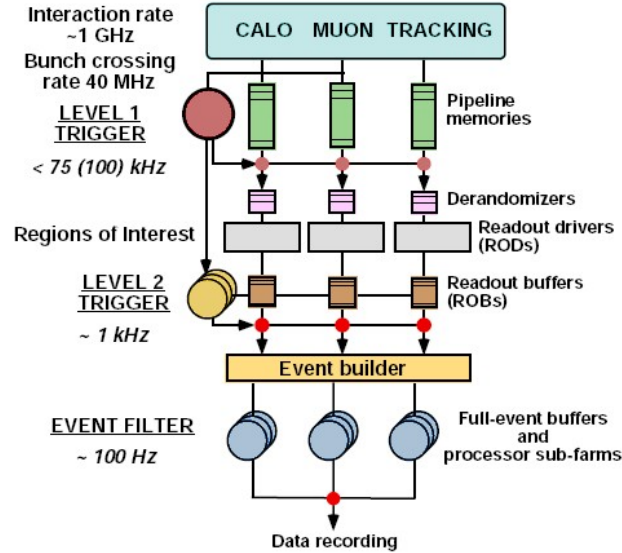


Figure 3.6: Block diagram of the ATLAS Trigger/DAQ system[14]

first requirement is an excellent efficiency, reducing the event rate by seven orders of magnitude. The second one is a low latency. As only the events tagged for final storage can be saved on disk, the detector readout has to be temporarily stored in buffers during the decision taking of the trigger. The total buffer size is limited and thus the time available to reach a decision is restricted.

ATLAS copes with these challenges with a three-level trigger and data acquisition system. At the first level a hardware trigger achieves a huge reduction in event rate in a very short time, searching locally for signatures of high energy muons, electrons, photons, jets and isolated hadrons as well as global trigger objects like missing and total transverse energy. The second level trigger selects candidates for interesting physics events based on the detector readout of regions of interest supplied by the first level, while at the third level an event filter accesses full event data comparable to an offline event reconstruction and analysis.

Overview of the Trigger System

Level-1 Trigger

The first level trigger significantly reduces the event rate to less than 100kHz. It searches for trigger objects hinting at interesting physics events, e.g. high energy lepton, jet or isolated hadron candidates, using calorimeter and muon system data. These objects are identified locally and then global multiplicities of found objects are determined. Additionally some large trigger objects like total transverse energy (E_T^{total}) and missing transverse Energy (E_T^{miss}) in the calorimeters

are computed. By comparing all this data to a trigger menu a decision is made whether to keep an event. If the decision is positive the full event is read from the on-detector pipeline memories and buffered in the data acquisition system. Event data not read out in time is automatically lost.

The Level-1 Trigger consists of three subsystems: the Calorimeter Trigger, the Muon Trigger and the Central Trigger Processor.

Level-1 Calorimeter Trigger

The Level-1 Calorimeter Trigger receives analog input from all ATLAS calorimeters. As about 230,000 channels are provided, the granularity has to be reduced to be able to build a feasible system. Up to 60 calorimeter channels are summed into projective towers called trigger towers, resulting in ~ 7200 trigger input channels with a typical granularity of 0.1×0.1 in $\eta \times \phi$.

The trigger tower signals are digitized in the Pre-Processor which then determines the transverse energy E_T and assigns it to the correct bunch crossing. Afterwards a subsystem called Cluster Processor searches for local energy deposition hinting at high- E_T electrons/photons and hadrons/taus, while a second subsystem, the Jet/Energy-Sum Processor, looks for high- E_T jets and computes the E_T^{miss} vector and total scalar E_T .

All object candidates and the global E_T sums are compared to thresholds (e.g. jets with $E_T > 90\text{GeV}$), and the numbers of trigger objects passing these thresholds are sent to the Central Trigger Processor. In the case that the event is selected the objects and their coordinates are sent to Level-2 of the trigger.

Level-1 Muon Trigger

The muon trigger receives precise and fast information about hits in the muon trigger chambers, which are Resistive Plate Chambers in the barrel region of the detector and Thin Gap Chambers in the end-caps. As more than 800,000 input channels are generated, only a part of the muon trigger is located in the trigger cavern, whereas the rest is built into front-end electronics on the detector to reduce the number of transmitted channels and thus the amount of cabling.

Mirroring the use of the different detector types in the barrel and end-cap regions, the muon trigger is divided into two parallel subsystems. Both search for hit patterns indicating high- p_T muons originating from the interaction region.

A third subsystem bundles and combines the data from the two triggers and acts as an interface to the Central Trigger Processor. In the case that an event is accepted muon coordinates are sent to the Level-2 Trigger.

Central Trigger Processor

The Central Trigger Processor(CTP) receives the multiplicities of muons, electron/photon, hadron/tau and jet candidates passing the thresholds in the other processors, plus the thresholds passed by the global E_T sums and combines this

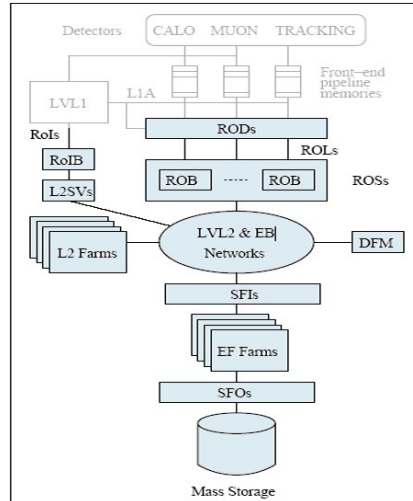


Figure 3.7: Principal components of the High Level Trigger and DAQ[15]

information in order to reach an overall Level-1 decision. The decision is made by comparing the input data to a trigger menu, which consists of up to 96 so called trigger items. Each of these trigger items can be a combination of different inputs, e.g. one muon with $p_T > 10\text{GeV}$ together with an isolated electron/photon candidate with $E_T > 15\text{GeV}$.

If any trigger item is matched by the data an event is in principle selected, though different trigger items can be individually scaled down to lower trigger rates, selecting only a fraction of events passing the criteria.

If an event is accepted by the CTP, a readout of the full event data from the on detector pipeline buffers is initialized, and the data is transmitted to the data acquisition system.

High Level Trigger

High Level Trigger is a collective name for the Level-2 (LVL2) trigger and the event filter (EF). Both are software triggers running on computer clusters and are an integral part of the Data Acquisition(DAQ) system. They differ in their approach, though, to achieve maximum combined efficiency. LVL2 uses fast, limited precision algorithms with a high rejection factor needing only modest computing power. Consequently it is able to concurrently process events with a high rate. The limitation of the LVL2 trigger is that it accesses the full detector data only around the candidate object provided by the Level-1 Trigger due to bandwidth restriction, the use of e.g. global parameters like missing transverse energy is not possible.

The event filter applies high precision algorithms on the full event data, using more extensive computing resources, and thus only being able to operate with a much lower rate. The algorithms used by the EF closely resemble the offline event

reconstruction and basic event analysis tools.

Chapter 4

Jets at ATLAS

The previous chapters introduced basic concepts and models of physics at the Terascale, as well as the LHC proton-proton collider and the ATLAS experiment. Before moving on to detailed studies of jets the principles of production and measurement of jets are introduced.

Underlying principles of Quantum Chromodynamics (QCD) and hard interactions between proton constituents, the quarks and gluon, are established first. Afterwards the connection between final-state partons and particle jets is studied.

The signatures left by particle jets in the detector, their measurement and necessary algorithms to make deductions from these signatures back to the particle level is discussed next. One vital ingredient is the calibration of jets, as the energy depositions measured by ATLAS do not easily allow to infer jet characteristics.

No experimental data of proton-proton collisions at the LHC is available yet, but to optimize the above procedures and be prepared for first data accurate expectations including the detector performance are necessary. While particle jets can be generated using Monte Carlo techniques, a simulation of the ATLAS detector is required. The two approaches used at ATLAS are introduced, a full simulation of the detector done to best knowledge and a fast parametrization of its attributes for high statistics event samples.

Using data samples thus generated and simulated, the expected performance of ATLAS with respect to the measurement of jets can be studied. Lastly a number of common jet measurements is presented.

4.1 Jet Production at the LHC

While the LHC is a proton-proton collider the main interest lies in interactions of the proton constituents, the quarks and gluons. Any scattering of these partons can be classified as either hard or soft. The theory to describe both these types of interactions is Quantum Chromodynamics, but there is a vital difference in our understanding of these two types. Hard scattering processes are generally rare events with a large momentum transfer, e.g. the production of jets with high

transverse momenta p_T or Higgs production. The coupling constant α_s of the strong interaction can be written as:

$$\alpha_s(Q^2) = \frac{12\pi}{(11N_c - 2N_f)\ln(\frac{Q^2}{\Lambda^2})} \left(1 + \mathcal{O}(\alpha_s^2)\right) \quad (4.1)$$

where $N_c = 3$ is the number of color charges and N_f the number of quark flavors with a mass less than the squared momentum transfer Q^2 ¹, and Λ is the QCD scale of the order of 10^2 MeV. For hard interactions Q^2 is significantly above Λ and α_s is small. Hence at high momentum scales interacting quarks and gluons can be considered to be quasi-free particles. This is called asymptotic freedom. The small α_s allows the use of perturbation theory to describe parton interactions. This means that a process is studied at leading order (LO) of α_s first and then perturbations representing a disturbance of the system can be added, of higher orders of α_s , e.g. the next-to-leading order (NLO). The calculation of a simple process at LO or NLO is already expected to be a good approximation. As a result perturbative QCD allows to describe the rates and properties of hard parton interactions with good precision.

For scales closer to Λ the coupling α_s becomes large, and terms of a higher order of α_s can not be treated as small perturbations anymore. Thus soft interactions are dominated by non-perturbative QCD effects and therefore significantly less understood. While hard parton scatterings are the sought after events, soft processes are an important part of the environment of a hadron collider. They are the bulk of interactions happening and contribute to hard processes e.g. by the scattering of additional partons of the incident protons.

Before discussing these effects the framework of perturbative QCD will be described.

4.1.1 Hard Quark and Gluon Interactions

First experimental evidence for the existence of proton constituents was found in 1968, in high energy interactions of electrons and protons, termed Deep Inelastic Scattering (DIS), at the Stanford Linear Accelerator Center. At sufficiently high energy scales points of charge were found inside the proton, termed partons by Feynman[16]. Their point-like nature was established by the so-called ‘‘Bjorken-scaling’’, that the inelastic cross section is independent of the momentum transfer Q^2 , and instead only significantly changes with the variable x :

$$x = \frac{Q^2}{2Pq} \quad (4.2)$$

¹e.g. $N_f = 5$ to 6 at the TeV scale, $N_f = 4$ below the bottom production threshold

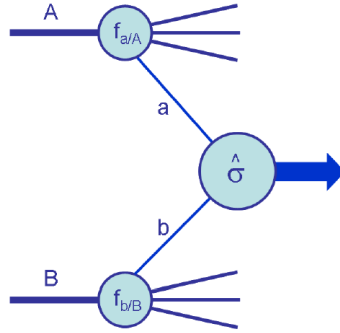


Figure 4.1: Diagram of a generic hard scattering process. [13]

where P is the four-momentum of the proton and q is the four-momentum of the virtual photon that is exchanged. The discovered partons were later identified with the quarks that had been independently proposed by Gell-Mann[17] and Zweig[18] in 1964 as a classification scheme for hadrons.

To describe the knowledge gained about the structure of the proton via DIS, parton distribution functions (PDF) are used. Drell and Yan[19] were the first to propose that these PDFs can also be applied to hadron-hadron collisions, sketched in figure 4.1. They postulated that the hadronic cross section of $\sigma(AB \rightarrow \mu^+\mu^- + X)$, thus named Drell-Yan process, can be predicted by weighting the cross section $\hat{\sigma}$ for $q\bar{q} \rightarrow \mu^+\mu^-$ by the PDFs $f(x)$:

$$\sigma_{AB} = \int dx_a dx_b f_{a/A}(x_a) f_{b/B}(x_b) \hat{\sigma}_{ab \rightarrow \mu^+\mu^-} \quad (4.3)$$

where $ab = q\bar{q}, \bar{q}q$, while x_a and x_b are interpreted as the fraction of the four-momenta of the two protons carried by the initial state partons.

Their predictions were in good agreement with measurements, providing further confirmation of the parton model of the proton. The calculation of the perturbative corrections from virtual or real gluon emission led to large logarithmic terms, though, which seemed to spoil the use of a perturbative expansion. But it was discovered that the logarithms in Drell-Yan corrections can be factorized and included into the PDFs by renormalization. This is called the factorization theorem, and adds a weak dependence on Q^2 to the PDFs, violating the exact scaling. In essence it means that soft gluon radiation directly before the hard interaction is interpreted as being part of the proton structure. E.g. for electron-proton scattering the quarks appear as point-like particles for low Q^2 , while with increasing Q^2 the electron is able to probe the proton structure with a higher “resolution” and does resolve more partons, all carrying a smaller fraction of the proton momentum.

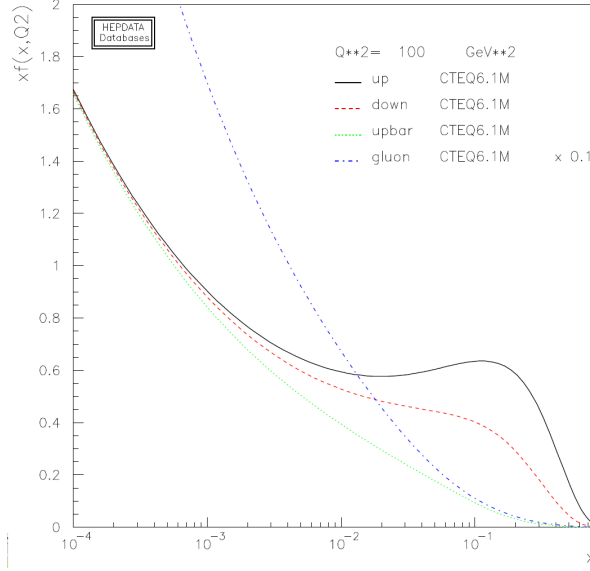


Figure 4.2: The CTEQ6.1 parton distribution functions evaluated at a Q of 10 GeV. [20]

A modern day PDF set for one value of Q^2 is shown in figure 4.2.

Finite corrections remain after factorization due to gluon radiation with higher momenta, and are dependent on the actual process leading to the use of a perturbative expansion of hard scattering cross sections:

$$\sigma_{AB} = \int dx_a dx_b f_{a/A}(x_a, \mu_F^2) f_{b/B}(x_b, \mu_F^2) \left[\hat{\sigma}_0 + \alpha_s(\mu_R^2) \hat{\sigma}_1 + \dots \right]_{ab \rightarrow X} \quad (4.4)$$

where μ_F^2 is the factorization scale and μ_R^2 is the renormalization scale for the running of the coupling. The factorization scale divides physics into long distance physics, where soft gluon emissions are factorized into the PDFs, and short distance physics, where virtual or real emissions have to be included specifically for the process.

A cross section calculated to all orders of α_s is in principle invariant under changes of μ_F^2 and μ_R^2 . But as the calculation is generally cut off at some point the resulting cross sections have a dependency on these scales. Commonly the typical momentum scale of the scattering process is used for both scales, and $\mu_F^2 = \mu_R^2$ is assumed. The dependence on the choice of these scales is significant for leading order calculations, and becomes smaller if higher orders are included.

As a summary e.g. the leading order cross section for an inclusive final state X , e.g. large p_T jet production, can be obtained by:

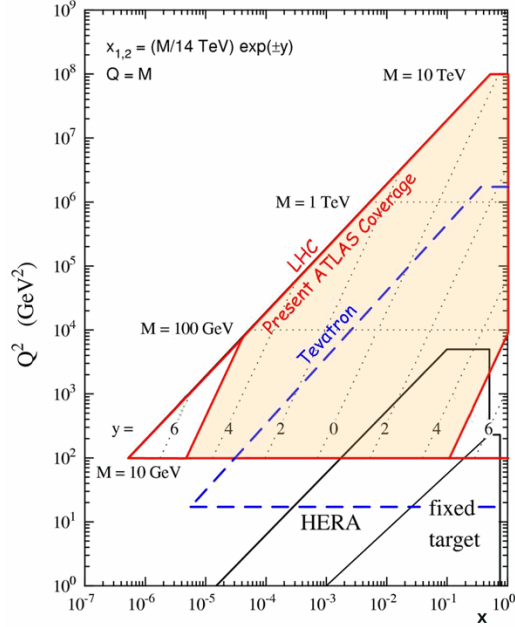


Figure 4.3: Graphical representation of the relationship between parton (x, Q^2) variables and the kinematic variables corresponding to a final state of mass M produced with rapidity y at the LHC collider with $\sqrt{s} = 14$ TeV [13]

1. Identification of all leading-order parton processes contributing to the final state
2. Calculation of the cross-sections $\hat{\sigma}_0$
3. Inclusion of appropriate PDFs for the initial state partons
4. The choice of the scales μ_F^2 and μ_R^2
5. A numerical integration over x_a, x_b and phase-space variables of the final state

The kinematics on parton level are defined by x_a and x_b . Figure 4.3 shows the range of kinematic variables that is accessible at the LHC, the Tevatron at the Fermilab, the HERA accelerator at the “Deutsches Elektronen Synchrotron” and fixed target experiments. For the LHC the horizontal pointed lines depict a selection of parton center-of-mass energies M . The position where these cross the two pointed lines depicting one value of the rapidity y give the $x_a \neq x_b$ required to result in these kinematic variables.

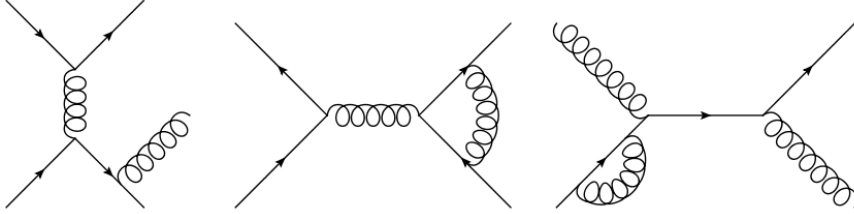


Figure 4.4: Examples of NLO Feynman diagrams of QCD dijet production

4.1.2 From Parton to Particle Level

Higher Order and All Orders Approaches

The leading order approach to describe a hard scattering process and determine the cross section, e.g. using Feynman rules as described in chapter 2, only gives a rough estimate.

For a calculation to higher order all diagrams contributing an additional strong coupling factor α_s have to be included. These can be split into virtual emission of particles (loop corrections) and real emissions changing the final state by the addition of further partons. Figure 4.4 shows some Feynman diagrams on next-to-leading order of α_s , adding to the first two in figure 2.1 on page 8.

The number of required diagrams rapidly rises with the order of α_s , and thus the exact calculation of higher order contributions is nontrivial, additionally complicated e.g. due to singularities arising when the momentum in a particle loop is taken to the limit of zero.

An alternative are all order approaches. Instead of systematically trying to calculate higher and higher orders in α_s for a given observable, dominant contributions from all orders are considered by the use of evolution equations.

In the parton shower approach, e.g. used by PYTHIA[21]², the few partons produced in the hard interaction are related to partons close to the QCD scale Λ . At this scale a phenomenological model can then be used to perform the hadronization of final state partons. The solution of the evolution equations can be expressed in Sudakov form factors, which give the probability that a parton evolves from a higher to a lower scale without the emission of a gluon with some resolution scale higher than a given value. In PYTHIA 6.4 the relative transverse momentum of the two partons is used as that scale. The evolution of scales is always done starting from the hard interaction, and is thus done backwards in time for the initial state partons. Figure 4.5 shows example Sudakov form factors for initial state quarks.

²PYTHIA 6.412 is main the Monte Carlo generator used in this thesis

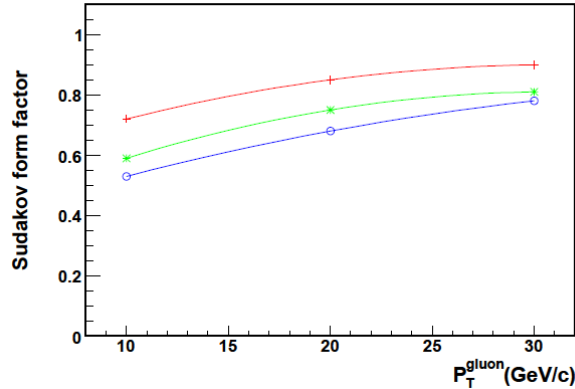


Figure 4.5: The Sudakov form factors for initial state quarks at a hard scale of 500 GeV as a function of the transverse momentum of the emitted gluon. The form factors are for (top to bottom) parton x values of 0.3, 0.1 and 0.03. [13]

Parton showers give a very good description of low-angle and soft gluon emission, while fixed order calculations provide a good description of partons that are widely separated, additionally including interference effects. Thus the optimal approach is to combine fixed order calculations with parton shower models. Care has to be taken to avoid double-counting in kinematic regions where both techniques overlap, which is nontrivial. E.g. there is no Monte Carlo generator available at the time of writing that combines NLO calculations with parton showers for inclusive jet production at the LHC.

Thus another method is required to obtain NLO predictions for jet production, termed NLO k -factors. The k -factor for a given process is the ratio of the NLO to the LO cross section, e.g. shown for jet production in figure 4.6. It is determined from matrix element calculations, and can be applied to correct the cross section for a process where the Monte Carlo generator interfaced with parton showers is only available at leading order of α_s .

Parton Distribution Functions

Once the cross sections of the process on particle level are known, these have to be weighted by the parton distribution functions. These PDFs can not be calculated perturbatively, but have to be determined from data of DIS, Drell-Yan and jet production. Parton distributions at a given x and Q^2 can be evolved to higher Q^2 using the so called DGLAP equations³, though. Thus figure 4.3 on page 31 suggests that the PDFs can be reasonably constrained by previous experiments

³named after Dokshitzer, Gribov, Lipatov, Altarelli and Parisi, who first formulated the equations

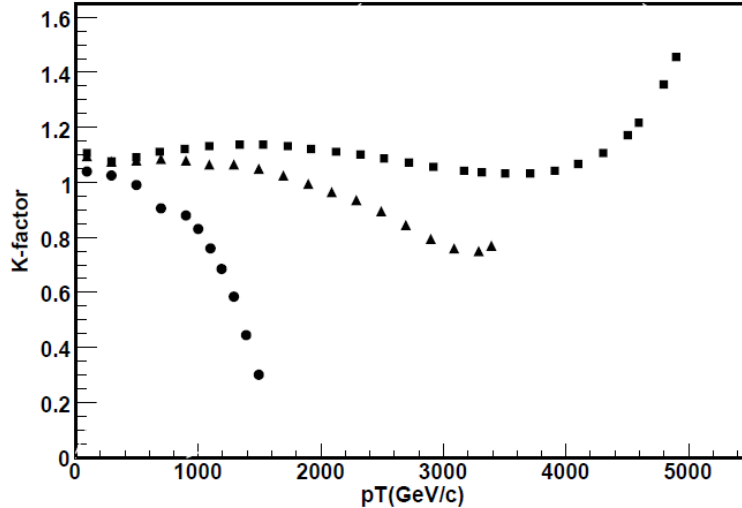


Figure 4.6: The ratios of the NLO to LO jet cross section predictions for the LHC using the CTEQ6.1 PDFs for the three different rapidity regions: 0 to 1 (squares), 1 to 2 (triangles), 2 to 3 (circles). [13]

for the majority of the kinematic range at the LHC.

There are two groups providing global fits of the PDFs to data, MRST[22] and CTEQ[20]. Both groups use over 2000 data points for the PDF fits, and for most data points the systematic errors are larger than the statistical errors. A correct treatment of systematic errors is thus very important, especially concerning the extrapolation to higher Q^2 . In addition to the accuracy of the measurement, uncertainties on $\alpha_s(Q^2)$ and the accuracy of the method used for the DGLAP evolution contribute to the errors.

Thus for the use of PDFs to obtain cross section predictions not only the best estimate of the PDFs, but also their errors are of interest. To calculate PDF errors the Hessian method is commonly employed. E.g. the CTEQ6 PDF set has 20 free parameters in the fit. A 20×20 matrix of fit χ^2 is diagonalized, resulting in 20 orthogonal eigenvectors which can be used to determine the PDF error for any cross section. For example figure 4.7 shows the PDF errors of the different eigenvector directions for the CDF inclusive jet cross section. While all eigenvectors correspond to some linear combination of free fit parameters, eigenvector 15 is of note as it represents the largest change in the high- x gluon behavior, primarily affecting jet production.

Figure 4.8 finally shows the uncertainty of the inclusive jet production cross section at the LHC for the CTEQ6.1M set. In this thesis the ATLAS standard PDF set is used, which is still CTEQ6L1 according to the ATLAS recommendation

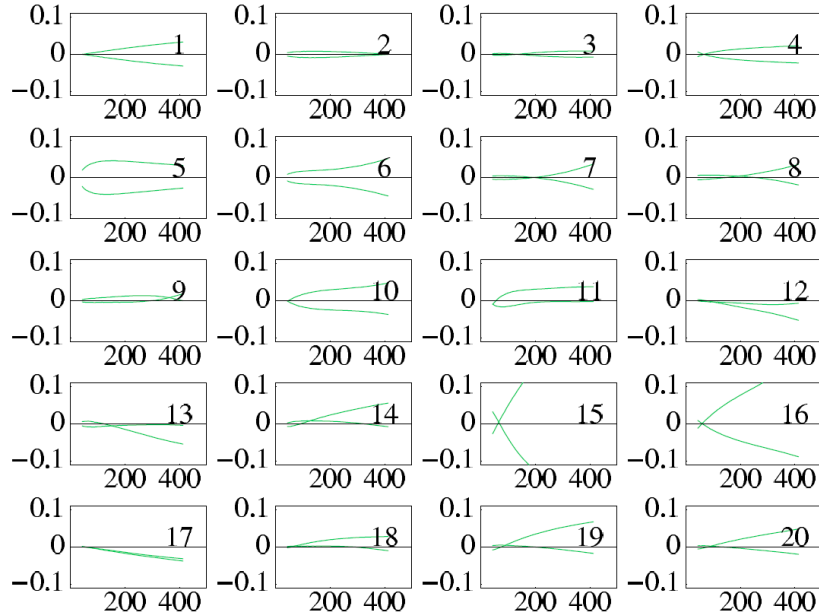


Figure 4.7: The inclusive jet production cross sections at the Tevatron, plotted as fractional differences compared to CTEQ6.1M for + and - displacements along the 20 eigenvectors, and as a function of jet p_T in GeV [20]

to use LO PDFs with leading order α_s with LO Monte Carlo generators. A new CTEQ PDF set version 6.6 has become available lately, including significant improvements concerning the PDF errors [23]. This set is only available using NLO calculations to fit the data. As, at least for inclusive jet production, it is viable to use NLO PDFs together with LO Monte Carlos, and the results are often closer to full NLO expectations despite formally still being leading order, it has to be considered to switch to this PDF set before data taking.

Factorization Scale and Renormalization Scale

The next important theoretical uncertainty on jet production cross sections is a result of the ambiguity in the choice of factorization scale μ_F and renormalization scale μ_R . It was already stated that a change from LO to NLO calculations not only increases the general accuracy of the prediction, but also decreases the uncertainties arising from the choice of scales. Thus in order to compare Monte Carlo predictions with data, ideally at least NLO calculations are used, as the scale uncertainties are very large for LO. For inclusive jet production the Monte Carlo generation is done in a combination of LO calculation and parton showering. The use of NLO k-factors is thus not only advisable to increase the accuracy of the mean value of a prediction, but also to constrain the uncertainties due to the

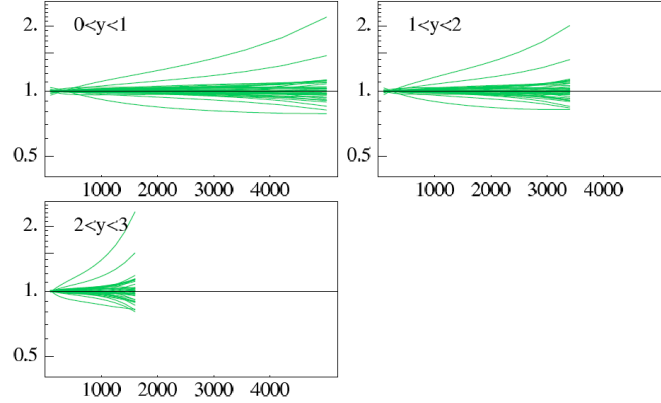


Figure 4.8: The uncertainty range of the inclusive jet cross section at the LHC. The curves are graphs of the ratios of the cross sections for the 40 eigenvector basis sets compared to the central (CTEQ6.1M) prediction versus jet p_T in GeV [20]

choice of scales. In this thesis it is assumed that all LO order predictions are approximated to NLO by the use of k-factors for the comparison with data, and thus the NLO scale uncertainty, or in other words the uncertainty of the correction to NLO arising from the choice of scales is used as theoretical uncertainty.

Weak Corrections for Jet Production

As the momentum transfer of hard scattering processes at the LHC can be far above the W mass, perturbative electroweak corrections could play an important role in addition to the QCD corrections[24]. Specifically virtual electroweak corrections of the following form may become significant:

$$\alpha_W \log^2(\hat{s}/M_W^2) \text{ with } \alpha_W = \alpha_{EM}/\sin^2\theta_W \quad (4.5)$$

where α_{EM} is the electromagnetic coupling constant and θ_W the weak mixing angle. These corrections come from a lack of cancellations of virtual and real W emission in higher order corrections. The impact of the virtual electro-weak logarithms is shown in figure 4.9, motivating that required corrections could be of comparable size to NLO QCD corrections.

Spectator Partons and Underlying Event

The so-called underlying event is an important part of the environment at a hadron collider. As the proton contains more partons, termed spectator partons, than the two involved in the hard scattering, additional jets are present in a proton-proton collision.

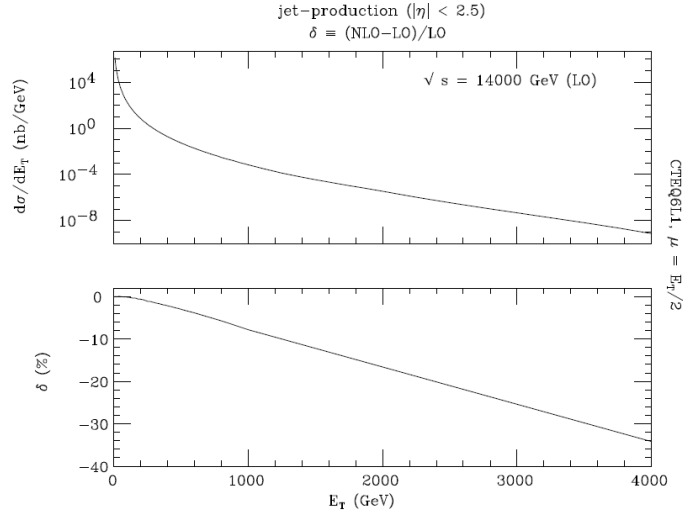


Figure 4.9: The effect of electroweak logarithms on jet cross sections at the LHC. [13]

PYTHIA utilizes a multiple parton interaction framework for the underlying event, where additional semi-perturbative interactions between the spectator partons are produced, including colour, flavour and momentum correlations to the hard interaction. The model used is phenomenological and must be tuned to data. In addition it is highly sensitive to the gluon distribution at low x .

While this soft physics is interesting in its own right, for this thesis the underlying event is purely treated as a background for the hard scattering, which has to be corrected for in order to be able to measure the precise characteristics of the hard process. In comparison to the so called pile-up, which is multiple concurrent proton-proton interactions, the underlying event is independent of the luminosity and will be present in data from the start.

Hence a measurement of the underlying event properties will be one of the first measurements required at ATLAS.

Hadronization

Quarks and gluons, carrying color charges, can not be observed directly due to color confinement. Thus the particles measured are not partons but colorless hadrons created by a process called hadronization. This process is not understood from first principle and phenomenological models have to be used.

In PYTHIA the Lund string model is used for hadronization. It treats all but the highest energetic gluons as field lines, which form a narrow tube called string

due to their self-interaction⁴. In a simplified picture, if enough total energy of two colour connected partons is available, additional partons are created and split the colour string. If there is not enough energy available the string can not be split, and the two partons are confined to a hadronic state.

Finally the resulting hadrons are forced to decay if short-lived, e.g. hadrons containing quarks of the second or third family which decay weakly. The final particle composition reaching the calorimeters of an experiment is dominated by charged pions and photons from neutral pion decays.

Summary

With the hadronization the last step required to arrive at hadrons actually being measured in a detector, starting from Feynman diagrams, is complete. At first the hard interaction of two partons at leading order of α_s was discussed, and then generalized to a hard process occurring in a proton-proton collision. Apart from parton distribution functions a solution was needed for the problem that ideally higher orders in α_s are required for a precise calculation of cross-sections and the correct classification of inclusive final states. As this problem can not be solved fully analytically the particle shower approach was introduced, combined with LO Monte Carlo generation and the correction of cross-sections to NLO. Lastly concurrent interactions of the additional partons of the proton were discussed as well as the hadronization mechanism to arrive at final state hadrons.

Of special mention is that significant theoretical uncertainties result from the accuracy of the knowledge of PDFs as well as from the fact that Standard Model radiative corrections are only precisely treated to a fixed order of the involved couplings, and include scale dependencies.

4.2 Jet Measurement and Reconstruction at ATLAS

The last section concluded with a framework for particle level predictions e.g. for inclusive jet production at the LHC, using a combination of perturbative QCD and a number of phenomenological models. These predictions are events with certain configurations of hadrons in the final state together with respective cross-sections. This section takes an approach in the opposite direction, starting at the energy depositions caused by highly energetic hadrons in the ATLAS calorimetry and describing the procedures required to arrive at a measurement of processes at the particle level.

The goal is to be able to compare theoretical predictions on the particle or parton level with experimental measurements. While such a comparison is viable after correcting the measured data to particle level with the procedures outlined in the following, it is not always sufficient. To e.g. estimate necessary jet corrections

⁴in contrast to e.g. electromagnetic field lines that can be thought of as spreading out as their is no photon self-coupling

or to extrapolate a jet calibration to higher p_T values, Monte Carlo predictions including a simulation of the detector are necessary. This is the concluding topic of this section.

But before going into detail, the kinematics on parton and jet level are defined to establish a number of variables.

The Parton Level Kinematics

The four-momenta of the two incoming protons, neglecting particle masses and a possible momentum component transversal to the beam, are:

$$P_A = (E, 0, 0, E) \text{ and } P_B = (E, 0, 0, -E) \quad (4.6)$$

The square of the center-of-mass energy \sqrt{s} in the proton system is:

$$s = (P_A + P_B)^2 = 4E^2 \quad (4.7)$$

With x_a and x_b being the fraction of the proton momenta carried by the initial state partons, the square of the center-of-mass energy $\hat{s} = M^2$ in the parton system is:

$$M^2 = (x_a P_A + x_b P_B)^2 = ((x_a + x_b)E, 0, 0, (x_a - x_b)E)^2 = 4E^2 x_a x_b = x_a x_b s \quad (4.8)$$

As generally $x_a \neq x_b$, the center-of-mass system of the initial state partons has a boost along the beam axis with respect to the laboratory system. Using the three-momentum $p = (p_x, p_y, p_z)$ for outgoing partons or jets, with the incoming beams being parallel to the z-axis, the boost-invariant transverse momentum $p_T = \sqrt{p_x^2 + p_y^2}$ is defined. In addition it is common to define the rapidity $y = \frac{1}{2} \ln\left(\frac{E+p_z}{E-p_z}\right)$. If the particle masses are negligible compared to the momenta, the pseudo-rapidity η can be used instead:

$$\eta = \lim_{\frac{m}{p} \rightarrow 0} y = -\ln\left(\tan\frac{\theta}{2}\right) \quad (4.9)$$

where θ is the angle between the outgoing parton or jet and the beam axis. This correlation to θ allows to trivially calculate η in the laboratory frame, whereas for y the particle mass has to be known. Assuming massless particles, η differences are boost invariant, making it a very useful coordinate and preferable to the use of θ . The coordinate system is completed by the azimuthal angle ϕ in the plane perpendicular to the beam axis.

4.2.1 Jet Algorithms

One necessity to compare theoretical predictions of jet production and event topologies with measured data is a common definition of a jet. Jets are defined by jet algorithms, which must be applicable on any of the following levels and ideally produce the same results:

- Parton level: The final state partons of the hard process at NLO or higher order⁵
- Particle level: Particles obtained after the addition of the underlying event and hadronization to the parton level
- Calorimeter level: Energy depositions measured with calorimeters, either in experimental or simulated data

The main jet algorithm used in this thesis is a classical seeded cone algorithm. It builds jets around seeds, which are either energy depositions in the calorimeter, particles or partons. All objects with a distance to the seed less than the size parameter R are considered to compose a proto-jet, with the distance being defined as $\Delta R = \sqrt{(\Delta\eta)^2 + (\Delta\phi)^2}$. Using all objects inside the cone a p_T weighted centroid of the jet is calculated, and a new proto-jet defined around that centroid. This is done iteratively until the cone is stable. As jet cones may overlap, a split/merge procedure is done at the end, e.g. at ATLAS merging all jets that share more than 50% of their momenta, and adding objects to the closer cone only otherwise.

The second jet algorithm used is the k_T algorithm [25][26]. It starts with the list of clusters, which are usually final state hadrons or an approximation thereof, and defines a parameter d for each cluster i , and each combination of two clusters i and j :

$$d_i = p_{T,i}^2 \text{ and } d_{ij} = \min(p_{T,i}^2, p_{T,j}^2) \frac{\Delta R_{i,j}^2}{D^2} \quad (4.10)$$

where D is a size parameter of the jet algorithm, ΔR a distance as defined above and $i \neq j$. For $D = 1$ and a small distance ΔR_{ij} the parameter d_{ij} is the squared minimal transverse momentum k_T of one of the clusters in respect to the other one. The minimum of all d_i and d_{ij} is determined. If that minimum is one of the d_i values the corresponding cluster is defined to be a jet and removed from the list of clusters. If the minimum is one of the d_{ij} values, the clusters i and j are merged to one cluster, and all parameters are recalculated. The whole procedure is then iterated.

One main advantage of the k_T algorithm is that it is infrared safe. The concept of infrared safety is sketched in figure 4.10.

⁵no jet algorithm is required for a LO $2 \rightarrow 2$ process

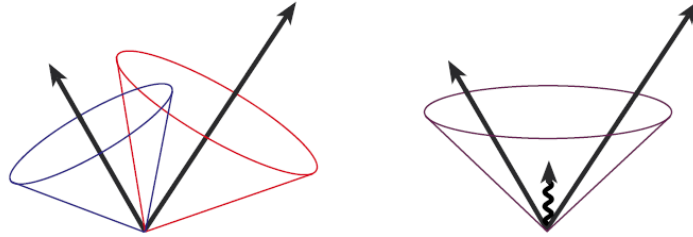


Figure 4.10: An illustration of infrared sensitivity in cone jet clustering. In this example, jet clustering begins around seed particles, shown here as arrows with length proportional to energy. It is illustrated how the presence of soft radiation between two jets may cause a merging of the jets that would not occur in the absence of the soft radiation. [26]

With the reliance of the cone algorithms on seeds, e.g. an additional soft radiation between two jets can decide if one or two jets are found. One option called the midpoint cone algorithm exists to increase the infrared safety by putting additional seeds between any two seeds, to limit the dependence on possible soft jet being measured as extra seeds. While the ideal solution is using a seedless cone, starting with a fine grid of seeds independent of any objects, it is computationally too slow for practical applications.

The main advantage of a seeded cone algorithm compared to the k_T algorithm is that it requires significantly less computing power. Additionally corrections for energy or objects located out of the cone and the correction needed to subtract the underlying event are well defined and constant due to the simple jet shape. For out-of-cone effects this may be surprising at first, but the fraction of jet energy located out of cone decreases proportional to the increasing total energy, due to high p_T jets being more collimated. This keeps the required correction roughly constant. Both corrections cancel each other out partially or even fully for cone jets, depending on the parameter R , as e.g. shown in figure 4.11.

The standard jet algorithms used in ATLAS and this thesis are:

- Seeded Cone, $R = 0.4$ and 0.7 , minimum p_T of seeds of 1 GeV, split/merge fraction 0.5
- A fast implementation of the k_T algorithm, $d = 0.4$ and 0.6 , using a nearest neighbor concept to reduce the number of d_{ij} values that are calculated for each iteration

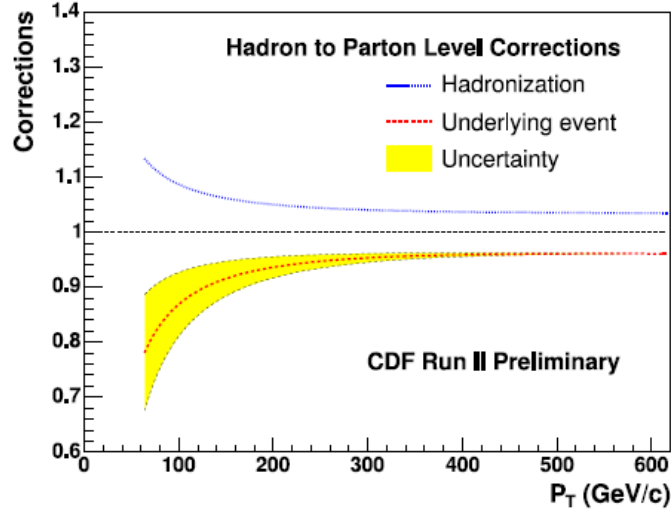


Figure 4.11: Fragmentation and underlying event corrections for the CDF inclusive jet result, for a cone size $R = 0.7$. [13]

4.2.2 Jet Calibration

In addition to a common jet definition the comparison of theoretical expectations to experimental data requires a thorough calibration of jets on calorimeter level. The main interest concerning the jet calibration in this thesis is the linearity of the jet energy scale (JES), for the actual calibration work as well as inclusive jet studies. The JES denotes the energy reconstructed from depositions measured in the calorimeters and using a jet algorithm, compared to the particle or parton level.

Effects influencing the jet energy on particle level have already been mentioned, like out-of-cone effects and the underlying event. This section is focused on instrumental effects, before the jet calibration is generally discussed.

Instrumental Effects on Jet Measurements

Electromagnetic and Hadronic Scale ATLAS has an electromagnetic and a hadronic calorimeter, which are both non-compensating sampling calorimeters. The particles of a jet cause showers of secondary particles due to the interaction with the absorber materials of the calorimeters. A fraction of the energy of these showers is sampled by the active material, producing the measured response. All calorimeter types at ATLAS are non-compensating and thus the scale of the measurement is different for hadrons compared to photons and electrons, by about 30%.

Jets, at the time when they reach the calorimeter, are mainly composed of

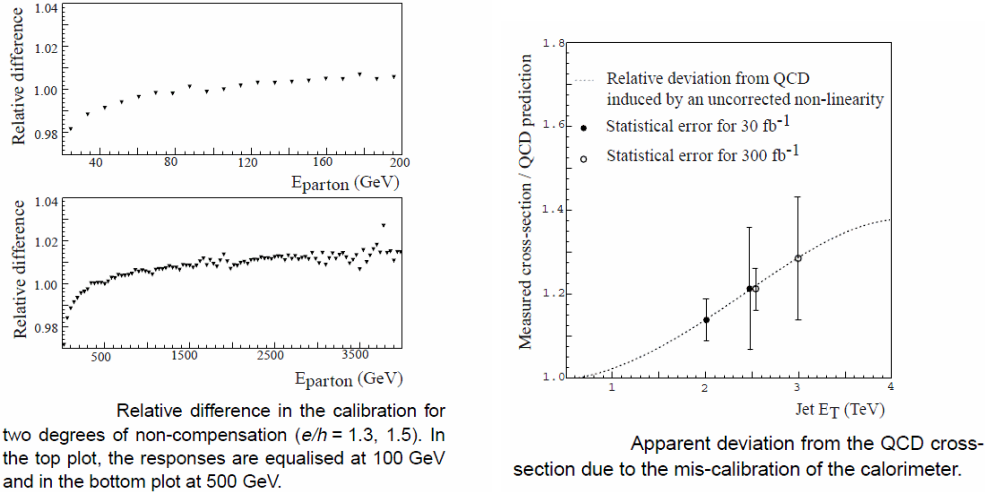


Figure 4.12: Study of a possible residual non-compensation[27]

charged pions and photons from neutral pion decays. Thus the calorimeter response for charged pions and decay products of neutral pions differs by the same 30%. As the composition of jets can be seen as a statistical process, this gives rise to the problem of the jet energy scale calibration, as the calorimeter response in relation to the jet energy is somewhere in between the response to photons and pure hadrons.

The electromagnetic scale of the calorimeters was directly determined by test-beam measurements. The non-compensation can e.g. be written as:

$$\frac{e}{\pi} = \frac{\frac{e}{h}}{1 + (\frac{e}{h} - 1)F(\pi^0)} \quad (4.11)$$

where e is the calorimeter response to pure electromagnetic energy deposition, h to pure hadronic energy, π is the response to pions e.g. measured at the test-beam and $F(\pi^0)$ is the expected fraction of neutral pions produced in the interaction, which is taken as $F(\pi^0) = 0.11 \ln E$. The value of $\frac{e}{h}$ was determined from test beam data, resulting in $\frac{e}{h} = 1.37 \pm 0.01$. The verification of this value for experimental ATLAS data of very high p_T jets can only be done by Monte Carlo data. Depending on the shower model during simulation the Monte Carlo measurements disagree by about ± 0.2 . The influence of such a difference in $\frac{e}{h}$ was simulated and is shown in figure 4.12. The effect on the inclusive jet cross section is estimated to be up to 40% [27].

Leakage into the Muon System While the majority of jets is expected to have showers that are fully contained in the calorimeter, the showering is a statistical

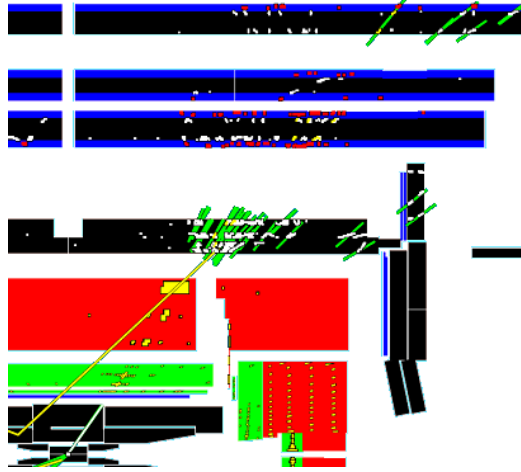


Figure 4.13: Event display of a simulated event with significant jet leakage into the Muon System. The calorimeters are shown in green (electromagnetic) and red (hadronic), while the outer black and blue structures are the Muon System

process. Even at low jet energies single “heroic” pions can e.g. reach the muon system of ATLAS and for the highest jet p_T values a significant portion of a jet or shower can “punch through” into the Muon System. While dramatic cases, e.g. shown in figure 4.13, could be tagged by the hits in the Muon System and subsequently removed from analysis, this leakage can also lead to another nonlinearity in the JES.

Dead Material and Detector Cracks Jet and shower energy is lost in dead material of the detector and in the cracks that are e.g. between the barrel and end-cap calorimeters. This has to be locally compensated by the jet calibration.

Detector and Electronic Noise The last factor concerning energy measurements with the ATLAS calorimeters is electronic noise of the detector and front-end electronics that has to be subtracted for the precise measurements of jets.

ATLAS Calibration Approach

The calibration approach at ATLAS is twofold. One method uses projective calorimeter towers, which are a summation of all cells within an area defined in η and ϕ . The other concept is based on so called topological clusters. This is sketched in figure 4.14.

Tower Jets Tower jets are based on the projective geometry of the calorimeters, and thus work well with the readout geometry of ATLAS. The first step is a

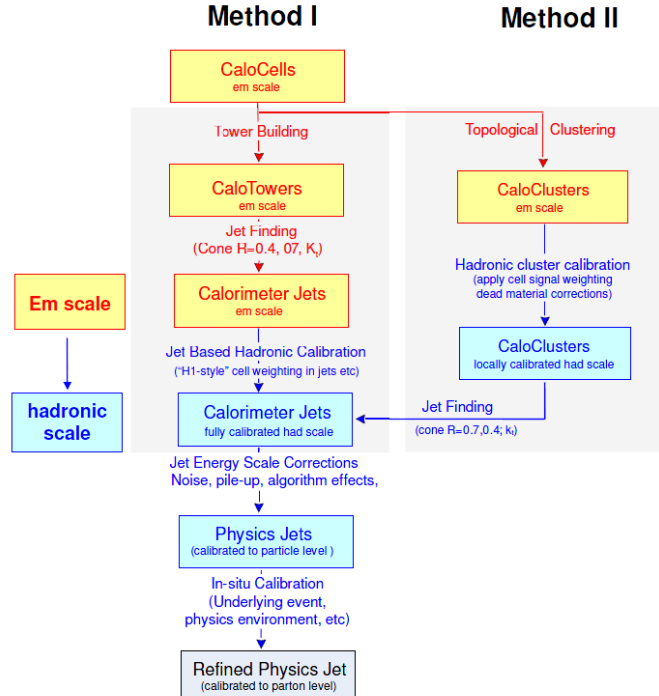


Figure 4.14: Diagram of the calibration approach at ATLAS [28]

summation of cells into towers in principle based on a fixed grid of $\eta \times \phi = 0.1 \times 0.1$. The scale of all cells and thus resulting towers is the electromagnetic, uncorrected scale. During the summation of cells to towers a noise suppression is applied. Towers can end up with negative energies due to detector and electronic noise. These towers are combined with nearby towers of positive energy until the sum of energy is greater than zero. Afterwards jet finding is done using these towers, which can be considered as massless pseudo-particles, resulting in calorimeter jets on the electromagnetic scale.

The next step is the retrieval of all individual cells of the calorimeter jets. A cell based calibration is applied, e.g. to correct for the calorimeter non-compensation and dead material. This calibration includes a classification of cells as predominantly electromagnetic or hadronic, based on energy flow considerations. The jet kinematics are recalculated, resulting in calorimeter jets on the hadronic energy scale, which is defined as the scale where electromagnetic and hadronic showers have the same response.

Jets from Topoclusters For jets based on topological clusters cells are first grouped into three dimensional clusters ideally corresponding to a single calorimeter shower. These clusters are locally calibrated to the hadronic scale based on

their characteristics, in addition to dead material and noise corrections. Thus in contrast to the tower method, calibrated pseudo-particles at the hadronic scale are available, without any bias due to a jet algorithm. Jet algorithms are then directly applied on the calibrated clusters, resulting in calorimeter jets on the hadronic scale. It is expected that these jets will provide a better jet energy resolution in the long-term, but are not used in the standard ATLAS reconstruction yet.

Independently of the procedure to arrive at calorimeter jets, the next step is a further correction of noise, pile-up and algorithm effects to arrive at physics jets, which are in the ideal case at the particle level. Using in-situ calibration methods, the attempt can then be made to bring the jets to parton level, if required by the respective physics analysis.

In-situ Calibration

To calibrate jets to the particle level, as described above, all necessary corrections have to be known precisely. While information is available from testbeam measurements using a large number of modules of the ATLAS detector, one vital task is to verify and extend that knowledge based on real ATLAS data. In addition an in-situ calibration is required to bring measured jets to the parton level.

The basic principle of in-situ jet calibrations is the use of some reference object to verify or improve the jet energy scale or jet energy resolution. Natural candidates for these reference objects are e.g. particles like photons, which are measured very precisely, recoiling against a jet, or mass peaks of known particles like the top quark.

In-situ methods that have been shown to work in previous experiments are vital tools to calibrate the JES. But one issue at ATLAS is that the reach of these methods is significantly less than the reach of jet p_T . Thus for early data it is envisioned to be able to verify the JES up to 500 GeV, but higher scales require an extrapolation using simulated Monte Carlo data. A solution to this problem, a new in-situ calibration method, is proposed in chapter 5 of this thesis, to allow the in-situ calibration of jets at the TeV scale even with earliest data.

4.2.3 The ATLAS Detector Simulation

While the framework that was established in the last sections allows the comparison of predictions on the parton or particle level to measurements at the calorimeter level, by correcting the measured jets at least to the particle level, this is not always sufficient.

The complexity of LHC physics and the ATLAS detector make it necessary to also go further in the opposite direction, by applying a simulation of ATLAS to Monte Carlo data. Especially as there is no real collision data available at the time of writing, a detector simulation is vital to evaluate the detector and physics

performance of ATLAS. All studies presented in this thesis are based on simulated data.

Two options are available at ATLAS, a full and precise simulation of the detector done to the best level of available knowledge, and a simple fast simulation.

Full Detector Simulation

The full ATLAS simulation program is divided into three steps, of which the first one has already been discussed:

1. Event generation
2. Detector simulation
3. Digitization

The second step, the detector simulation, is the most critical and time consuming of the above. The GEANT 4 package[29] is used to simulate detailed detector characteristics, geometry and performance. The four-momenta of stable particles produced by the event generation are tracked on their way through the detector material, also including all dead material like e.g. the cooling or support infrastructure of the ATLAS detector. At any stage a snapshot of the current status can be recorded, which is done most foremost for the active detector regions to simulate the detector response. These snapshots are stored as so called HITS. Information is additionally collected e.g. in the dead material, which is impossible for real data. With simulated data these “calibration HITS” can be used to derive a calibration or verify corrections. While HITS e.g. in the tracker are rather straightforward, most of the processing time is spent for the simulation of showers in the calorimeters.

The next step is the so called digitization, where the recorded HITS are used to simulate the detailed and precise characteristics of the detector signals, e.g. including noise injection and the front-end electronics behavior. The output of the digitization is in the same format as the real detector readout.

It can thus be directly interfaced with the reconstruction, where e.g. the jet finding and calibration is done.

While the full detector simulation of ATLAS is a very powerful tool, it requires a lot of computational resources. The simulation of a single event takes about 20 minutes on average, and up to 40 minutes for high multiplicity events, as for example including pile-up. As a result a fast and more parametrized simulation is needed to produce high statistics Monte Carlo samples.

The Fast ATLAS Detector Simulation

The fast simulation and reconstruction of ATLAS, termed ATLFAST, uses a simple parametrization of the detector response. It is an intermediate step between an analysis based on particle level information and a study utilizing the detailed detector simulation. In addition to its usefulness to quickly and roughly estimate rates for physics signals or backgrounds, it is the only practical tool for high statistics study, due to the processing time required for the full simulation.

It directly provides a list of reconstructed jets and particles, as well as missing transverse momentum. While the detector performance of the full simulation is reproduced in terms of e.g. a global jet energy resolution, only very basic information about the detector geometry is included. This information is mainly the granularity of the hadronic calorimeter and the η coverage of the calorimetry.

As a result it is very fast, with an average event processing time of 20 ms.

In the last years it has become more and more obvious that another step, in between the above ATLFAST and the full simulation is highly desirable. Even if the processing time required for the fast simulation would be increased by e.g. two orders of magnitude to 2s due to additional features, this would still be acceptable for high statistics studies. The feature missed most in ATLFAST is a parametrization of calorimeter showers, including the option to produce data that can be interfaced with the standard reconstruction. The first feature has been worked on for several years and is basically already available, and a new version of the fast simulation including both features, ATLFAST II, is in the validation process at the time of writing.

4.3 Jet Performance and QCD Benchmarks

This section covers the expected performance of jet measurements at ATLAS, and the introduction of a selection of jet measurements to probe the validity of the Standard Model and perturbative QCD. After the above discussion of hard interactions of gluons and jets, the move to particle and calorimeter level, the strategy for jet finding, reconstruction and calibration and the ATLAS simulation approach, this chapter concludes the groundwork for detailed jet calibration and physics studies.

Monte Carlo Simulated Data Sets

In the current absence of experimental data, data generated with the PYTHIA Monte Carlo and simulated with version 13 of the ATLAS software framework is used. As the inclusive jet cross section drops very fast with jet p_T a continuous simulated data sample starting at low scales would provide no statistics at high scales. To solve this problem the jet p_T spectrum is commonly divided into several

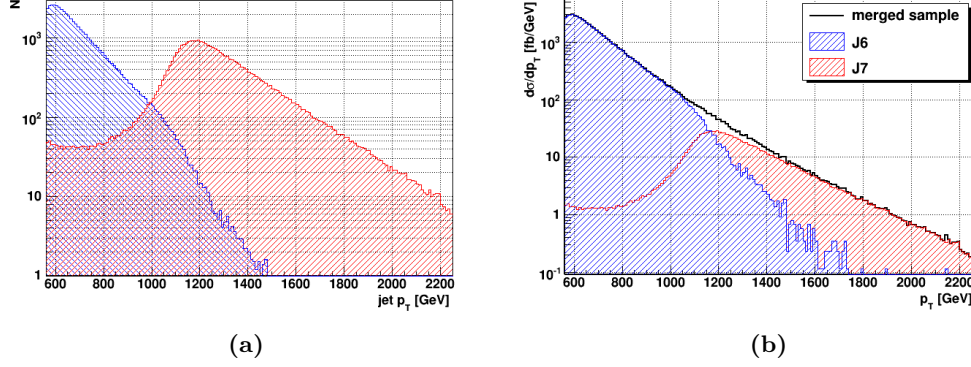


Figure 4.15: Merging of J6 and J7, (a) plain number of events in the samples per 10 GeV, (b) samples weighted by their cross-sections

intervals for event generation. ATLAS uses the following convention of subsets, where the limits on p_T are set on generator level:

Name	p_T range [GeV]	estimated cross section [nb]
J0	8-17	$1.75 * 10^7$
J1	17-35	$1.37 * 10^6$
J2	35-70	$9.63 * 10^4$
J3	70-140	$6.14 * 10^3$
J4	140-280	$3.17 * 10^2$
J5	280-560	$1.25 * 10^1$
J6	560-1120	$3.45 * 10^{-1}$
J7	1120-2240	$5.30 * 10^{-3}$
J8	2240- ∞	$2.22 * 10^{-5}$

The sets named J6, J7 and J8, representing high p_T jet production, are used mostly in this work. To obtain a continuous and consistent sample of QCD jet production spanning over a larger p_T region, the above subsets have to be weighted by their cross-sections and merged. Figure 4.15 e.g. illustrates this for J6 and J7, using fully simulated samples.

These merged samples can then be used to represent experimental data. One caveat of the procedure is that actual statistical fluctuations of a merged sample are not consistent or in a fixed relation to estimated statistical errors of experimental data, as the number of events in the sample rises significantly at each transition. This can be seen in figure 4.15 (a).

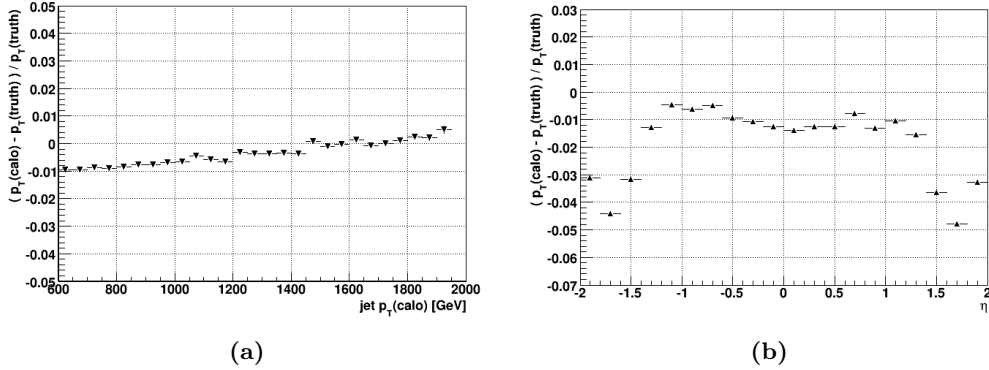


Figure 4.16: Jet response displayed as a function of (a) reconstructed jet p_T , for $|\eta| < 2$, (b) jet η , $p_T > 1$ TeV

4.3.1 Jet Energy Scale and Resolution

In the following the ATLAS jet performance is estimated using the full detector simulation. The standard calibration applied to simulated data can be considered a best case scenario concerning experimental data. This is a result of the use of so called calibration HITS, which are energy depositions in the dead material of the detector, and particle level information which are both not available for collision data. While the initial ATLAS calibration for experimental data will utilize parts of these studies on Monte Carlo data, and the detector simulation is thought to be accurate enough to make this viable, the verification of the calibration is a non-trivial challenge. At first the real jet performance of ATLAS has to be assumed to be a deterioration of the results presented in the following.

One of the most important aspects of Monte Carlo data calibration studies is to identify problems and shortcomings of the calibration and reconstruction procedures, in order to be able to improve them or develop new ones if required.

Jet Energy Scale

The absolute and global jet energy scale at ATLAS will only be known to a certain degree, constrained by in-situ methods. Thus the results using Monte Carlo data, where the absolute JES was calibrated using particle level information, is not a viable estimate for real data. Residual nonlinearities in jet p_T , η or ϕ after the calibration are characteristic for the detector and the calibration procedure, though. Likewise a study of the jet energy resolution using simulated data will result in a lower limit achievable with the ATLAS detector and the applied calibration.

Figure 4.16 shows the difference between reconstructed and particle level jet p_T divided by the particle level jet p_T for a fully simulated sample. This parameter is roughly independent of jet p_T , with an accuracy $< 1\%$. But studied in jet η

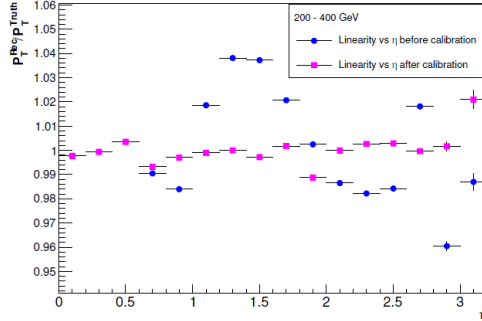


Figure 4.17: Jet response before (blue) and after (red) the inter-calibration in η [30]

significant deviations are visible. This motivates the use of the central detector region, with $|\eta| < 1.5$, for studies with early ATLAS data.

An in-situ method to improve the JES linearity in η was developed by Pavel Weber in the ATLAS Heidelberg group[30], though, based on an inter-calibration using dijet events. Even applied on calibrated Monte Carlo samples, a significant improvement is achievable, as shown in figure 4.17.

Regarding the JES linearity in p_T , the situation in experimental ATLAS data could be radically worse than the above result, as was e.g. motivated in section 4.2.2. Consequently a significant part of the work for this thesis was the development of an inter-calibration method that can linearize the JES momentum dependence, in addition to providing an estimate of the absolute JES uncertainty. This will be described in chapter 5.

The final goal of ATLAS is to achieve a JES uncertainty smaller than 1%, comparable to Monte Carlo results. A rough estimate of the time scale is that it will require at least 5 to 10 years of data taking to reach this goal.

Jet Energy Resolution

The jet energy resolution corresponds to the standard deviation of a Gaussian spread of measured jet transverse momenta around their true values. It is first and foremost a result of the interplay of hadronization and the non-compensating sampling calorimeters of ATLAS, in addition to calorimeter showering and measurements being a statistical process.

A non-constant jet response in η or ϕ also deteriorates the jet energy resolution. Another inter-calibration method was developed in Heidelberg to improve the jet energy resolution by linearizing the response in ϕ [30]. Figure 4.18 shows the result of the standard calibration in Monte Carlo data, after a miscalibration ϕ was introduced and the recovered resolution after the inter-calibration.

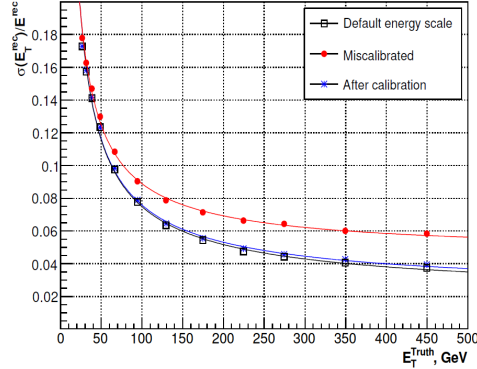


Figure 4.18: Jet energy resolution within $0 < \eta < 0.5$, initial scale (black), miscalibrated energies (red), after the inter-calibration (blue). [30]

The long-term goal of ATLAS is to improve the jet energy scale beyond current Monte Carlo estimates, by the use of the local hadron calibration described in section 4.2.2.

4.3.2 Precision of the Jet Axis

Another important characteristic of the detector and reconstruction is the precision to which the jet axis is reconstructed. This most severely influences the calculation of masses for systems of jets with small angles between the jets, e.g. the reconstruction of a W mass from a hadronic decay.

Regarding this “spatial” jet resolution an unexpected effect was discovered during the work for this thesis. The η distribution of jets of the J6 sample, starting at 560 GeV of p_T on generator level, is shown in figure 4.19 as an example. While the distribution for particle level jets has the expected statistical deviations only, the reconstructed jets show a clear structure on top of that.

The identical effect is present with respect to the jet azimuthal angle ϕ . In figure 4.20 (a) the number of jets is shown in relation to the difference between a jet ϕ value and the lower ϕ border of a cell of the ATLAS hadronic calorimeter, together with a fitted sine function.

This effect was first thought to be a result of a possible glitch in the jet reconstruction. If e.g. the jet axis would not be recalculated after applying a cell calibration, and the final axis used is the one determined from projective towers having the granularity of the hadronic calorimeter. Figure 4.20 (b) shows the relative amplitude of this effect for different jet reconstruction options. As it is practically identical for jets reconstructed either using the cone or k_T jet algorithm, applied either on calorimeter towers or topological clusters, no specific feature of these approaches can be the cause.

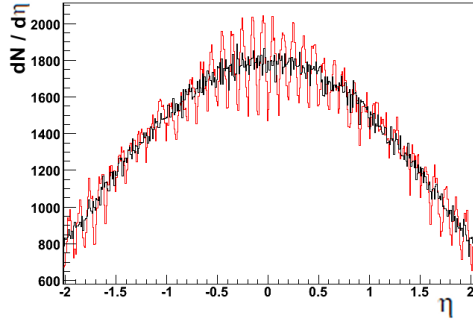


Figure 4.19: The number of jets in dependence of reconstructed (red) and particle level (black) jet pseudo-rapidity

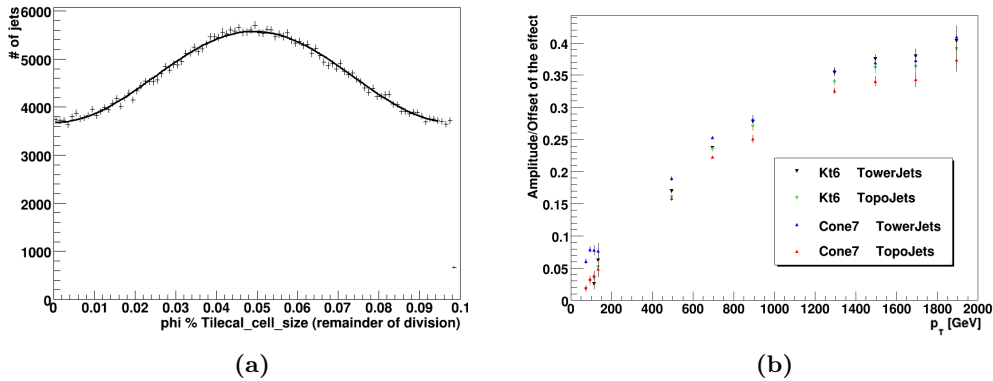


Figure 4.20: Study of the effect on reconstructed jet ϕ

It is now understood that the error of these measurements of the jet axis is a result of the procedure to calculate the jet axis from calibrated cell energies or clusters. In events where a significant part of the jet energy is contained in the hadronic calorimeter, in a single projective tower with the calorimeter granularity, the reconstructed jet axis is drawn strongly towards the center of this tower. In the extreme case of all energy being contained in a single cell with a size of $\eta \times \phi = 0.1 \times 0.1$ the jet must be assumed to be exactly centered in the middle of that cell, as no additional information is available from the calorimeter.

The above described imprecision of the measurement of the jet axis is expected to have the biggest impact on the mass resolution for systems of jets with a small opening angle, e.g. resulting from the decay of high p_T heavy quarks. But for jet p_T values below 200 GeV, most relevant in these cases, it is reasonably small. No specific studies of the influence of this effect on such measurements were done so

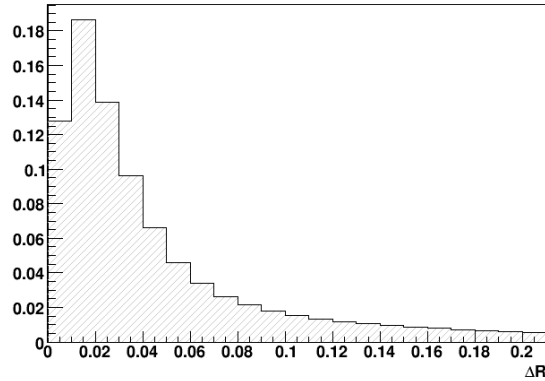


Figure 4.21: Distribution of differences between reconstructed (r) and true (t) jet axis, $\Delta R = \sqrt{(\eta_t - \eta_r)^2 + (\phi_t - \phi_r)^2}$, area normalized to 1

far, but all analyses at ATLAS are done on data including this effect.

For large jet scales the magnitude of this error is up to 40%. The effect on physics studies presented in this thesis is generally still negligible, as firstly the opening angles of jets are close to π in ϕ . Secondly all distributions in η are determined with a granularity equal to that of the effect, preventing any actual influence. A possible impact on invariant dijet mass spectra will be examined in the next section.

If a case arises where an analysis is hindered by this effect, an option is e.g. to assign higher weights to cells of the electromagnetic calorimeter for the calculation of the jet axis, or to outlying cells. This could linearize the angular distributions in η and ϕ , but may decrease the overall precision of the measurement of jet coordinates.

The difference between the reconstructed jet axis and the axis of the matched particle level jet is shown in figure 4.21, for the default reconstruction including the effect and jets above 600 GeV p_T .

4.3.3 Inclusive Jet Spectra

One of the first benchmarks to evaluate the performance of ATLAS with experimental data, and to study perturbative QCD and possible new physics beyond the Standard Model will be the measurement of inclusive jet spectra. These are e.g. utilized to study the sensitivity of ATLAS to new physics in chapter 6 and 7.

Inclusive jet production cross section

Figure 4.22 shows the Monte Carlo expectation for the differential inclusive jet production cross section at ATLAS, with jets being sorted into pseudo-rapidity

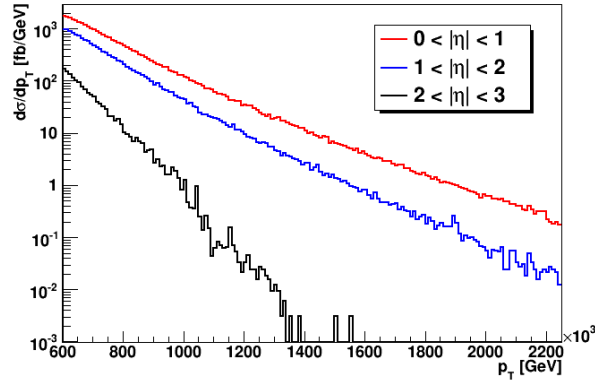


Figure 4.22: Inclusive jet production cross section for different pseudo-rapidity regions

and p_T ranges. This discrimination on η is useful as on one hand new physics is expected to be first found in the central region, and on the other hand the higher η regions are very sensitive to Standard Model corrections. The second point is e.g. motivated by figure 4.6 on page 34, showing that e.g. the k-factors are significantly larger for non-central jets.

While measurements of the inclusive jet production cross section are very important at ATLAS, they are also subject to a large number of systematic effects, the dominant ones being:

- PDF uncertainties of up to a factor of 2
- Perturbative Standard Model corrections, having an uncertainty of up to 40%
- The JES uncertainty; a JES error of 10% can cause a cross section error of 40% to 120%
- The absolute luminosity measurement uncertainty, of the order of 5%

Thus one vital task for early ATLAS data is to constrain both experimental as well as theoretical uncertainties.

Dijet mass spectrum

A second important inclusive measurement is the invariant dijet mass cross section. The invariant mass M_{jj} of a system of two final state jets is defined as:

$$M_{jj}^2 = (P_{j,1} + P_{j,2})^2 \quad (4.12)$$

where P_j are the four-momenta of the jets.

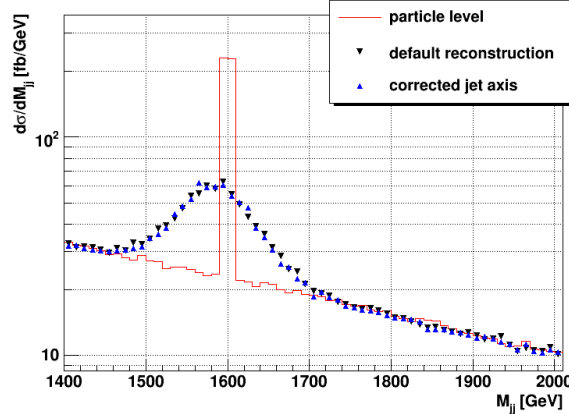


Figure 4.23: Inclusive M_{jj} cross section, including a sharp resonance introduced by hand to estimate the mass resolution

In the limit of massless particles this can be written as:

$$M_{jj}^2 = 2 p_{T,1} p_{T,2} [\cosh(\eta_1 - \eta_2) - \cos(\phi_1 - \phi_2)] \quad (4.13)$$

where $\cos(\phi_1 - \phi_2)$ is roughly equal to 1 for dijet events. As the hyperbolic cosine is rising steeply for large η differences, the error in the reconstruction of the jet axis could play a role for the mass resolution.

To study this an arbitrary resonance was introduced into the Monte Carlo data, by a reweighting of events based on M_{jj} calculated on particle level. This resonance was then measured either using the standard ATLAS reconstruction or the measured and calibrated jet energy together with the jet coordinates determined on particle level. The results can be seen in figure 4.23.

No significant influence is visible and the conclusion is that the jet energy resolution dominates the mass resolution for dijet events at high masses. Thus the effect of the jet axis error is negligible for invariant dijet masses calculated in this thesis.

The main advantage of the dijet invariant mass cross section compared to the inclusive jet cross section is that heavy resonances like excited quark states, or a sharp increase of cross sections based on the center-of-mass energy, result in a stronger signal than in p_T spectra.

4.3.4 Jet Angular Measurements

Another observable that is used in this thesis and provides valuable information about the validity of QCD are jet angular distributions. As the physics at ATLAS is ϕ symmetric the easiest angular distribution containing useful information is the

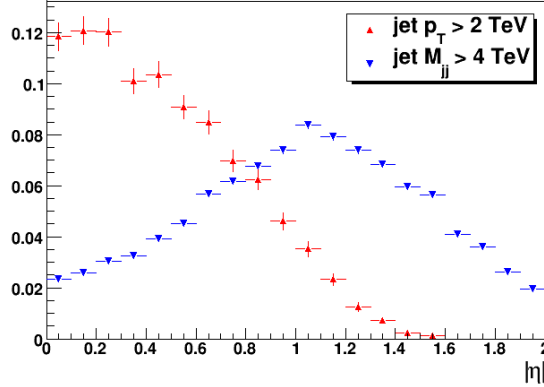


Figure 4.24: Expected η distribution of QCD jet production for two selection criteria, normalized to 1. Errors are statistical uncertainties for 1 fb^{-1}

jet η distribution. Figure 4.24 for example shows the distribution of the absolute value of η for two jet selection criteria. The first one shows jets with p_T greater than 2 TeV. A different way to obtain an η distribution is the selection of events based on the invariant dijet mass M_{jj} instead of p_T . The distribution of the two leading jets per event for $M_{jj} > 4 \text{ TeV}$ is also shown in figure 4.24.

Selecting events based on M_{jj} has one significant advantage. The forward peaked η distribution of the dominant process, t-channel gluon exchange, becomes visible. A common variable to study angular distributions is defined as the ratio R_η of events with leading jets in a pseudorapidity range between 0 and 0.5, and those between 0.5 and 1:

$$R_\eta = \frac{N_{events}(0 < |\eta| < 0.5)}{N_{events}(0.5 < |\eta| < 1)} \quad (4.14)$$

For QCD jet production the expected value of R_η is 0.6, independent of the actual lower limit on M_{jj} that was used during event selection.

The second parameter commonly used for analysis is χ , which can be calculated either with the η in the laboratory frame or the scattering angle θ^* in the center-of-mass frame of the two jets:

$$\chi = e^{|\eta_1 - \eta_2|} \quad \text{and} \quad \chi = \frac{1 + |\cos \theta^*|}{1 - |\cos \theta^*|} \quad (4.15)$$

The motivation for this parameter, seen as a simple sketch, is as follows. Many new physics models, including the two studied in this thesis, are expected to result in isotropic angular jet distributions, being approximately flat in $\cos \theta^*$, while QCD jet production is dominated by $\frac{1}{(1 - \cos \theta^*)^2}$ terms and thus rises rapidly with $\cos \theta^*$.

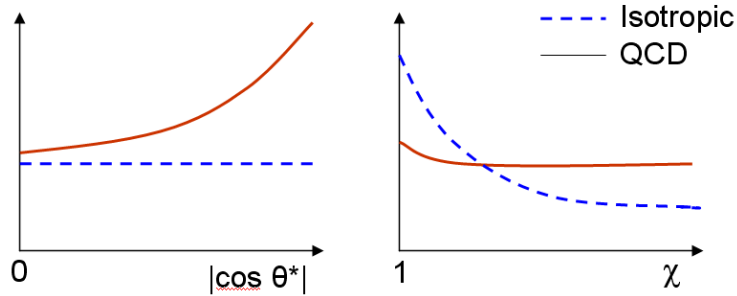


Figure 4.25: Expected angular distribution of isotropic new physics and QCD jet production

This is sketched in figure 4.25 on the left. By the change of variable to $\frac{1+|\cos \theta^*|}{1-|\cos \theta^*|}$ the distributions in $\cos \theta^*$ are “stretched out”. Intervals corresponding to a constant width in $\cos \theta^*$ become increasingly broader for higher values of χ , with $\cos \theta^* = 1$ corresponding to $\chi = \infty$. This is illustrated by the right sketch in figure 4.25, with the distributions normalized to an identical shown area. QCD jet production now results in an approximately flat distribution while the new physics hypothesis leads to an excess of events at low values of χ .

The use of angular distributions has one significant advantage over p_T and M_{jj} spectra, it is less sensitive to systematic uncertainties. This is shown in the chapter 6.

Concerning the systematic error of the jet η measurement that was previously described, the solution for angular spectra is a suitable definition of intervals in χ to sort events into. These intervals are chosen to correspond to a change of 0.1 in the η difference, as the fluctuation of the η distributions directly carries over into the distribution of η differences. Thus the pattern is contained within each bin in χ and no beat due to the combination of the pattern and interval borders is created.

Jet angular distributions will be shown to be a powerful tool to discover or exclude new physics in chapters 6 and 7, especially when experimental uncertainties on cross section measurements are not well under control.

4.4 Summary

This chapter introduced the full framework for jet physics at ATLAS. Starting with perturbative QCD and additional concepts like hadronization that are necessary, the production of predictions for jet measurements was explained first. The required methods to compare these predictions with measured data, jet algorithms

and a jet calibration, were studied next. After the introduction of the ATLAS simulation environment simulated data was used to estimate the jet performance of ATLAS, and to establish a set of measurements to be able to probe perturbative QCD and potential new physics beyond the Standard Model.

A few critical issues have been identified. On the experimental side this is mainly the verification and correction of the JES using experimental data. This is the topic of the next chapter.

Chapter 5

In-Situ Jet Calibration at the Highest Momentum Scales

A precise calibration of the Jet Energy Scale (JES)¹ and a thorough understanding of the associated uncertainties is a crucial requirement for the success of the ATLAS experiment. Many QCD and new physics signatures alike rely on an accurate measurement of jet transverse energies (p_T). Large uncertainties of the JES can not only influence the precision of analyses, but also ultimately their viability. Furthermore a miscalibration of the JES can easily fake signals of physics beyond the Standard Model.

An initial calibration of the JES will be available at the start of ATLAS, utilizing test beam data of single charged pions together with Monte-Carlo simulated jet data. The goal is to surpass the accuracy of this starting point by one order of magnitude using in-situ techniques, to a JES uncertainty of the order of one percent. Using in-situ calibration methods that were employed in previous experiments, this goal should be achievable for jets with transverse energies of a few hundred GeV, but at the TeV scale they are insufficient.

Thus while jets of transverse energies above 1 TeV are essential for many studies at ATLAS, their calibration provides a special challenge. To give an example, two prominent methods to calibrate the JES are the use of so-called prompt-photon events, with one jet recoiling against a precisely measurable photon, or likewise Z+jet events. Both suffer from small statistics, the respective cross-sections for these channels being four to eight orders of magnitude below the inclusive QCD jet production cross section. Before e.g. having enough statistics to provide an in-situ calibration for transverse energies above 1 TeV, millions of jets at that scale would already have been measured, possibly containing evidence for physics beyond the Standard Model which is hidden by JES uncertainties and errors. As a result, in a classical approach, an extrapolation of the absolute jet momentum scale to high values of p_T is still required, using simulated Monte-Carlo events.

¹All particles are treated as massless objects, thus transverse energy E_T and momentum p_T can be used interchangeably for $c = 1$

A vital point regarding this issue is that studies at the highest scales, like e.g. QCD physics with very high- p_T hadronic jets or quark compositeness studies, do often not require a very accurate understanding of the absolute jet momentum scale. Nonlinearities of the jet response can cause quite serious problems, though. The goal is thus defined to, on one hand, reach a good accuracy of the absolute jet momentum scale at transverse energies of the order of 10^2 GeV, and on the other hand measure and correct any deviations from a linear jet response up to the highest values of jet p_T .

In this dissertation a new solution to the second step is proposed, which is denoted as Multi-Jet Bootstrapping in the following. This term hints at two of its features. Firstly it utilizes the very high inclusive QCD jet cross section, the respective events being termed multi-jet events as more than two reconstructed jets are required. This way, the JES can be verified and calibrated up to very high scales even with early ATLAS data of less than 1 fb^{-1} .

The second feature is that the method is no direct JES calibration, but is done with respect to a previously verified region in p_T . This is required as there is no reference object independent from the hadronic momentum scale to be found in the multi-jet events, in contrast to methods where objects measured at the electromagnetic scale are used. Thus the JES is "bootstrapped" up to higher transverse momenta using a reference region at a lower scale, with the option to do this iteratively using the previous result as a new reference region.

As a result it is well suited to linearize the jet response in-situ up to transverse energies of several TeV. Additionally, using the results of other in-situ calibration methods at comparatively low jet momenta, the absolute JES can be obtained for the whole probed range.

Section 5.1 shortly illustrates the problem of using proven calibration methods for high values of p_T , and lists the expected reach and accuracies of these methods. The following section introduces the multi-jet bootstrapping method, motivating its use and showing basic characteristics. In addition, systematic effects influencing the bootstrapping calibration are studied and expected upper limits on the method's systematic uncertainties derived from simulated data are established. At the same time a procedure to get a handle on systematics using data only is presented. The fourth section finally includes expected results of this method to calibrate the JES at very high transverse energies at ATLAS. In the last section, as an addendum, a second jet bootstrapping method is proposed, which, due to its characteristics, is less suited to linearize the JES as required, but can be utilized to verify the results of the first method and provide an independent estimate of the JES uncertainty.

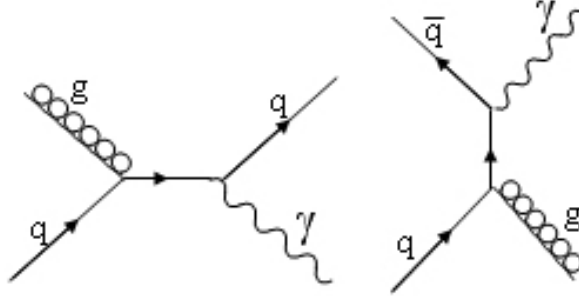


Figure 5.1: Dominant Feynman diagrams for Photon + Jet Production

5.1 In-situ Studies using $\gamma/Z + \text{Jet}$ Events

The first fundamental challenge of jet energy or momentum measurements is the non-compensating calorimetry of ATLAS. Thus the response is different for electromagnetic and hadronic showers. The fraction of energy deposited by jets in the calorimeters is not fixed as the jet composition is purely statistical. All energies are considered to be measured on the so-called electromagnetic scale, and jet energy depositions have to be corrected by about 30% to result in the same response as e.g. for electrons. This correction has to be determined in-situ.

One classical way to solve this problem is to select events in which one particle, recoiling against a single jet, is fully measured on the electromagnetic scale. As an example the dominant production processes for events with a single neutral vector boson and a jet are shown in figure 5.1, exemplarily for the photon case and at leading order of perturbation theory. So at first, considering $\gamma/Z + \text{jet}$ events as two-body processes the vector boson and the jet are expected to be exactly balanced in transverse momentum. A study of this balance in data allows to calibrate the jet momentum scale using the known and precise electromagnetic scale on which either a photon, or the Z via $Z \rightarrow e^+e^-$ or $Z \rightarrow \mu^+\mu^-$, are measured. But at the level of reconstructed events a large number of effects influence this balance, like e.g. initial and final state radiation, or detector and algorithm effects.

In principle the influence of these effects could be reduced by selecting events in which just the vector boson and exactly one jet are present. Such a selection can only be approximated in reality though, and would reduce the already low available statistics heavily. Alternatively one could explicitly include all additional jets in the balance. This presents the choice of either including them in a composite reference object together with the vector boson, or in a composite probed object with the leading jet. The first approach results in an essentially undefined reference object that no longer utilizes the electromagnetic scale only, the second one makes it difficult to relate the resulting calibration to the momentum scales of specific single jets.

Table 2: Fitted p_T balance, error and integrated luminosity of the analysed data samples for the various p_T intervals for the tight photon selection. The last column shows the precision expected for 10 pb^{-1} obtained by scaling the error according to the recorded integrated luminosity.

p_T low edge	Bin width	Fitted balance	Integrated luminosity pb^{-1}	Error for 10pb^{-1}
20 GeV	10 GeV	0.948 ± 0.007	0.67	$\sim 0.2\%$
30 GeV	15 GeV	0.958 ± 0.005	0.67	$\sim 0.2\%$
45 GeV	22.5 GeV	0.953 ± 0.005	9.1	$\sim 0.4\%$
67.5 GeV	33.5 GeV	0.973 ± 0.003	9.1	$\sim 0.4\%$
101 GeV	51 GeV	0.974 ± 0.003	47	$\sim 0.7\%$
152 GeV	76 GeV	0.982 ± 0.002	47	$\sim 0.4\%$
228 GeV	114 GeV	0.984 ± 0.002	535	$\sim 1.7\%$
342 GeV	171 GeV	0.979 ± 0.005	535	$\sim 4\%$
513 GeV	256 GeV	0.994 ± 0.026	535	$\sim 19\%$

Figure 5.2: Expected JES uncertainty using $\gamma + \text{Jet}$ events for 10 pb^{-1} [31]

In practice the difference $\Delta\phi$ in the azimuthal angles of the boson and the jet proves to be a useful quantity. Introducing an event selection requirement on $\Delta\phi$ aims at reducing instead of fully eliminating a possible bias introduced by additional radiation. It thus acknowledges that the two methods outlined above are not practical. A further requirement to reduce bias of the p_T -balance is the right choice of quantity to subdivide the probed p_T range. As this issue is analogous in the multi-jet bootstrapping case it is studied there in the respective section.

As a conclusion, using $\gamma/Z + \text{jet}$ events a p_T balance can be measured in order to calibrate the absolute JES. This balance has a residual bias $< 1\%$ after all event selection cuts on Monte-Carlo data, which is treated as a systematic error. Using both calibration methods utilizing vector bosons, the ATLAS collaboration aims at a JES precision in the order of a few percent for jets up to a transverse momentum of 500 GeV, with less than 1fb^{-1} of integrated luminosity [31].

5.2 Multi-Jet Bootstrapping

5.2.1 Introduction

As previously outlined, the motivation of the method herein after termed multi-jet bootstrapping is twofold. On one hand there is the incentive to use the large QCD-jet cross section to calibrate the JES, since using events containing vector bosons does not offer the desired reach in transverse momentum. On the other hand even localized nonlinearities of the JES can heavily influence analyses with jets of the

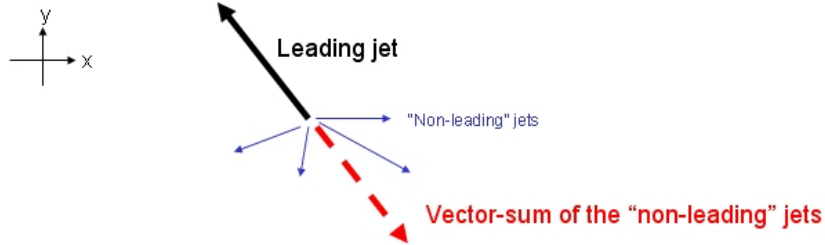


Figure 5.3: Sketch of a sample event topology

TeV scale. A method having access to very high statistics is thus envisioned to be able to measure and correct deviations from a linear jet response with a high resolution in p_T .

The basic idea can be seen as providing a precise JES inter-calibration, not in η or ϕ but in p_T , the desired result being a constant jet response up to very high transverse energies. Other in-situ methods can then be used as a reference point to establish the absolute jet momentum scale.

The method is based on the selection of events with at least three reconstructed jets, while one jet, hereafter termed the leading jet, is required to have significantly more transverse momentum than all others. In this way the leading jet is on a different p_T scale compared to the other jets reconstructed in the event, simply termed non-leading jets or remnant jet system.

Figure 5.3 is a simple sketch of an example jet configuration. To study the JES the non-leading jet momenta are summed vectorially to provide a composite object to balance the leading jet against. Thus a correlation between the momentum scale of the leading jet, and the scale of the non-leading jets can be established. If, in the simplest case, the absolute JES is known for the non-leading jets, it can be verified for the p_T of the leading jet. The following definition is used for the multi-jet p_T balance:

$$p_T \text{ balance} = \frac{p_T^{\text{leading jet}}}{p_T^{\text{remnant system}}} - 1 \quad (5.1)$$

In the ideal case this balance should reside at zero. But even with a perfect jet calibration various effects introduce a bias. Such a bias has already been mentioned in the $\gamma/Z + \text{Jet}$ case in the last section, but it is more pronounced in the multi-jet method, justifying a thorough study which is presented in the next section. As a short anticipatory explanation, the main causes are non-collinear soft gluon radiation favoring the hemisphere opposite the leading jet, as the system of remnant jets is on a softer scale, and the general challenge that all objects in the events are jets, and thus only measured with a certain accuracy.

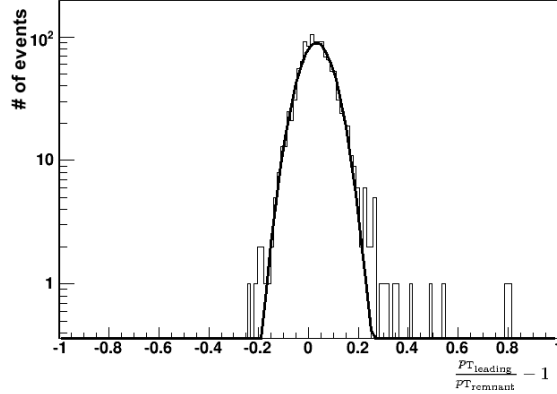


Figure 5.4: Distribution of the multi-jet balance for one sample p_T -bin

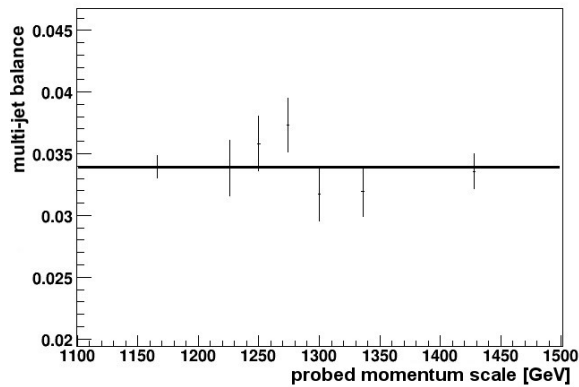


Figure 5.5: Example result of a bootstrapping measurement of the JES

To study the p_T balance a procedure to measure it has to be defined first. All events from one data sample are sorted into a number of intervals, in the simplest case discriminating by the p_T of the leading jet. Figure 5.4 shows an example balance plot for a fixed region of leading jet p_T , the horizontal axis denoting the balance. A Gaussian fit was done to extract the mean value and the error of the mean value, shown in the figure as a thick solid line.

The above is done for a number of different p_T bins, and their mean values and respective errors are shown in figure 5.5 as a function of the probed momentum scale. The JES in the sample used was known and constant in p_T , which is confirmed with an accuracy $<1\%$ by the measurement.

A bias of the balance is visible at a level of a few percent, though. Treating this bias as a systematic error would still be acceptable if the multi-jet bootstrapping

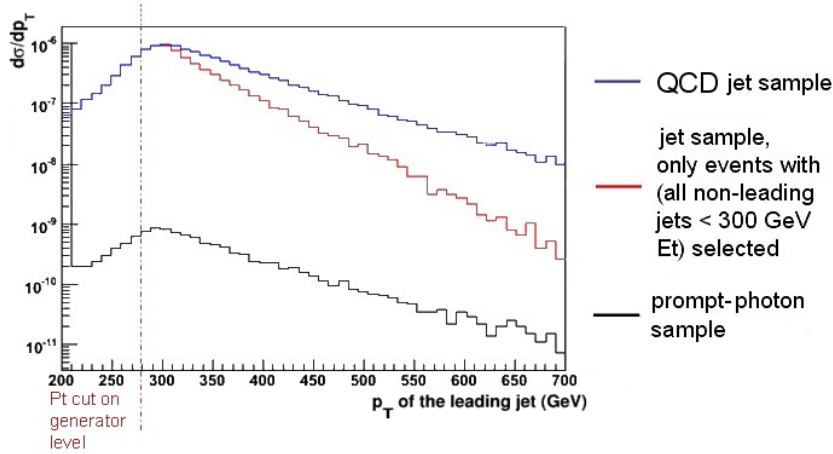


Figure 5.6: jet p_T spectra for inclusive jet production, events selected for the bootstrapping calibration and prompt photon events

method is only applied once. But an iterative use is needed to reach high p_T regions.

As the difference between the maximum allowed p_T of the non-leading jets, to confine them to the reference region, and the leading jet p_T increases, the required event topology includes one or several rather hard gluon emissions from one of the initial partons. The cross section of such events falls rapidly with increasing p_T of the leading jet, and also has tails that are probably not well described by current Monte Carlo generators, as no data of sufficiently hard interactions is available to tune them. Figure 5.6 shows the cross section for prompt photon events as e.g. required in the last section and events available for multi-jet bootstrapping in comparison. Jets with a p_T up to 400 GeV are considered to be already calibrated here, and thus an upper cut on non-leading jet transverse momenta of 300 GeV was used for event selection in the multi-jet case. The number of selected events falls much more rapidly than the inclusive QCD jet sample, being two orders of magnitude lower at 700 GeV of leading jet transverse momentum.

Generally there are two options to counteract the rapid fall of the cross section of events usable for multi-jet bootstrapping. The first one is sorting all events in one data sample with respect to the transverse momentum of the leading jet. Then, starting at low p_T values, a sliding limit on the second highest jet p_T in an event could be used, e.g. restricting it to be at least 30% below the leading jet p_T . In this way one could measure the p_T -balance for the whole sample in one go. The second one is relaxing the p_T cut on the system of non-leading jets iteratively. One again starts at low momentum scales, this time with a fixed limit, and uses the result as a new reference region for the next application, with a higher maximum p_T allowed for the remnant system.

For both approaches the significant bias of the multi-jet p_T -balance poses a non-

trivial challenge. The next section shows that the actual size of the bias is sensitive to the momentum scale of the remnant jet system. As this scale is mainly set by the maximum allowed p_T of non-leading jets, a sliding limit leads to the bias changing with the probed p_T scale. Thus any actual miscalibrations could not be discerned from systematic effects and influences on the bias, as it is impossible to disentangle the two without using generator level information that is not available for real data. As a result, if one does not resort to assuming that the bias is linear and the same as in Monte Carlo data without having any evidence to support this, using multi-jet bootstrapping in that way would be only viable to limit the JES uncertainty, and not to verify it or uncover problems like nonlinearities. Furthermore any actual JES error would add to the JES uncertainty, resulting in higher uncertainties with actual data, compared to expectations derived from a correctly calibrated Monte Carlo sample.

Hence only the second approach, iteratively increasing the limit on non-leading jet p_T , while keeping it constant during one iteration, is able to fulfill the stated goal of providing an accurate measurement of the JES and including possible p_T dependent deviations. The statistics available to calibrate jets of the highest scales is increased by several orders of magnitude compared to a single application of the calibration method with a fixed limit. But, if one considers the p_T -balance bias as a systematic error in the order of a few percent, this would quickly add up in an iterative process.

As a result, during the work described in this dissertation, the decision was made not to treat the whole bias in the p_T balance as a systematic error, but to disentangle constant, expected offsets that can be measured from data from real error sources introduced by the event topology or analysis methods and parameters. Accordingly possible systematic influences are studied in detail in the next section, with the goal to constrain the total systematic error to below one percent. The hypothesis is that for one iteration of the bootstrapping method, the bias is constant in p_T . For more than one iteration a common scale is established by their p_T ranges overlapping and a comparison of the offsets in the overlap regions.

5.2.2 Study of the p_T -Balance Bias

The first step towards an understanding of systematics in multi-jet bootstrapping is identifying the sources of the bias in the p_T -balance. Two main types of influence can be identified. On one hand there are physics effects on the particle level, including jet algorithm effects like out of cone energy, initial and final state radiation, fragmentation and the underlying event. On the other hand instrumentation effects play a role, mainly migration effects due to the jet energy resolution, detector and electronic noise and generally the jet response. Apart from migration effects, which are the biggest influence, particles or energy depositions being lost outside of jets that are too small to be reconstructed as separate objects are a prime candidate. As by design the remnant jet system is much softer than the leading jet, these effects are expected to affect it more strongly, which can intro-

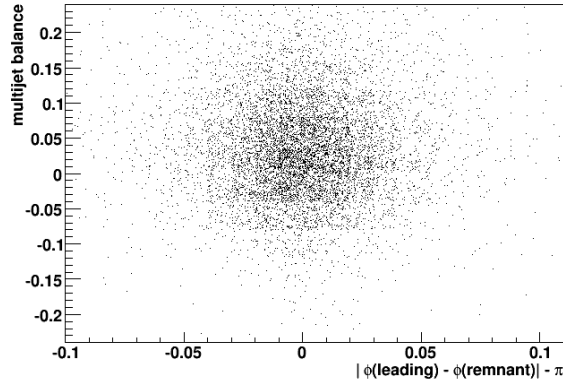


Figure 5.7: Multi-jet balance versus the deviation from a perfect back-to-back topology (in the plane transversal to the beam axis)

duce a bias into the p_T -balance. The leading jet is more collimated resulting in smaller losses outside of a fixed size (in η/ϕ or momentum space) jet. While these losses should be compensated in case of a perfect jet calibration, they may not be negligible for experimental data. These effects and thus the bias were found to be independent from common choices for event selection in p_T balance methods, like the azimuthal angle between the leading jet and reference object, shown in figure 5.7.

In the following the goal is to minimize the bias of the multi-jet balance, as then possible relative fluctuations of the above effects are also expected to be smaller. All decisions are based on this goal.

The event samples used in the following are Monte Carlo generated data, both fully simulated and reconstructed events as well as particle level truth information². The datasets are inclusive QCD jet samples known as J6 and J7 at ATLAS. J7 are events with lower and upper bounds of 1120 GeV and respectively 2240 GeV transverse momentum on the generator level. 170000 events were used, corresponding to an integrated luminosity of 32 fb^{-1} . J6 has limits of 560 GeV and 1120 GeV on generator level, and 300000 events were available, corresponding to 0.87 fb^{-1} . J6 statistics were reweighted to be equal to the J7 sample. All events were generated using PYTHIA and simulated and reconstructed using release 13 of the ATLAS Offline Software, including the full detector and electronics simulation. For this study, the main event selection criterion was discarding events that have non-leading jets of more than 900 GeV transverse momentum, if not stated otherwise. Jets were generally reconstructed up to an $|\eta|$ of 5 and down to a p_T

²particle level truth denotes jets directly based on the particle four momenta output of the Monte Carlo generator

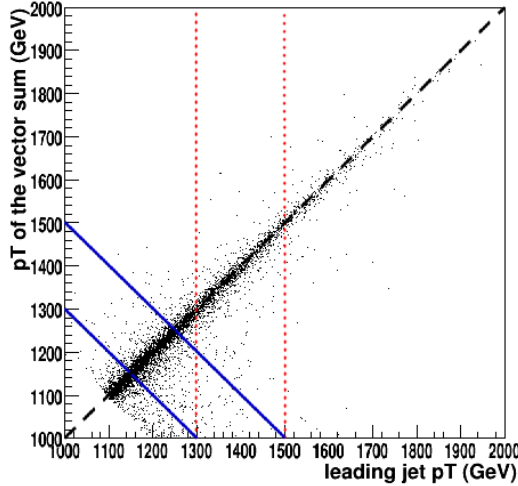


Figure 5.8: Distribution of events in a p_T of the vector sum/ p_T of the leading jet plane. Red dashed lines define an interval based on $p_T^{leading}$, blue on the average of the leading jet and remnant system p_T

of 10 GeV and jet finding and reconstruction was performed with a seeded cone algorithm³ with a size parameter R of 0.7.

Jet Resolution and Migration Effects

One important choice with most p_T -balance methods is the variable used to subdivide the probed momentum scale. Regarding multi-jet bootstrapping the bias of the p_T -balance changes by several percent for reconstructed data, when binning is done on either the p_T of the leading jet, p_T of the system of non-leading jets, or a combination of both. But an influence on the bias is not the only outcome of this choice.

Figure 5.8 illustrates the effects of the binning variable. As a connection between the probed p_T scale and the p_T of a single jet that needs to be calibrated is required, the most obvious choice to select events is by the p_T of the leading jet. An example of an interval thus defined is shown as red dashed lines. This choice introduces a strong bias on the p_T -balance. The interval includes significantly more events below the bisecting line than above, due to the jet energy resolution and the steep fall of involved cross-sections. In these events the transverse momentum of the leading jet has been overestimated in comparison to the non-leading jet sum. Selecting events based on the p_T of the remnant jet system leads to an analogous problem. Furthermore choosing the remnant system as reference causes the measured p_T -balance missing a clearly defined connection to the scale probed

³see section 4.2.1 for details

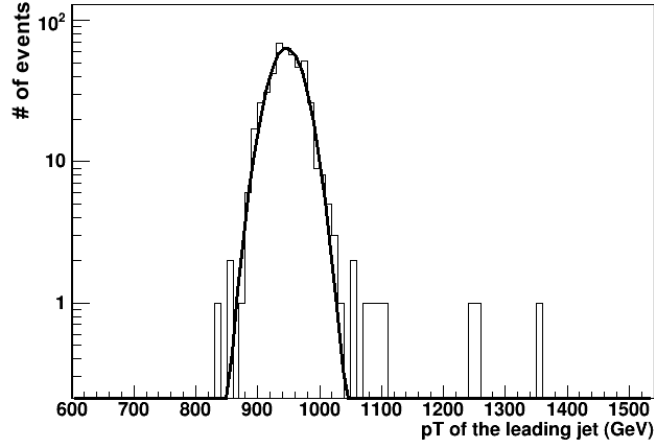


Figure 5.9: Distribution of leading jet p_T of a sample bin defined by borders on $(p_T^{\text{leading jet}} + p_T^{\text{remnant system}})/2$

by the leading jet. Events with broadly varying leading jet momenta would be included in a single data point in the results.

Thus the most sensible choice appears to be using bin borders perpendicular to the bisecting line in figure 5.8, as shown by the solid blue line. Events having an imbalance due to resolution effects cancel each other out on average and the momentum range of leading jets is still relatively narrow and well defined. From now on the measured balance is always connected to the probed momentum scale for single jets by:

$$\text{probed } p_T \text{ scale} \sim \frac{p_T^{\text{leading jet}} + p_T^{\text{remnant system}}}{2} \quad (5.2)$$

After the balance was measured for such subdivisions of the probed p_T scale, the exact region of the JES that was probed has still to be determined. E.g. in the case of a large local nonlinearity of the JES of the leading jet, this nonlinearity would not be visible at the p_T scale of the leading jet, but in between this scale and that of the remnant system p_T , due to the above averaging. To amend this, for each p_T bin one additional histogram containing the transverse momentum of the leading jet only is created. The maximum of that histogram finally sets the scale that was probed by these events. A sample distribution of leading jet p_T values for events assigned to one interval by the above defined average can be seen in figure 5.9. The distributions are generally dominated by the jet energy resolution and thus in good approximation Gaussian, allowing the reliable extraction of the maximum using a fit, even with low statistics.

Using the procedure described above, the bias due to migration between bins caused by resolution effects is minimized.

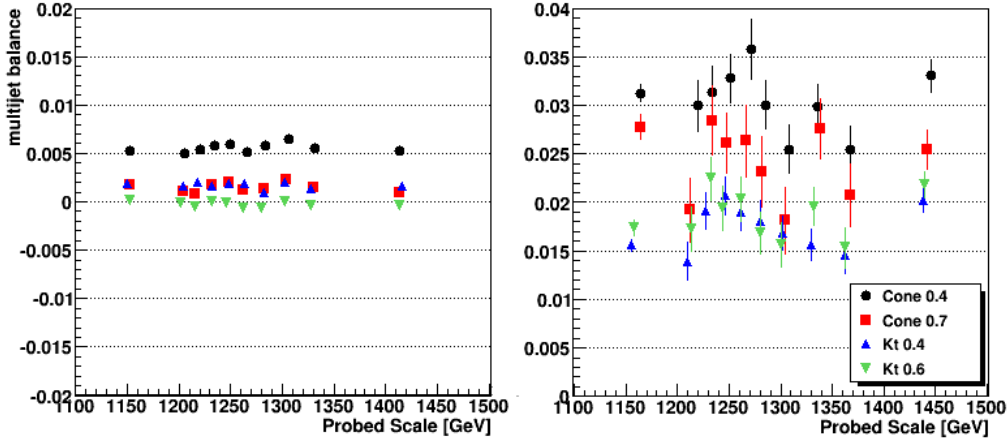


Figure 5.10: Multi-jet balance using differing jet algorithms, shown on the left on particle truth level, and for simulated and reconstructed events on the right

Jet Algorithm

As the multi-jet p_T -balance is expected to be sensitive to out of cone effects, e.g. soft gluon radiation not collinear with hard jets or charged particles curving out of jets due to the magnetic field, the next point of interest is using different jet algorithms and different jet sizes. The jet calibration does include corrections for these effects, eliminating them on average, but for the specific event topology used here these corrections are not necessarily correct, and different algorithms could have different sensitivities to these effects. E.g with high jet multiplicities out of cone losses could be measured as part of another jet thus being double counted after a correction.

Two approaches were studied, the seeded cone jet algorithm, defining jets by using the difference of objects in angles, and k_T jets, by a relative transverse momentum criterium. Details can be found in section 4.2.1.

Figure 5.10 shows the result using particle level truth data on the left, and fully simulated and reconstructed data to the right. Using particle truth jets, the cone algorithm with a size of 0.4 appears to suffer from particles not reconstructed as part of any jet, while the other choices result in a very small bias. After simulation and reconstruction of the event, differences are visible between the algorithms, but no algorithm can reduce the bias below one percent. On this level the bias is also sensitive to the jet response and calibration, though, which is not perfect even for Monte Carlo samples. This is studied later.

From both figures no clear arguments for or against one jet algorithm, apart from the Cone 0.4, present itself. The seeded cone algorithm with a size $R = 0.7$ is used exemplarily from now on.

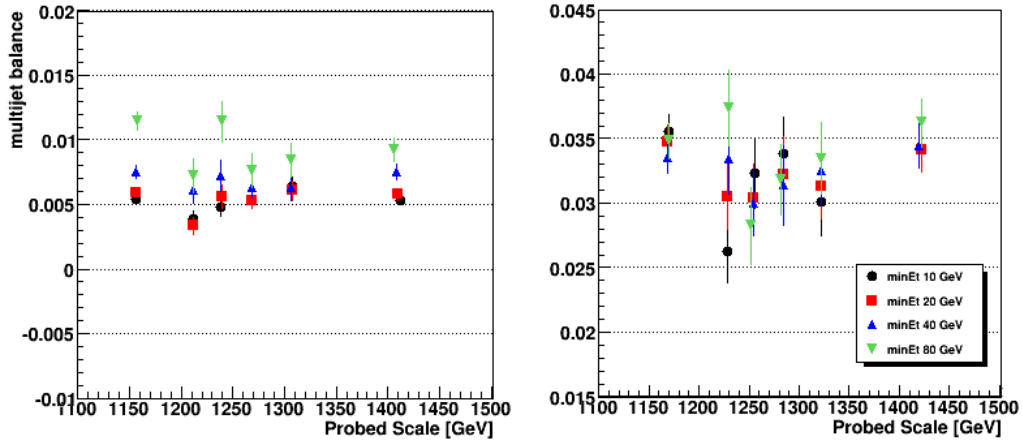


Figure 5.11: Multi-jet balance using different cuts on minimum jet p_T , particle truth level on the left, reconstructed events on the right

Lower p_T Threshold for Non-Leading Jets:

A minimum transverse momentum criterion for all jets is always present in data, thus only jets passing this threshold can be included in the vector sum to balance the leading jet. This criterion is either done implicitly by the minimum p_T required for jet candidates to be reconstructed by the ATLAS software, by the jet finding efficiency, or explicitly by a user choice. Such a user selection could be included to e.g. suppress fake jets from calorimeter noise or very soft jets from the underlying event.

Due to this lower threshold on jet p_T , soft jets or energy depositions landing out of cone are not always reconstructed as separate objects, and thus are missing from the p_T -balance. In figure 5.11 the threshold was varied from 10 GeV up to 80 GeV to study its influence, on the left side on particle level and on the right side for simulated and reconstructed data. This criterion does have a measurable influence on the balance, but it is by far not sufficient to explain the full bias.

Jet Response:

As the two candidates described above can not fully explain the significant bias visible in the multi-jet balance, the jet response in the simulated sample has to be studied. While the calibration in the Monte Carlo data is done using truth information unavailable in experimental data, and thus very accurate, uncertainties of the order of percent can still remain. The deviation from an ideal jet response is shown in figure 5.12 in dependence on the true jet p_T , to eliminate migration effects.

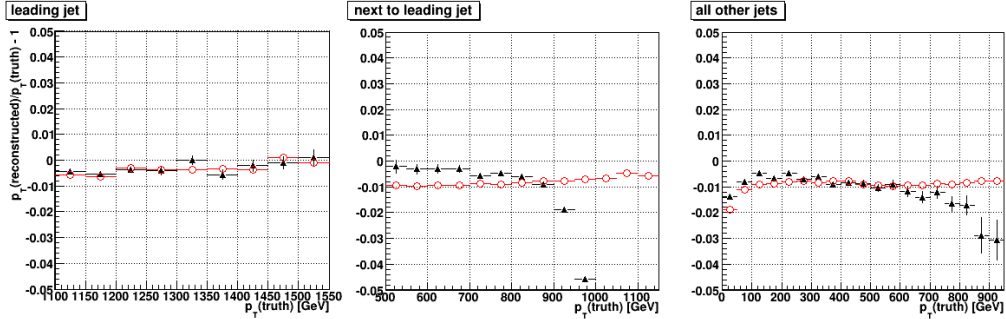


Figure 5.12: The solid black markers are the deviation from a perfect jet response in the Monte Carlo sample, for events selected for bootstrapping and (from left to right): the leading jet, the jet with the second highest p_T , all other jets in an event. The open red circles were obtained including all jets in the sample without any selection.

This deviation is defined here as:

$$\frac{p_T^{\text{measured}} - p_T^{\text{true}}}{p_T^{\text{true}}} - 1 \quad (5.3)$$

The open red circles in the figure are the determined miscalibration for the full QCD jet sample, without using any event selection or any discrimination between leading or other jets. Hence all three plots show parts of the same distribution. The jet response is nominal at high values of jet p_T , but is up to 2% too low below 1 TeV. To check the influence of this jet calibration error on the multi-jet balance, correction factors were calculated and applied and the bootstrap calibration was redone. Figure 5.13 shows the measured multi-jet balance before and after the correction as open data points. As the correction relies on Monte Carlo truth information, and is only done to study the bias, it is not applicable to real data. Furthermore it changes the multi-jet balance by less than one percent, and thus falls short of explaining the full bias.

The next study examines migration effects due to the jet energy resolution. It was already shown that the probed scale is determined in a way that minimizes the bias through migration effects at the bin borders for multi-jet balance histograms. But the upper limit of allowed p_T for non-leading jets can also cause a bias due to the jet energy resolution. The solid black data points in figure 5.12 were determined as above, but only events with no measured non-leading jet p_T above 1 TeV were selected. Additionally the jet response measurement was done separately for the jets of these events. For the leading jet the response is consistent with the case of not using any event selection, but the next-to-leading jet and all further jets show significant deviations. The response drops sharply in the regions of true jet p_T close to the maximum allowed measured p_T . The cause of this are events in which

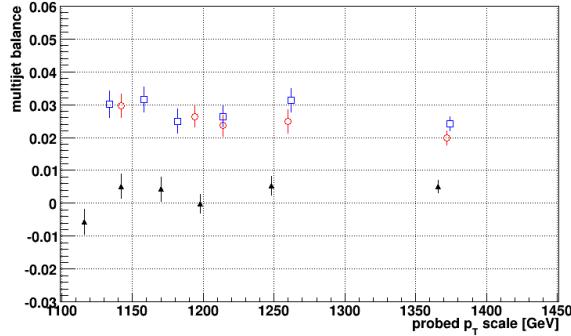


Figure 5.13: Multijet balance before (open blue squares) and after (open red circles) the application of correction factors to account for the jet response (see Figure 5.12). For the solid black points migration effects due to the event selection were additionally taken into account.

these jets were reconstructed with a higher momentum than their true value being discarded during event selection. Hence jets with a ratio of reconstructed to truth p_T below 1 dominate the selected events in that region. Since the cross section decreases as the difference of leading and next-to-leading jet p_T increases, most next-to-leading jets are expected to be found close to the threshold thus causing a significant bias of the multi-jet balance.

Again correction factors can be determined for the jet response, and a multi-jet balance after correction is shown in figure 5.13. The result has a bias of less than one percent, which is comparable to multi-jet bootstrapping using Monte Carlo particle level information, e.g. in figure 5.11 on page 73.

It can be concluded that the dominant source of bias in the multi-jet bootstrapping method is the event selection on non-leading jet p_T . This also explains why the bias strongly depends on that cut, as the non-constant jet energy resolution determines its magnitude.

5.2.3 Systematic Effects and their Influence on Multi-Jet Bootstrapping

The working hypothesis regarding the bootstrap calibration of the JES using multi-jet events is that while the p_T -balance defined in the last section has a measurable bias, it is constant for one iteration of the method. One iteration essentially means that the allowed p_T range for non-leading jets is fixed, and thus the momentum scale of the remnant jet system is expected to likewise stay the same. As a result, the bias itself is not treated as a systematic error, but only deviations of the bias from a constant influence the uncertainty of a bootstrapping calibration.

While the hypothesis holds true with very high precision for Monte Carlo data

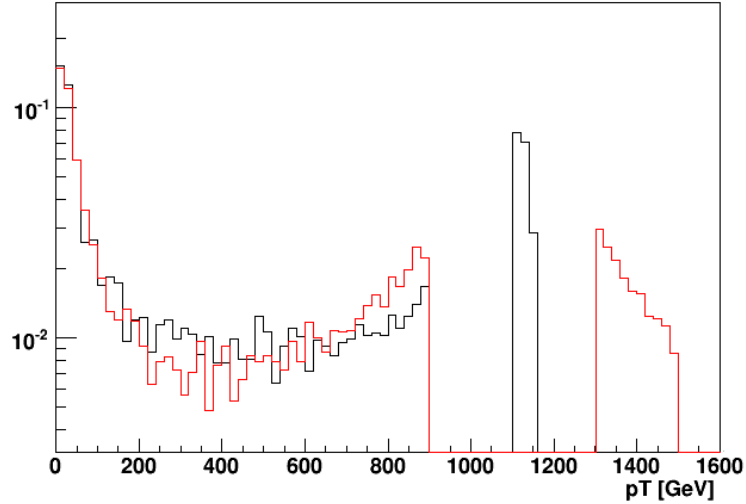


Figure 5.14: Inclusive jet spectrum after event selection, for two different p_T bins (shown in black and red)

on particle level, as can e.g. be seen in figure 5.10 on page 72, this has to be verified using simulated and reconstructed data.

Before going into detail, the actual distribution of non-leading jets is examined. Figure 5.14 shows the inclusive jet spectra for events passing the following criteria:

- More than two jets have been reconstructed
- The second highest jet transverse momentum is below 900 GeV
- The leading jet has a p_T between a) 1100 and 1160 GeV (shown in black) or b) 1300 and 1500 GeV (shown in red)

Both distributions were normalized to an area of one for comparison. The interval containing the leading jets can be clearly discerned on the right of the distributions, while all non-leading jets can be found below 900 GeV.

Due to this event selection on transverse jet momenta of the remnant system the distributions look very similar. For the higher probed scale the remnant system is slightly harder with a higher percentage of the jets having large p_T values close to the threshold. As the hypothesis that the balance of the bootstrapping calibration stays constant is based on the assumption that the system of non-leading jets essentially stays the same, independent of the leading jet p_T , further study is needed.

In the following section, possible sources for fluctuations of the bias are examined in detail in order to quantify possible systematic errors. To study such deviations

from a constant they were split into two components. The first component is a potential global slope in p_T , determined using a linear fit. The maximum relative change to the bias resulting from that slope is provided including its error. This is complemented by the spread of the single values from a constant to quantify possible local deviations. The constant is set to the mean value of measured balances. Two quantities are calculated. First the expected standard deviation of the balance values in case the hypothesis would be true, based on pure statistics and under the assumption that statistics are comparable for all measurements:

$$spread_{expected} = \frac{1}{N} \sum_{i=1}^N \sigma_i \quad (5.4)$$

Secondly the estimation of the standard deviation from the actual spread of the data points:

$$spread_{data} = \sqrt{\frac{1}{N} \sum_{i=1}^N (x_i - \bar{x})^2} \quad (5.5)$$

whereas N = number of data points/measurements, σ_i = error of the mean of one bin, x_i are the measured values of the balance and \bar{x} their arithmetic mean.

Anticipatory, the magnitude of both these effects is generally of the order of the statistical errors, and the results using simulated data are compatible with the hypothesis of the multi-jet p_T -balance being constant in p_T . Therefore this split of possible deviations into two independent components is feasible, as is their treatment. While the bias is compatible with being constant, an effort is nonetheless made to establish conservative upper bounds on possible systematic influences, individually for each effect and in total.

The Monte Carlo data used in the following consists of the same samples used in the last section, a total of 470000 events, corresponding to 32 fb^{-1} .

All numbers are primarily included for reference, the results are summarized and discussed together after all individual introductions.

Candidates for Systematic Error Sources

Migration Effects Revisited: As previously stated the expectation is that migration effects resulting from the jet energy resolution are highly suppressed by the choice of variable to set interval borders. Hence the actual choice of upper and lower p_T limits for probed multi-jet balance intervals should not cause deviations from a constant. To verify this, the probed p_T region was first divided into intervals of constant size, and then of strongly varying size.

The left side of figure 5.15 shows the p_T -balance for both these choices. The results are compatible and the following table contains the measured deviations from a constant bias, together with their statistical errors:

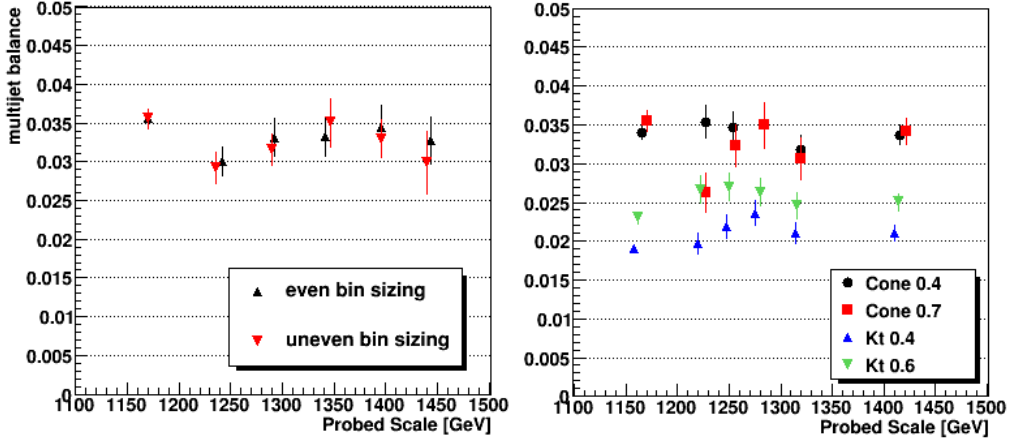


Figure 5.15: Left: Dependence of the multi-jet balance on the bin sizing/spacing. Right: Dependence on the jet algorithm.

		even bins	uneven bins
linear fit	slope	-0.30%	-0.50%
	error of the slope	0.37%	0.38%
spread	data	0.17%	0.26%
	expected	0.23%	0.25%

The p_T -balance does not appear to be influenced by the actual choice of intervals.

Jet Algorithm: It was previously found that the choice of jet algorithm can introduce a small bias into the p_T -balance. The right side of figure 5.8 shows results with both cone and k_T algorithms, and two different choices for the jet size parameter each. All four are compatible with the hypothesis of a flat bias, and the choice of the jet algorithm does not appear to have a systematic influence on the result.

The respective deviations from a constant balance, together with their statistical errors, are included in the following table.

		cone 0.7	cone 0.4
linear fit	slope	-0.14%	-0.10%
	error of the slope	0.33%	0.24%
spread	data	0.33%	0.12%
	expected	0.23%	0.17%

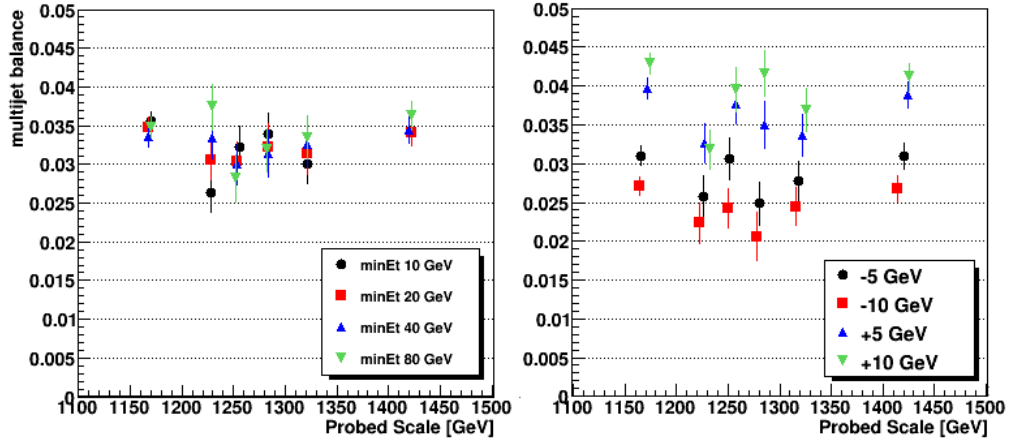


Figure 5.16: Left: Dependence of the multi-jet balance on the minimum jet p_T . Right: Influence of an incorrect underlying event correction

Minimum p_T of Non-Leading Jets: The minimum p_T for jets to be included in the non-leading jet vector sum can introduce a bias into multi-jet bootstrapping. Therefore it is important to verify that this bias is independent of the probed p_T scale, and as a result does not influence the accuracy of the bootstrapping calibration.

An allowed minimum p_T of non-leading jets was introduced, ranging from 10 to 80 GeV. This is no event selection criterion, but only governs which jets are included in the vector sum to create the composite reference object.

As can be seen in figure 5.16 on the left, the bias of the p_T -balance shifts by the order of half a percent, but appears to stay constant regardless of the exact threshold used. The precise results can again be obtained from the table below:

		10 GeV	20 GeV	40 GeV	80 GeV
linear fit	slope	-0.20%	-0.11%	0.11%	0.14%
	error of the slope	0.33%	0.36%	0.33%	0.36%
spread	data	0.33%	0.19%	0.16%	0.31%
	expected	0.23%	0.23%	0.24%	0.24%

Underlying Event: Another consideration regarding the bootstrapping method are contributions of the underlying event to the jet momenta. While the expectation is that about 1-3 GeV add to each jet, the actual contribution is highly dependent on the gluon parton distribution function plus the spatial distributions of these gluons in the proton, and may thus at the moment not be well described.

The average energy deposited per jet by the underlying event will be estimated starting with the earliest LHC data, in order to correct for it, but there could still be large uncertainties involved. A non-perfect correction would mainly influence the remnant jet system due to the larger number of jets, and could thus introduce a bias. To study the effect of these uncertainties the bootstrapping calibration was done while adding 5 to 10 GeV to or subtracting that from every reconstructed jet. A non-optimal correction of detector and electronic noise would have the same influence, a p_T independent addition or subtraction of measured energy, and is thus studied simultaneously by this test.

The result can be seen on the right side of figure 5.16. While the bias is sensitive to fixed contributions to each jet, the effect is in good agreement with being constant in p_T .

		-5 GeV	-10 GeV	+5 GeV	+10 GeV
linear fit	slope	-0.03%	-0.08%	-0.13%	-0.19%
	error of the slope	0.32%	0.32%	0.34%	0.34%
spread	data	0.27%	0.26%	0.29%	0.39%
	expected	0.23%	0.23%	0.23%	0.24%

JES of the Remnant System: The JES of the non-leading jets is another uncertainty for experimental data. If the absolute JES is determined using the bootstrapping method, by utilizing an already calibrated low p_T reference region, the calibration in that region will never be perfect and only be known to lie within the bounds of the JES uncertainty. The JES uncertainty is expected to be in the range from 10% to 1% depending on the available amount of data. Now if e.g. the jet response is off by 5% independently of jet p_T , we do not expect any change in the multi-jet balance, as the contributions cancel out. It is nonetheless advisable to check if a difference in JES between the leading jet and the non-leading jets has an influence on the p_T -balance and a possible slope. The more interesting case is if the jet response is not constant in the reference region, but is compatible with a constant considering involved uncertainties.

Both these cases have been simulated, the first by globally increasing and lowering the scale for the remnant system by 5% and 10%, the second by introducing a linear, non-constant JES error. This was done such that the JES is nominal at 1 TeV, but drops or rises when going to lower p_T values, by up to 5% or 10% when the momentum approaches zero. The results can be seen in figure 5.17. For both cases no measurable systematic influence on the p_T -balance can be found, apart from a constant shift.

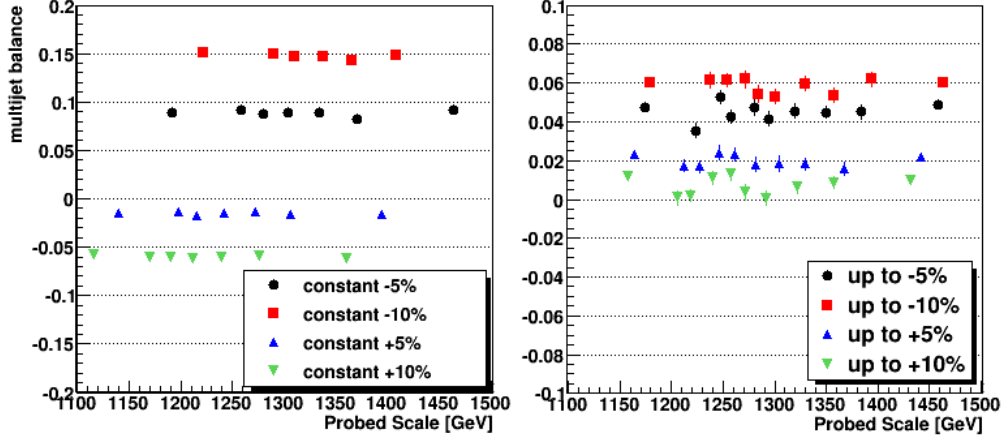


Figure 5.17: Left: Influence of a constant JES error in the reference region. Right: The same for a non-constant JES error.

constant JES		+5%	+10%	-5%	-10%
linear fit	slope	0.10%	-0.21%	-1.28%	-0.59%
	error of the slope	0.26%	0.23%	0.48%	0.22%
spread	data	0.17%	0.15%	0.30%	0.31%
	expected	0.17%	0.15%	0.21%	0.24%

non-constant JES		+5%	+10%	-5%	-10%
linear fit	slope	-0.19%	-0.34%	-0.16%	0.06%
	error of the slope	0.32%	0.32%	0.34%	0.32%
spread	data	0.32%	0.46%	0.48%	0.35%
	expected	0.30%	0.32%	0.30%	0.34%

Upper p_T Bound for Non-Leading Jets: One required event selection done by the user is restricting the p_T of non-leading jets to a certain maximum value, which lies outside the probed p_T region of the current iteration of the bootstrap calibration. Ideally this threshold is a few times the JES resolution below the lowest probed p_T to ensure that the leading and next-to-leading jets are indeed on a different momentum scale.

The p_T distribution of the jet with the second highest transverse momentum, for events with leading jet momenta above 1.1 TeV, is shown in figure 5.18 on the left. The selection on the non-leading jet momenta is not only the main event selection criterion, but was also shown to be the dominant source of the

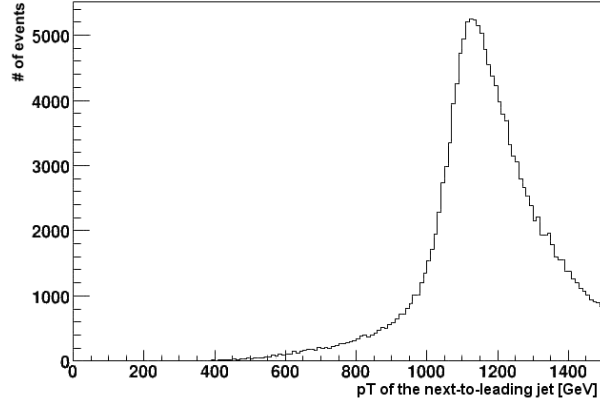
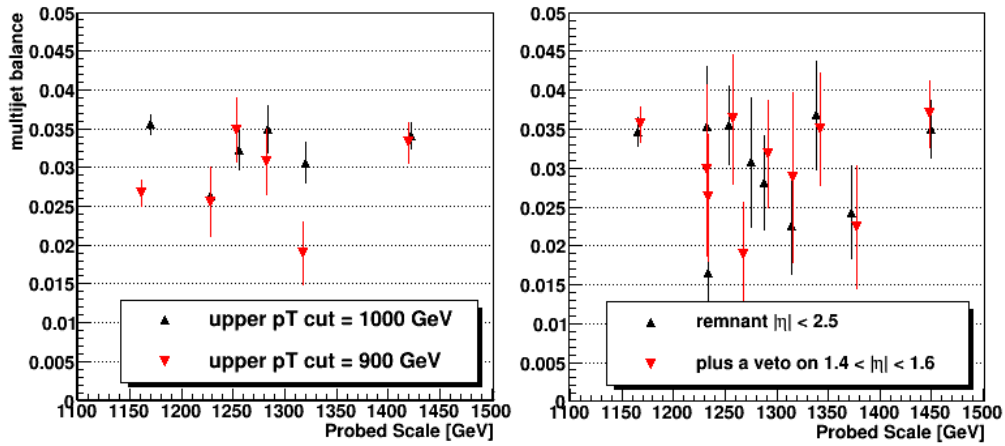


Figure 5.18: Distribution of the second highest jet transverse momenta

Figure 5.19: Left: Dependence of the multi-jet balance on the upper cut on non-leading jet p_T . Right: Influence of cuts on the η of remnant jets.

bias. Therefore on the left side of figure 5.19, it was varied by 100 GeV to study possible effects on the bias of the p_T -balance. As can be seen, both results are compatible with a constant, and thus a systematic influence, if present, can be strongly constrained.

		1000 GeV	900 GeV
linear fit	slope	-0.14%	0.78%
	error of the slope	0.33%	0.47%
spread	data	0.57%	0.64%
	expected	0.32%	0.52%

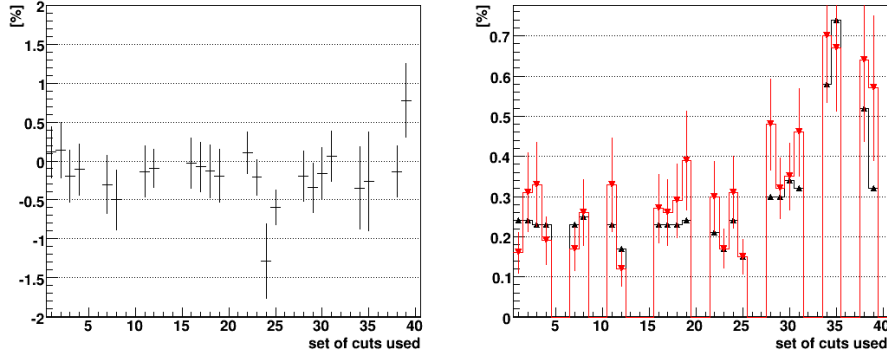


Figure 5.20: Summary of possible systematic error sources, for all studied sets of cuts, given in the tables. Left: Distribution and errors of the slopes of one iteration. Right: Average statistical error and measured spread(dashed red line) of the multi-jet balance data points

η of Non-Leading Jets: As an example, it may be required to disregard certain areas of the detector with respect to the measurement of jets during early data taking at ATLAS. Forward jets could for example be excluded from the system of non-leading jets, or certain η regions like the transition from the barrel to the end-cap calorimeters, where the jet calibration is expected to be imprecise at first. While it is envisioned that the jet inter-calibration in η and ϕ can be done with a high precision before applying the multi-jet method, some limit for the η of non-leading jets is always in effect. To test the influence on the multi-jet p_T -balance non-leading jets were first constrained to $|\eta| < 2.5$. In a second step a veto on $1.4 < |\eta| < 1.6$ was additionally introduced. The result can be seen in figure 5.19 on the right. The absolute bias changes and statistical errors increase, as the remnant system loses momentum if one or more jets fall outside the allowed regions, but the bin averages are still compatible with being constant in p_T .

		constraint	+ hole
linear fit	slope	-0.35%	-0.26%
	error of the slope	0.53%	0.63%
spread	data	0.70%	0.67%
	expected	0.58%	0.74%

Conclusions: In order to precisely apply an iterative bootstrapping method to data the multi-jet balance has to be constant for one iteration, or any deviations at least be constrained to a know size.

All Monte Carlo estimates of a possible slope or local deviations from a constant bias are summarized in figure 5.20. The measured slopes, shown on the left, are

generally compatible with being zero. A projection of all slope values onto the y-axis results in a mean value of $-0.09\% \pm 0.04\%$, and a standard deviation $\sigma = 0.28\%$. This σ is perfectly compatible with the assumption of a purely statistical distribution of measured slope values, as the average statistical error of the slopes is around 0.3%.

To quantify an expectation for a possible slope caused by the conditions and analysis choices for experimental data, despite all measurements being compatible with a constant for Monte Carlo data, a value of $-0.09\% \pm 0.04\%$ is chosen as a possible slope. Additionally, for a single parameter set the statistical uncertainty of around 0.3% is added, representing our sensitivity to a possible slope. This results in a conservative upper bound of 0.3% for systematical deviations from a constant bias caused by a non-zero slope.

The right side of figure 5.20 combines all actual spreads of single data points and the expectations from pure statistics. These values are generally compatible, but on average the actual spreads appearing to be $0.05\% \pm 0.02\%$ higher. The distribution of the differences of all sets, centered on that value and having a $\sigma = 0.08\%$, is in good agreement with the average error of the measured spread of around 0.1%. As an additional spread due to systematic effects would add in quadrature to the pure statistical spread, the figure and above numbers result in a very conservative limit of 0.4% for an additional error of a single bootstrap measurement.

In summary, both types of possible deviations from a constant bias combined are believed to result in a total systematic error of 0.5%, which is very likely a conservative overestimate as single deviations enter into both components.

Plans and Viability for Data Taking

In order to apply multi-jet bootstrapping to data, one has to be sure that, for the case of a perfect calibration of reconstructed jets to the particle level, the bias of the balance stays constant in p_T , or at least only deviates by a known measure. The last sections summarized studies of known possible sources for a non-constant bias using Monte Carlo data. This has of course to be redone with experimental ATLAS data. Systematic effects of analysis choices on the deviations from a constant bias, as well as the other above mentioned issues, can be determined in any p_T region where the multi-jet balance is reasonably flat with standard choices, as no Monte Carlo truth information or absolute JES is required.

The more challenging task would be to prove that the multi-jet balance is supposed to be constant for one iteration using data only. While it can be verified in a reference region calibrated by another in-situ method, this is limited by the JES uncertainty, and results are not necessarily be applicable to higher momentum scales. Thus in the following arguments are given why the hypothesis of a constant multi-jet balance is expected to be true in case of a perfect jet energy calibration.

A possible starting point is the selection of events with exactly three recon-

structed jets above the minimum p_T threshold. With this simplification physics effects are considered first. On parton level it is clear that the two final state partons and the radiated gluon of a QCD three jet event always have to be balanced in transverse momentum. Thus the following physics options remain for the hypothesis to fail:

- The jet sample is not dominated by hard QCD parton scattering, but has a significant contribution by some process that produces highly energetic particles that are not registered by the ATLAS detector, like neutrinos or e.g. possibly gravitons
- Our Monte Carlo description of fragmentation, showering or jet shapes is significantly wrong

The first item, new physics producing missing transverse energy with a cross section rivaling QCD jet production, could result in a bootstrapping calibration providing largely wrong results. Significant missing transverse momentum would introduce a non-constant bias, changing with the relative cross section of the production process. But any such process would likewise influence any dijet balance methods, as e.g. used for the η and ϕ inter-calibration of jets. While the p_T inter-calibration could interpret these new physics as a JES error attributed to certain p_T scales, e.g. the dijet balance methods for ϕ would not be able to attribute it to a ϕ value and thus clearly show that inclusive jet events do not conserve measured momenta. Thus no risk to “calibrate the signal away” is present in that case. Multi-jet bootstrapping would not be applicable, as it requires a sample mainly consisting of QCD jet production, but also would not produce wrong results or hide new physics.

The second case, a significant difference in the creation and simulation of jets using Monte Carlo samples compared to real data is much more likely. Any such effects can be divided into effects that are either only p_T dependent or depend on at least one other variable, like the parton type. In the second case, as jet and shower shapes will be measured in data to obtain a calibration any significant discrepancies should be considered a physics discovery. In the first case the multi-jet bootstrapping measurement would show that the JES calibration is off by some amount, which would actually be true despite it being possibly a new insight into physics.

If none of the above new physics, either fundamental processes or behavior of quarks and gluons, is present, any deviation of the JES measured by the bootstrapping method is by definition a miscalibration, and the method rightly sensitive. Examples of possible effects are significantly different jet or shower behavior at high momentum scales leading to wrong corrections of jet particles leaking into the muon system or dead material of the detector, or wrong calibration from the electromagnetic to the hadronic scale based on faulty assumptions on shower shapes.

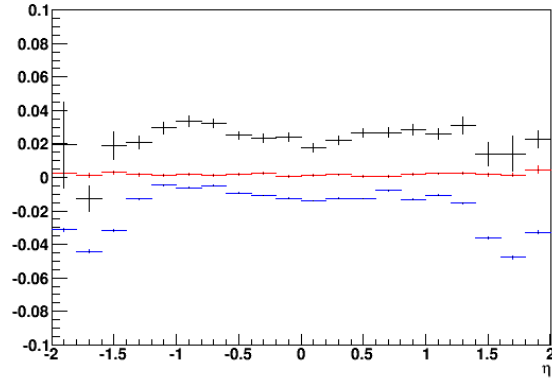


Figure 5.21: η dependence of the multi-jet balance for reconstructed jets(blue) and truth jets(red), plus the jet response(black)

Considering e.g. the case of just three jets, it is clear that if no radical new physics are present, our measured transverse momenta should be conserved, independent of the actual p_T values, if our calibration to the particle level is correct. Thus multi-jet bootstrapping is viable and the hypothesis can be considered true.

As a final note on considerations for the ATLAS data taking phase, one definite measurement that has to be made to validate the bootstrapping calibration is to use exclusive samples based on the jet multiplicity of events. Thus any errors of the jet reconstruction or calibration that are dependent on the topology can be checked. A possible event selection on jet multiplicity, which was not necessary in Monte Carlo data, can be considered if problems are encountered.

Other Systematic Influences

Leading Jet η : Multi-jet bootstrapping is not envisioned to provide a jet intercalibration in η . This is expected to be done using dijet balance methods with higher statistics and thus accuracy. Therefore the aim of the bootstrapping calibration is to use a well understood region in η for the probe and reference jets, while not reducing statistics too much. The case of reference jets was already studied and only a test of an influence of the leading jet η in simulated data remains to be done.

Figure 5.21 shows multi-jet bootstrapping results in bins of leading jet η , in black for reconstructed and in red for truth jets. The following event selection criteria have been applied:

- More than two jets are reconstructed
- The second highest jet transverse momentum is below 1000 GeV

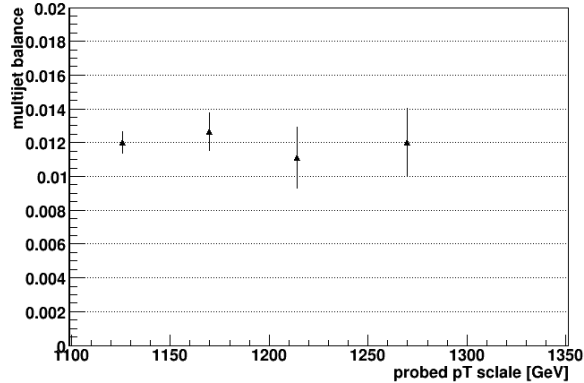


Figure 5.22: Bootstrap calibration result using an ALPGEN sample

- The leading jet has a p_T between 1100 and 1600 GeV

While the result is flat in η for particle level truth information, the result using reconstructed jets shows a structure. The third distribution plotted in figure 5.21 is the jet response in the sample in dependence of η . Comparing the distributions, it can be concluded that the deviations from a flat multi-jet p_T -balance in η are a result of residual JES miscalibrations in η , which are present in the simulated sample. The inter-calibration in η is also worked on in the ATLAS group at the University of Heidelberg, and using the methods described by Pavel Weber in his thesis [30], it can be significantly improved in Monte Carlo data, with the same being expected for real data. Still, to stay clear of the most critical η -region, the transition from the barrel to the end-cap calorimeters around $\eta = 1.5$, the absolute value of the leading jet η is constrained to be less than 1.2 in all following studies. 82% of the events survive this criterion, increasing statistical errors by 10%.

ALPGEN The PYTHIA approach to take the QCD process at the leading order of perturbation theory and combine it with an all-orders approach for initial and final state radiation, may currently not be best suited to estimate expected cross-sections and distributions for the topologies required for multi-jet bootstrapping. This is a result of the absence of any jet data at the respective energy scales that would allow its tuning. Thus as a double-check a comparison with ALPGEN [32] was done. While ALPGEN is also a Monte Carlo generator working with the leading order of perturbation theory, for QCD jet production with up to 6 final state jets the exact matrix element is calculated on parton level.

The result using ALPGEN is shown in figure 5.22. As the largest difference to PYTHIA is expected in the hard tails of the gluon radiation momentum distributions, a very strict event selection on the non-leading jet p_T was used for the ALPGEN sample. All non-leading partons were required to have parton level

transverse momenta below 600 GeV while the leading transverse momentum is higher than 1 TeV. As the fraction of these events in an inclusive sample is very low, the selection was applied on generator level before full simulation of the events, which is the most time consuming step.

While the bias of the multi-jet balance is different from previous figures, as expected due to the significantly different cut on non-leading momenta, the measurement is perfectly compatible with a constant balance.

5.2.4 Multi-Jet Bootstrapping Applied and Expected Results

A method to verify and improve the JES calibration in-situ, up to very high jet momentum scales, was introduced. Its basic idea can be described as an inter-calibration in jet p_T , calibrating a high p_T probe region using a known low p_T reference region. The p_T -balance of this method is not perfect, but shows a bias. This bias has not only been studied with respect to its constituents but the prerequisite for the use of the method, that this bias is largely independent of the probed momentum scale, was established for Monte Carlo data. The expectation derived from simulated data is that systematic errors introduced by possible deviations from a flat bias lie below 0.5%.

With the framework and characteristics of multi-jet bootstrapping fully in place, this section concentrates on expected results and accuracies. This is done in detail for a dataset with an integrated luminosity of about 32 fb^{-1} , corresponding to a few years of data taking. Further results are then given for expected first ATLAS data, with an integrated luminosity of 100 pb^{-1} , plus for a large sample of 100 fb^{-1} , in order to estimate JES uncertainties for physics studies requiring high integrated luminosities.

As the first ATLAS data is now expected to be recorded with an LHC center of mass energy of 10 TeV, the results for this case and 100 pb^{-1} are also presented.

Theoretically all estimates are dependent on the actual cross section for selected events. Apart from e.g. uncertainties of the particle distribution functions used to generate the events, the required topology resides at the hard tail of gluon radiation probabilities. Thus the cross-sections could additionally not be well described by our current Monte Carlo generators. Conservatively assuming a 50% error on the effective cross section of selected events, this would increase statistical errors by 22%.

This is not explicitly included in the following, as generally the binning was chosen such that the systematic errors dominate for the majority of the p_T reach. If the actual number of events available in data is significantly lower than expected, the number of bins and thus resolution in p_T can be reduced to reach the same accuracy for all but the highest probed p_T intervals.

General Approach and Detailed Results

The first Monte Carlo sample used corresponds to 32 fb^{-1} of integrated luminosity, with the total number of events being 364800. The sample was acquired by combining different samples with non-overlapping p_T selection intervals on generator level. The lowest p_T interval has a lower limit of 560 GeV. All samples were simulated and reconstructed using version 13 of the ATLAS Offline Software, including a full detector and electronics simulation, the full event reconstruction algorithms and a jet calibration. Analysis parameters are as follows:

- $|\eta|$ of the leading jet is required to be below 1.2
- more than two reconstructed jets are required
- non-leading jets down to 30 GeV p_T and up to an $|\eta|$ of 2.5 are used for the momentum vector sum
- a seeded cone algorithm with size $R = 0.7$ is used for jet finding and reconstruction
- events are allocated to intervals based on the average of the leading jet and remnant system p_T

It is assumed that the JES was calibrated in-situ up to 600 GeV with an uncertainty of 3%, using other methods and to the particle level (see section 5.1). Systematic errors introduced by one iteration of the multi-jet calibration are considered to be 0.5%, as established in the previous sections. Further choices were bin borders for individual probed scales that result in bins with nearly even statistics. As the cross section for usable events drops rapidly, statistical errors were allowed to become slightly larger for bins at higher probed momenta, in order to preserve some resolution in p_T and counteract extremely broad bins. The goal was to keep the errors of individual bins below 1%, to be small against the JES uncertainty in the reference region. An exception to the general binning strategy is the first bin of each iteration, which overlaps with the reference region or previous iteration and establishes the common scale, called reference bin from now on. Its size is arbitrarily set larger to ensure high statistics, as its error has to be considered a systematic uncertainty for the rest of the bins. The result using statistical errors only is shown in figure 5.23, and is discussed in the following.

The first iteration of the bootstrap calibration method, shown in black, starts with the reference bin lying below 600 GeV. The maximum p_T allowed for non-leading jets was set to 450 GeV. For this iteration the total error on the JES measurement is assumed to be the following:

- A systematic error of 0.5%
- The statistical error of the reference bin, around 0.15%

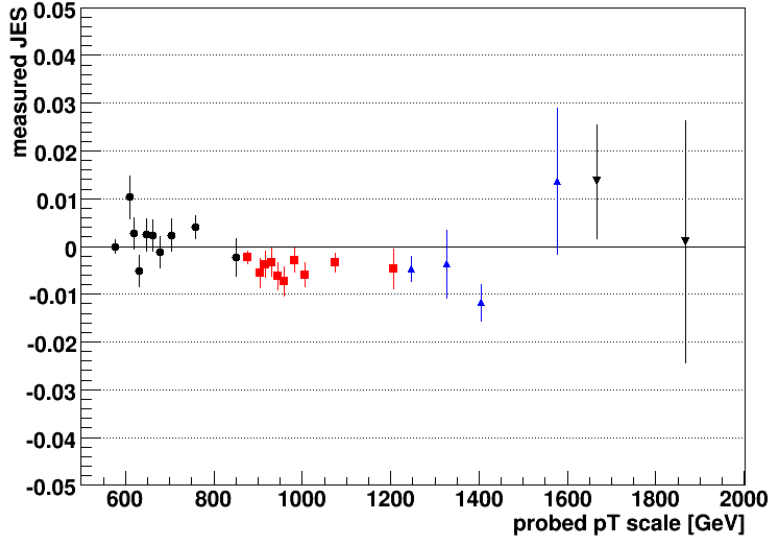


Figure 5.23: Bootstrap calibration result, statistical errors only. The colors/markers highlight different consecutive iterations of the basic method.

- For a single resulting data point, its own statistical error

The JES uncertainty in the reference region is included as a global uncertainty of the absolute JES in the end, and thus not individually for each iteration. After the multi-jet p_T -balance measurement, the balance was shifted by a fixed constant to bring the reference bin to 0. The deviations from zero presented in figure 5.23 thus represent deviations from the target value of the balance, which corresponds to the JES of the reference region.

The second iteration, shown as red squares in the figure, has an upper p_T bound of 750 GeV for the non-leading jets. It was shifted such that the p_T -balance value of the reference bin is identical to the balance of the highest p_T data point of the first iteration, to get a reference to the original reference region and thus the absolute JES. Additional errors are introduced, which are treated as systematic errors for the next iteration:

- A systematic error of 0.5%
- The statistical error of the last bin of the first iteration
- The statistical error of the reference bin of this iteration

For the third iteration, the jets of the remnant system were confined to being below 1150 GeV. Additional systematic errors are another 0.5%, the statistical

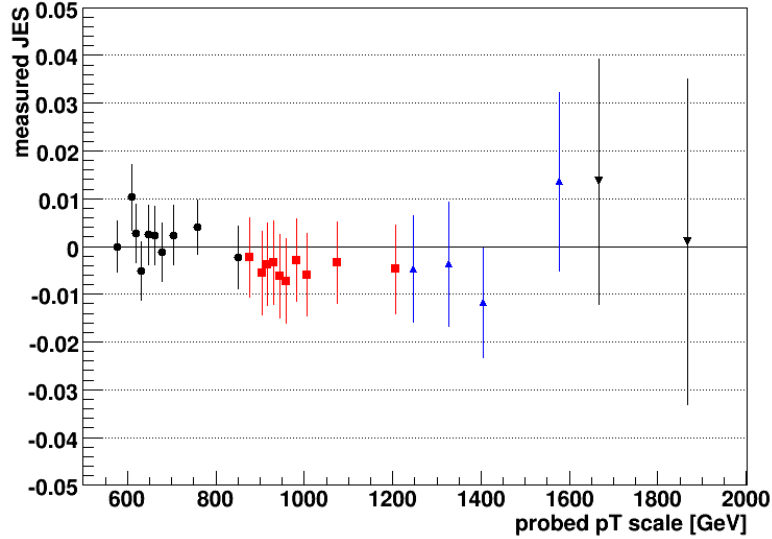


Figure 5.24: Bootstrap calibration result, including systematics

errors of the last bin of the second iteration and the reference bin of the third one, while the latter was set to be at the same absolute value of the balance, by shifting the whole third result by a constant.

A fourth and last iteration is done likewise, where the statistical errors start to become significant.

In summary the systematic errors for the iterations were 0.52%, 0.83%, 1.08% and 2.28%. In figure 5.24 these were added in quadrature to the statistical errors of the single bins, to result in the total error for each JES measurement of the multi-jet bootstrapping method. As the Monte Carlo sample used was calibrated with a high precision, the nominal JES lies at 0. All bootstrap measurements of the JES are in very good agreement with that scale, and the total errors are generally around 1%, up to a probed p_T scale of 1.5 TeV. As the absolute JES in the reference region is assumed to be 3%, it is clear that this is the largest contribution to the total uncertainty of the absolute JES. Compared to this the errors introduced by multi-jet bootstrapping the calibration from 600 up to 1500 GeV are close to being negligible. Even for the region of the highest probed p_T , reaching up to 2.3 TeV, the method's error is still manageable at 3.5%, which increases the absolute JES uncertainty from 3% to 4.5%.

It can be concluded that for this sample the proposed bootstrapping of the jet energy scale, using an iterative method and multi-jet topologies, appears to be a very useful tool to extend the p_T region where the JES has been verified in-situ, while itself only adding marginally to the errors and uncertainties. The JES can

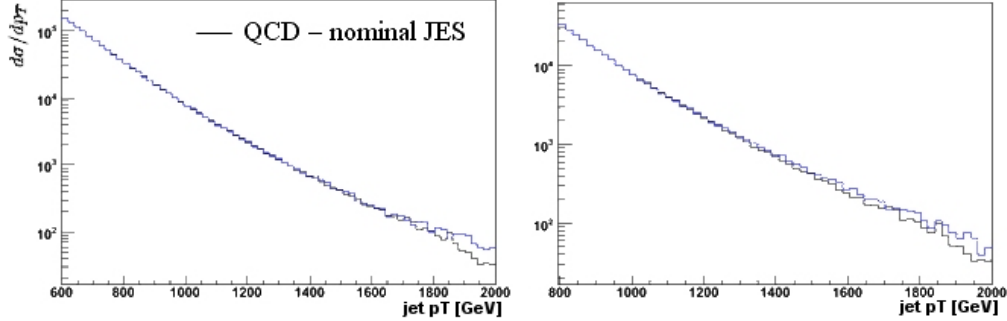


Figure 5.25: Correctly calibrated QCD sample compared with a spectrum including a 5% JES error (left) and a quark compositeness scenario (right)

essentially be bootstrapped from 600 GeV to 1.5 TeV without significant losses in accuracy, and, assuming a 3% JES uncertainty in the reference region, the absolute JES around 2 TeV can still be probed with a total error of less than 5%.

JES nonlinearities

Multi-jet bootstrapping has been established above as a viable procedure to verify a correct JES. The next step is to study its results in case the JES is not correct and non-linear. This case is especially important as deviations from the nominal JES at high values of p_T can easily hide or fake signals from physics beyond the standard model. As an example a possible nonlinearity of the JES due to the non-compensating nature of the calorimeters was parameterized by:

$$\frac{p_T^{miscalibrated}}{p_T^{nominal}} = \frac{1}{c \cdot (1 + (\frac{e}{h} - 1) \cdot b \cdot \ln(p_T))} \quad (5.6)$$

whereas $\frac{e}{h}$ is 1.36, c was set such that the JES is correct at 1 TeV, and the parameter b was chosen such that it is off by 5% at 2 TeV.

For illustration, the expected deviations of one example quark compositeness scenario from the inclusive pure QCD jet cross section together with the deviation of one QCD sample including a nonlinearity of the above described magnitude are in figure 5.25. The effect achieved by the parametrization of a possible JES nonlinearity is roughly equal in size and shape to the quark compositeness case with a $\Lambda_{qq} = 10$ TeV.

To measure the JES error, the same event selection criteria and parameters as in the last section are used. Figure 5.26 shows the result. The function used to create the nonlinearity is shown as a solid line together with the measurement. All systematic and statistical errors are included, except for the JES uncertainty in the initial reference region, as for the discovery of JES nonlinearities the absolute JES is not required. The measurement reproduces the introduced error nicely. This

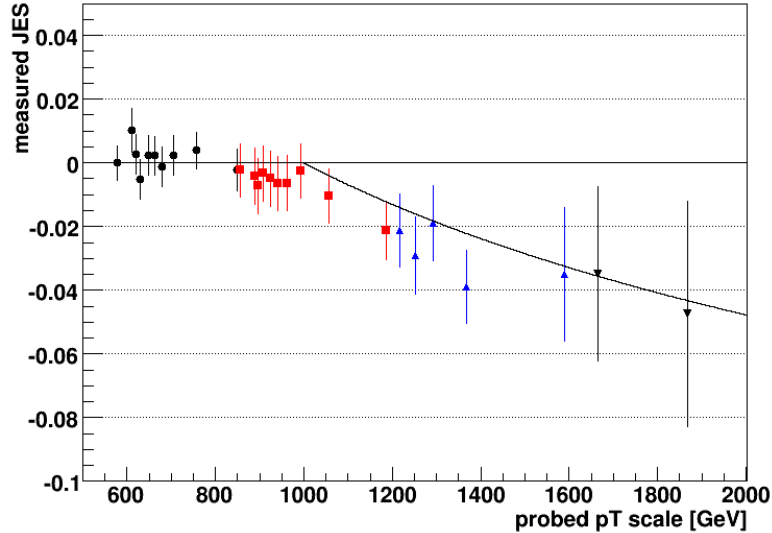


Figure 5.26: Bootstrap measurement of a JES with an arbitrarily introduced non-linearity (solid line)

essentially means that even if the absolute JES uncertainty would be 5% or 10% in the reference region, the JES can be linearized up to 1.5 TeV with a precision of 1%, and with about 2% up to 2 TeV.

In the ideal case the next step after measuring the JES nonlinearity would be to find its reason and correct for it in the standard calibration procedures, though as a quick solution one can also directly extract correction factors from the bootstrap JES measurement and apply them on reconstructed jet level.

Expected Results for Higher Accumulated Statistics

The last section showed that, with sufficient QCD-jet statistics, the errors introduced by multi-step bootstrapping are small compared to the JES uncertainty of the reference region. Therefore the planned strategy for larger ATLAS data samples is not to start bootstrapping at the upper edge of the p_T region calibrated using other in-situ methods, but instead to e.g. always start around 500 GeV and profit from smaller JES uncertainties in the reference region that are achievable with higher statistics.

One issue with predicting the expected reach of a multi-jet bootstrapping calibration utilizing a higher integrated luminosity is the scarcity of fully simulated Monte Carlo events. But as it has been shown that for Monte Carlo data the systematics are known, under control and quantified, the use of the fast simulation of the ATLAS detector (ATLFAST) for further studies is valid.

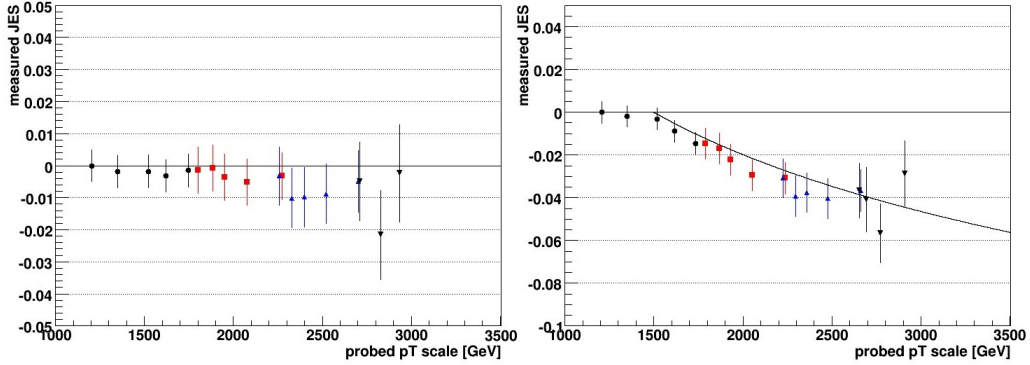


Figure 5.27: Multijet bootstrapping measurement of the JES for an integrated luminosity of 100 fb^{-1} , using a sample with a nominal JES (left), and one with an arbitrary nonlinearity (right)

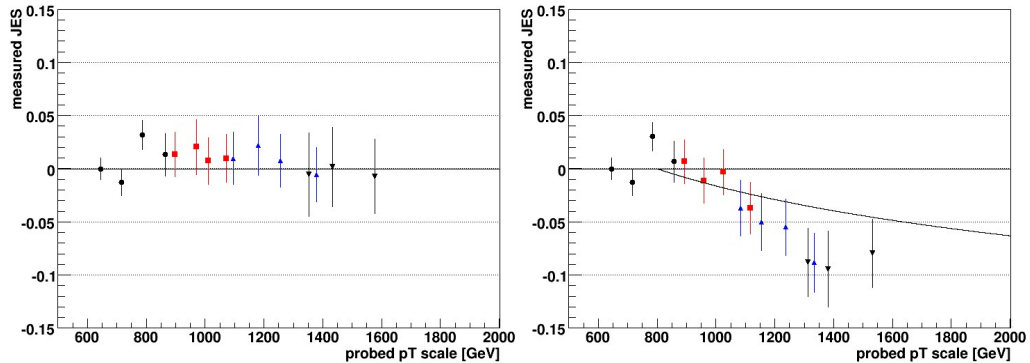


Figure 5.28: Multijet bootstrapping measurement of the JES for an integrated luminosity of 100 pb^{-1} , using a sample with a nominal JES (left), and one with an arbitrary nonlinearity (right)

Hence for the result shown in figure 5.27 500000 events produced using ATLF-FAST and release 13 of the ATLAS Offline Software were used. The first iteration, bringing the JES scale up to 1.1 TeV is not shown on the figure, as it was done using another sample of 5 million events with a lower minimum p_T threshold on generator level.

On the left of figure 5.27 the nominal JES was verified up to 2 TeV with an accuracy $< 1\%$, and with $< 3\%$ up to 3.5 TeV. In the righthand plot the measurement reproduces the JES nonlinearity that was put into the sample with the same accuracies.

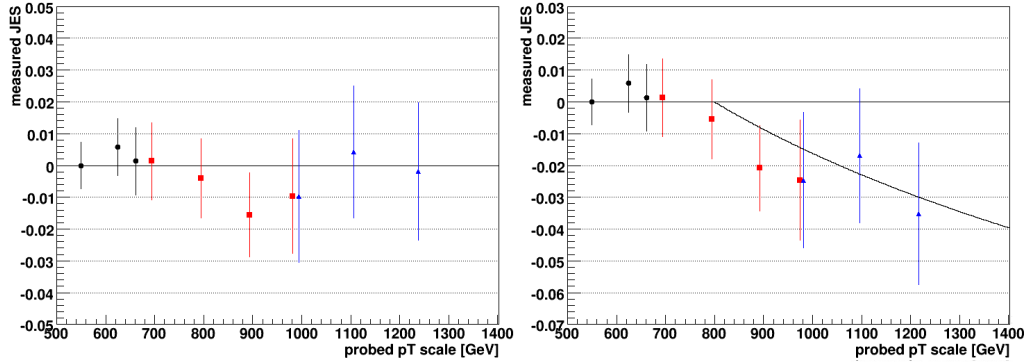


Figure 5.29: Multijet bootstrapping measurement of the JES for an integrated luminosity of 100 pb^{-1} and for a 10 TeV LHC cms energy, using a sample with a nominal JES (left), and one with an arbitrary nonlinearity (right)

Expected Results for First Data

To estimate the reach for early ATLAS data, a random subset of the fully simulated event sample was used, corresponding to 100 pb^{-1} of integrated luminosity. Figure 5.28 includes the results for both a nominal and non-linear JES in the sample.

Expected accuracies of the JES measurement are 3% up to 1 TeV and 5% up to 2 TeV.

10 TeV Data

The current plan is to collect first data with ATLAS at an LHC center of mass energy of 10 TeV instead of 14 TeV. The sample used here was generated using PYTHIA and ATLFast, with a 500 GeV minimum p_T requirement on generator level. The number of events is 22000, which corresponds to 100 pb^{-1} .

Expected accuracies of the JES measurement are shown in figure 5.29 and are roughly 3% up to 1.3 TeV.

5.3 Dijet Bootstrapping

While the intrinsic bias of the p_T -balance using the multi-jet bootstrapping method is understood in Monte Carlo data and corresponding systematic errors were studied and quantified and methods to repeat these studies with real data are available, it would still be beneficial to have a tool available to verify the results and independently establish a JES uncertainty for highly energetic jets in-situ.

Desired ideal characteristics for such a method would be:

- a reach in probed p_T similar to multi-jet bootstrapping

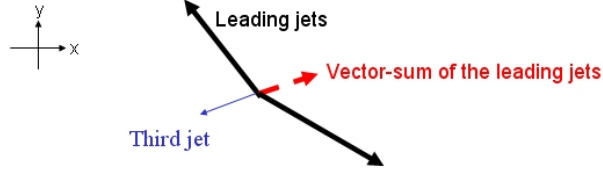


Figure 5.30: Sketch of a possible event topology in the plane perpendicular to the beam axis

- use of a data sample that is orthogonal to the one used for the multi-jet method
- robustness regarding systematic errors and uncertainties, to be feasible as a fast cross check

Regarding the first item, proven in-situ methods will not offer the possibility to verify the JES at the desired scales, which was the initial motivation for multi-jet bootstrapping. The only imaginable way to satisfy this requirement is to utilize the large QCD jet cross section again. Hence another method was developed during the work done for this thesis, which is presented in the following.

To comply to our second requirement to ideally use an independent data sample for the cross check, while QCD jet events are used for both methods, a different event topology is required. Events selected for multi-jet bootstrapping generally have a large p_T difference between the two leading jets, plus a system of additional jets coming from initial and final state gluon radiation. The basic idea for dijet bootstrapping is to use events where the leading jets are roughly of the same momentum scale, and a soft third jet is the only other jet reconstructed in the event. This is illustrated in figure 5.30. A p_T balance is now studied by vectorially summing the momenta of the two leading jets and a comparison of the transverse component of the sum, shown in red, to the p_T of the third jet. If the two leading jets are measured wrongly by a certain percentage, this percentage linearly carries over to the p_T of their sum. As the third jet is on a much lower scale, where the jet response is assumed to be correct, the leading jet miscalibration can be measured. The p_T balance is defined as follows, and ideally resides at zero:

$$p_T \text{ balance} = \frac{\sqrt{(p_x^1 + p_x^2)^2 + (p_y^1 + p_y^2)^2}}{p_T^3} - 1 \quad (5.7)$$

whereas raised numbers 1 to 3 correspond to the jets with the highest, second highest and lowest p_T respectively. The probed p_T scale is defined as:

$$\text{probed } p_T \text{ scale} \sim \frac{p_T^1 + p_T^2}{2} \quad (5.8)$$

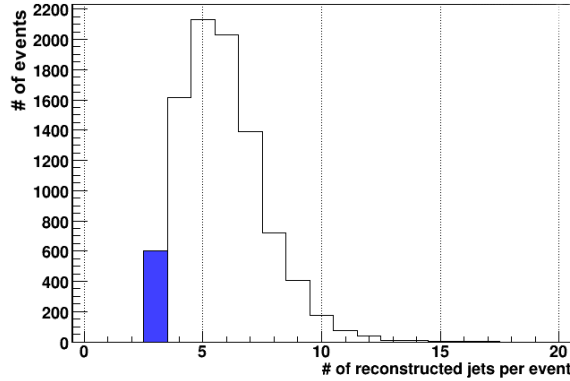


Figure 5.31: Number of jets above the minimum p_T threshold in events selected for multi-jet bootstrapping, exactly 3 jets is shown in blue

The easiest representation of the above situation in data are events with exactly three reconstructed jets with p_T higher than a fixed value, set to reduce the influence of fake jets coming from detector and electronic noise, or additional low p_T jets from the underlying event. Using this as a selection criterium makes the use of a sample orthogonal to the multi-jet bootstrapping sample trivial. While the multi-jet method has been using all events with at least three reconstructed jets so far, tightening this cut to require more than three jets does not influence the systematics and results in only a minor reduction of available statistics, see figure 5.31. Thus to double check the results the multi-jet JES measurement would be redone excluding events with exactly three jets, allowing the result to be compared to an independent measurement using exclusively three jet events and a dijet method.

To comply with our third sought-after characteristic, the method being robust and not requiring extensive systematics studies on its own in order to be able to provide a fast cross check mechanism, ideally the p_T -balance would have a negligible bias. In order to not multiply possible systematic uncertainties and the statistical errors, the method was developed to require no iterative process.

It is clear that not all requirements can be perfectly met, else the question would arise why one should use multi-jet bootstrapping after all, which is more complicated in design and application. A workable cross-check method was still found, but it has one large inherent disadvantage to the multi-jet method, as was hinted at in this chapter's introduction. Namely it appears to be viable to establish a rough JES uncertainty if the JES is linear, but is not suitable to measure JES nonlinearities.

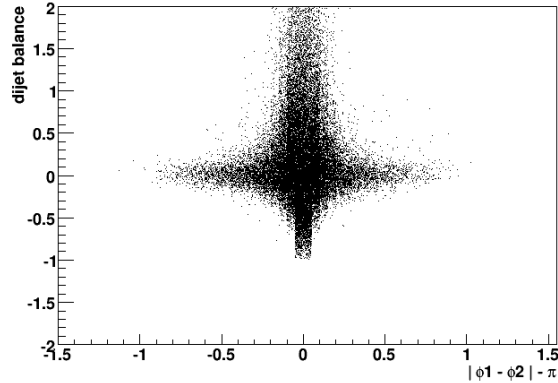


Figure 5.32: Correlation between the dijet bootstrapping balance and the deviation from the two leading jets being directly back-to-back in ϕ

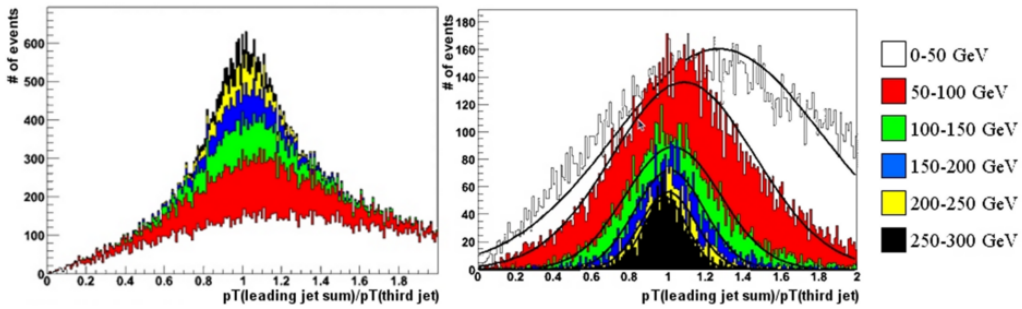


Figure 5.33: Dijet bootstrapping balance for exclusive samples selected on the p_T of the third jet. The histograms are shown super-imposed (left) and in front of each other(right).

5.3.1 Dijet Bootstrapping Applied

Similar to the multi-jet bootstrapping procedure, the p_T range to be probed is first subdivided into a number of intervals. Their borders are defined in a way to establish roughly equal statistics, with all statistical errors lying below 1%. In contrast to the afore mentioned method no iterations are used, so the p_T range is probed with a single application of the method.

Ideally the p_T -balance would reside at 0 for the calibrated Monte Carlo data. If the dijet bootstrapping method is applied without any event selection apart from events having exactly three jets and the third jet being constrained to the reference region, a significant bias is present in the p_T balance. Figure 5.30 on page 96 seems to imply that in the ideal case, the leading jets are not back-to-back in the plane perpendicular to the beam axis, due to the existence of the third jet. In figure 5.32

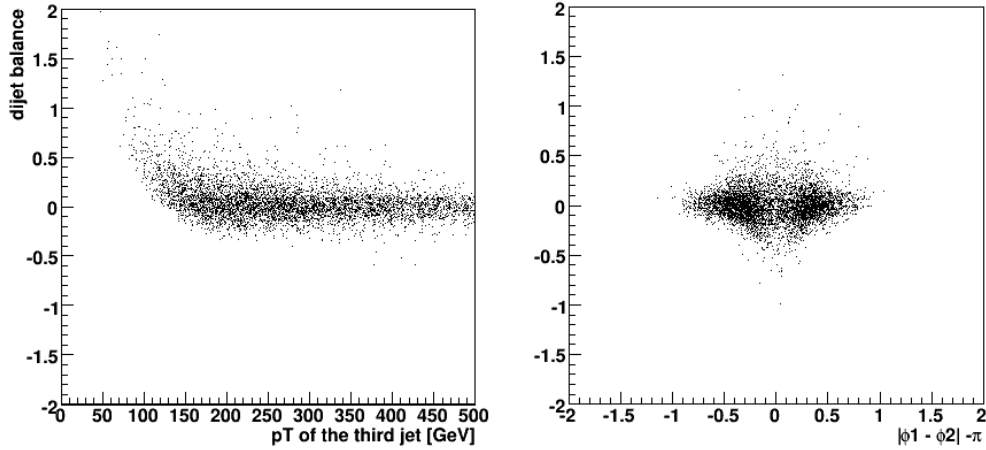


Figure 5.34: Left: Dependence of the balance on the p_T of the third jet after a cut on $\Delta\phi$. Right: Correlation between $\Delta\phi$ and the balance after a cut on the third jet p_T

the correlation between the difference of azimuthal angles of the two leading jets to the dijet bootstrapping balance is shown. Events where the two leading jets are perfectly back-to-back expectedly show a bias and large error of the balance. Another possible quantity to select events on is the p_T of the third jet. On the left of figure 5.33 the contributions of events with differing third jet momenta to a dijet bootstrapping balance plot are shown. On the right these distributions are displayed in front of each other instead of super-imposed. Events with a third jet p_T below 100 GeV are biased with respect to the perfect balance and have a wide distribution due to the higher jet energy scale resolution at lower momenta.

The expectation is that these two event selection criteria have some correlation, as we do expect the leading jets not to be back-to-back in events with a relatively hard, correctly measured, separate third jet. Hence to compare these two options, their efficiency is checked in relation to the respective other method in figure 5.34. After an event selection on the angular difference of the leading jets an asymmetric tail towards lower third jet transverse momenta remains in the data. A direct selection on these only lets events pass which are reasonably balanced, even in cases where their measured leading jets are back-to-back in ϕ . Consequently this criterion was adopted, and an additional selection on the difference in jet angles is not necessary as evident from the figure.

In summary, the following event selections and parameters were used:

- exactly 3 reconstructed jets with more than 30 GeV transverse momentum are required
- the $|\eta|$ of the leading jets is required to be below 1.2

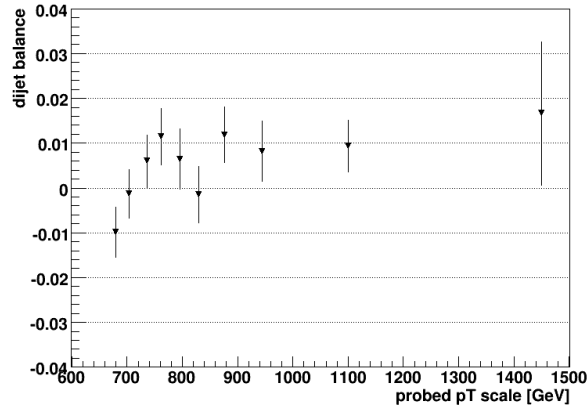


Figure 5.35: Result of the dijet bootstrap method for a sample with a nominal JES

- binning is done on the average of the leading jet and next to leading jet
- the JES is assumed to be calibrated in-situ up to 600 GeV, setting an upper limit for the p_T of the third jet
- a lower limit of 200 GeV is used for the third jet, to reduce the bias of the p_T balance
- the third jet is allowed to have an $|\eta|$ of up to 2.5
- a seeded cone of size $R = 0.7$ is used for jet finding and reconstruction

The result for Monte Carlo data corresponding to about 32 fb^{-1} of integrated luminosity can be seen in figure 5.35. As any bias is simply considered to be a systematic error, the conservative conclusion is that the relative JES uncertainty is below 3% in the probed region. The result can be used as a verification of the multi-jet bootstrapping results, to motivate that systematics are under control.

The reason why it cannot be used as an independent calibration procedure becomes obvious in figure 5.36 on the left. The same nonlinearity as described in section 5.2.4 on page 92 was created in the Monte Carlo data, but does not clearly show in the measurement. The main reason for this is that the transverse momenta of the two leading jets in selected events often lie more than 100 GeV apart. Their distribution for the sample after selection is shown in figure 5.37. Thus what is probed is the average of two scales, and given a JES nonlinearity only one of the two leading jets could be affected, or both to differing degrees, leading to the JES error being “washed out” or appearing to be lower in the dijet bootstrapping measurement.

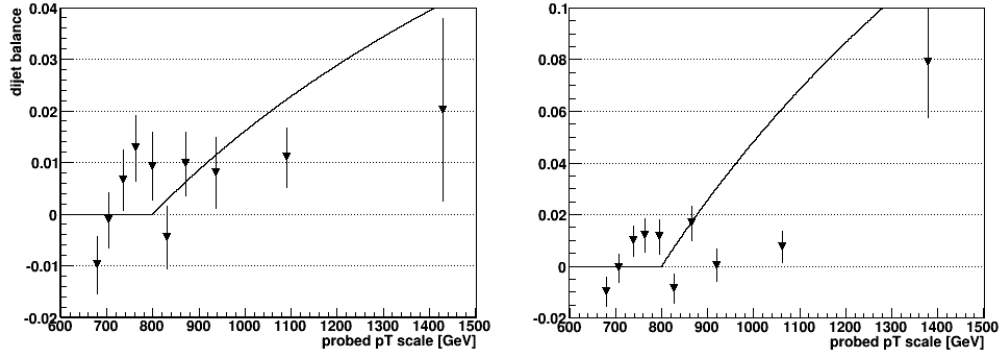


Figure 5.36: Result of the dijet bootstrap method for two samples including an arbitrary JES nonlinearity

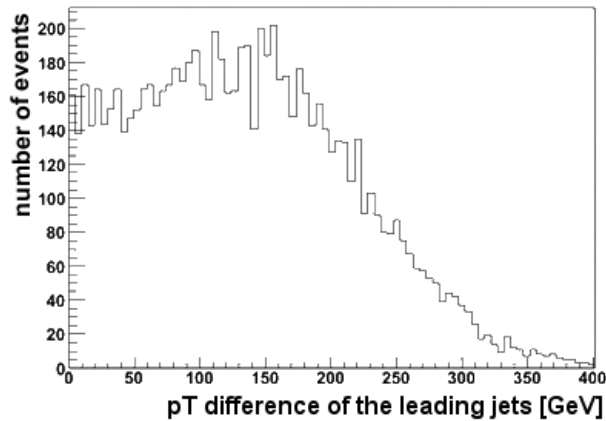


Figure 5.37: Transverse momentum difference between the leading and next to leading jet in events selected for dijet bootstrapping

Thus ideally the JES needs to be linearized first using the multi-jet bootstrapping approach, and only then can the dijet method provide another independent measurement of the residual JES uncertainty. Large residual JES nonlinearities remaining after the multi-jet bootstrapping would be visible in the dijet balance, but some care has to be taken regarding the interpretation. Due to the spectrum of differences in leading jet p_T the resolution for measuring nonlinearities is very low, and any visible deviations must be assumed to be already present at significantly lower scales. This is e.g. evident in the right plot of figure 5.36, where a large JES error was put into the data.

Multi-jet bootstrapping requires a good understanding and estimate of sys-

tematic errors to allow the use of an iterative approach. The dijet bootstrapping method proposed above can be applied to cross check the results, and independently estimate the absolute JES uncertainty. Due to limitations of the dijet method, the results are only meaningful if the measured JES for lower jet p_T is compatible with a constant, and can only be applied to scales lower than the measured one. Localized nonlinearities, in contrast to the JES continuously drifting away from the nominal scale, are not measurable by this method.

5.4 Summary

This chapter has introduced a method using QCD jet events to bootstrap the JES uncertainty acquired by other in-situ methods up to much higher scales, without a significant loss of accuracy. In addition this method, multi-jet bootstrapping, is well suited to linearize the JES at high momentum scales with a very good precision, being able to accurately measure a possible p_T dependence of the JES or even local deviations.

Expected precisions for the local measurements of the JES linearity, as a function of the integrated luminosity of available ATLAS data, are summarized in the following table:

up to [TeV]	1	1.5	2	2.3	3.5
100 pb ⁻¹	3 %	5 %			-
32 fb ⁻¹	1 %		3.5 %		-
100 fb ⁻¹	1 %			3 %	

Including an estimate of JES uncertainties of 5%, 3% and 1.5% in the reference region for the three integrated luminosities the final uncertainty on the absolute JES results would be expected to be:

up to [TeV]	1	1.5	2	2.3	3.5
100 pb ⁻¹	5.8 %	7.1 %			-
32 fb ⁻¹	3.2 %		4.6 %		-
100 fb ⁻¹	1.8 %			3.4 %	

In conclusion all studies performed with simulated Monte Carlo data suggest that multi-jet bootstrapping is a very powerful tool to in-situ measure, linearize and possibly correct the JES at ATLAS. Starting with the first data taken, the relative JES can be precisely measured up to transverse momentum scales above 1 TeV, and the uncertainty on the absolute JES obtained by other methods can be bootstrapped to significantly higher jet p_T .

A second method was developed in order to double-check the results once first data is available. While being limited in its explanatory power, it can provide

further evidence whether the systematics of multi-jet bootstrapping are under control. It does not replace a thorough study of systematics though, and the power of multi-jet bootstrapping will have to be reevaluated with experimental data. Based on the Monte Carlo results presented, the prospects are very promising, though.

Chapter 6

Jets and Physics Beyond the Standard Model - Compositeness

In chapter 4 basic jet physics and related issues and effects have been introduced, and it was established that the jet calibration plays a vital role in ATLAS. The previous chapter proposed new in-situ methods to verify the Jet Energy Scale (JES) once experimental data is available, especially addressing the issue that nonlinearities of the JES can easily hide or feign the existence of new physics beyond the Standard Model. This chapter finally presents searches for new physics signals by inclusive jet studies at ATLAS.

In order to probe the validity of perturbative QCD at the energy scales provided by the LHC, it is not only of interest to study expected data distributions with the null hypothesis that no new physics processes are present. Hence two scenarios beyond the Standard Model are investigated in this thesis, one being quarks as composite and non-pointlike objects, the other being the possibility to observe quantum gravitational effects at the LHC. Both these scenarios were introduced in chapter 2, where the underlying concepts can be found.

This chapter starts with the topic of statistical methods. Then detailed analysis strategies are given for the compositeness case, with an emphasis on robust measurements for early data taking. In the next chapter possible quantum gravitational signatures are included using the same analysis approach, and also compared to quark compositeness.

As a basis inclusive jet measurements at ATLAS are explored, with the focus on a precise test of the validity of QCD and the Standard Model of Particle Physics. The studies presented concentrate on inclusive jet spectra first, where the challenge is not only the problem of instrumental effects, but also to distinguish new physics from Standard Model corrections that are not known exactly. Jet angular

distributions are expected to be less sensitive to these effects and corrections, and are examined afterwards. As this expectation will be confirmed by the results, one analysis using jet angular distributions will be studied in more detail, with respect to a strategy for experimental data.

After expected exclusion limits have been established, the focus is moved on to the discovery reach of ATLAS for quark compositeness.

All estimates of the reach of ATLAS, derived from Monte Carlo data and including all expected statistical and systematic errors, suggest that even results from the first ATLAS data ($\leq 100\text{pb}^{-1}$) are expected to surpass Tevatron results by a factor of two to three.

6.1 Statistics Introduction

In order to discover new physics or to set limits on parameters of specific models, it is useful to compare the experimental data with at least two hypotheses. These are the null hypothesis describing known physics only, and a minimum of one specific model of new physics. In the following the effective models for new physics include at least one free parameter, motivating the test of data against not just the above two but different hypotheses depending on these model parameters. In order to provide exclusion limits for any given dataset, the number of hypotheses is increased toward the limit of a continuum of hypotheses in the work presented here, in essence treating each model and parameter set as distinct hypothesis.

6.1.1 Confidence Levels

A common convention in particle physics is to define different desired levels of confidence for exclusion of new physics compared to their discovery. The reasoning for strict limits on discovery are that the Standard Model is already well established, and thus to claim that it is wrong requires a very high confidence in the experimental results. In other words, extraordinary claims require extraordinary evidence. Although this discussion is independent of the statistic used, so called p-values are considered first. The p-value is defined as the probability to obtain an experimental result at least as extreme as the one that was measured, given that the hypothesis is true. The common convention is that a p-value should correspond to an upper tail of 5σ for a discovery. Expressed in probabilities this roughly equals a $3 \cdot 10^{-7}$ chance that the data is a result of the rejected hypothesis.

As a criticism of this practice, the probability value of $3 \cdot 10^{-7}$ is extremely small and in the far tail of the error distribution. E.g. systematic errors are often assumed to be Gaussian despite that normally only being a rough approximation, especially in the tails. The question is thus if a 5σ p-value is actually meaningful, as it is determined in a region where we know our assumptions are probably wrong.

Therefore p-values of 3σ are used as a measure for a first discovery throughout this thesis, corresponding to a probability of 1.5×10^{-3} . Conservatively this is often called an evidence, and upon an evidence of new physics the first goal can be seen as trying to prove it wrong. Thus all systematic uncertainties would need to be thoroughly reexamined in an attempt to explain the measurement. The goal in this thesis is hence to provide these evidence limits, evaluated with Monte Carlo datasets. In case of an actual evidence for new physics in experimental data, a thorough evaluation of the actual uncertainties in the data and theory uncertainties should lead to one of three scenarios. Either rejection of the hypothesis, a 5σ discovery or a situation requiring more data or a refinement of theoretical models to decide. Furthermore a discovery can at first only be claimed to be a general discovery of new physics, instead of that of a single model. To actually discover e.g. quark compositeness any alternative models leading to a similar experimental signature need to be excluded first.

Concerning the exclusion of hypotheses corresponding to new physics or limits on a parameter of a given model, the convention concerning confidence levels is not as strict, and is adopted here. To exclude a model or parameter of new physics a probability lower than 5% that the measurement or a more extreme value could be a result of the rejected hypothesis is seen as sufficient. The reasoning is that compared to a rejection of the Standard Model, a rejection of one specific hypothetical case of new physics is not surprising. Likewise an exclusion limit that is slightly too large is not seen as critical. Or, quoting Glen Cowan¹: “If you have lost your car keys and have looked hard in the kitchen, so you are 95% certain they are not there, it is sensible to continue the search elsewhere.”

Thus, using 5%, a large number of hypothesis and parameters that would not be excluded by a more stringent requirement, despite the measurement probably being a product of statistical fluctuations, are dismissed in order to concentrate the discussion and further searches on other models or parameter ranges.

P-Values

As already mentioned above, one method for hypothesis testing used in this dissertation are p-values. The basic concept is to determine a probability distribution function for the probability to measure a given value under the assumption that the hypothesis under investigation is true. The p-value is then the probability that the actually measured or an even more extreme value is a result of the hypothesis, assuming it is true.

While being widely accepted, criticism of the p-value method exists, though largely on its interpretation. For example statements are often given that of all experiments quoting p-values below 5% to exclude an hypothesis, many more than 5% are wrong in the sense that the hypothesis was true. Actually this is not a

¹Physicist/Statistician, Royal Holloway, University of London

conflict, as the p-value does not give the probability that the hypothesis is true. Such a probability can not be given in frequentist statistics, as it depends on other factors. This is obvious if e.g. a large number of experiments is considered that use the same constant. This constant is known by a central value and its error, while its unknown true value may lie outside of a 95% confidence level of the central value. All experiments that are very sensitive to this constant are biased, and it is imaginable that the majority of this experiments excludes the null hypothesis as a result of this bias. This emphasizes that the frequentist probability does not give an estimate if a hypothesis is true or not.

To be able to quote the probability that one hypothesis is true, one has to use a Bayesian approach.

Bayesian Approach

The alternative approach also used in the following is based on Bayes' Theorem, which establishes a connection between conditional and marginal probabilities. Interpreted in terms of likelihood and probabilities for data analysis, and neglecting the normalisation for now, it can be written as:

$$P(H|d) \propto L(d|H)P(H) \quad (6.1)$$

where H is a single hypothesis with a fixed set of model parameters, and d is the data. Hence the probability that the hypothesis is true given the data is proportional to the likelihood of the data if the hypothesis would be true, multiplied by the so called prior probability for the hypothesis. The prior parametrizes the available information regarding H before doing the experiment.

The likelihood $L(d|H)$ is the probability that the measured value is a result of the hypothesis. A simple example is considered where a single measurement can have a number i of outcomes. N_i denotes the number of measured events with outcome i , P_i is the prediction of the probability for a single measurement to result in i :

$$L(d|H) \propto \prod_i P_i^{N_i} \quad (6.2)$$

For the determination of exclusion or discovery limits, equation 6.1 is best written with an x denoting one of a set of hypothesis, that differ by a parameter x , or a functional x of model parameters:

$$P(x|d) \propto L(d|x)P(x) \quad (6.3)$$

One can now e.g. integrate to define an upper limit x_{lim} on x with the confidence level C.L.:

$$C.L. = c \int_0^{x_{lim}} L(d|x)P(x)dx \quad (6.4)$$

where c is a constant to normalize the integral over all possible values of x .

Thus the Bayesian approach provides a probability that a certain hypothesis is true, or that a parameter lies inside an interval. But in Bayesian statistics a probability is defined as a degree of belief given the evidence, instead of the classical interpretation of a relative frequency of occurrence in the limit of an unlimited repetition of the experiment.

One problem of the Bayesian method is the dependence on the prior probabilities $P(x)$ assigned to the hypotheses. They express the a priori degree of belief, or expectations from previous experiments, and do influence the results. Given enough data, the data will generally outweigh a sensible prior, but one still has to check the dependence of results on the choice of prior.

One further common critique on Bayesian techniques also concerns the use of the prior. In classical statistics the integration over a likelihood function is not possible. While the ratios of likelihood values are independent of the choice of x , integrals of normalized likelihood functions are not. Thus if one calculates a likelihood function in x or $1/x$, an integral over x or $1/x$ used for Bayesian limits can give different results.

In Bayesian analyses a uniform or flat prior (in some variable) is often chosen, in order to keep the influence of the prior on the result small, or to correctly express genuine ignorance of a parameter value before doing the experiment. So in summary, integrating over likelihoods is wrong to do, but if the likelihood is e.g. multiplied by 1 integration is suddenly valid? This is a common and basically correct critique, emphasizing the care one has to take to ensure that results of a Bayesian method are not strongly biased by either the choice of integrating variable or prior. As in practice this can be impossible to do precisely, one should assign an additional systematic uncertainty to the results.

6.1.2 Summary

The two hypothesis testing methods shortly portrayed represent two different schools of thought, and there is no unanimously accepted decision which one is better suited in general. That being said for specific problems one of the two methods can have definite advantages, while correctly applied Bayesian techniques and a p-value based analyses will often be comparable and in agreement. Both methods are employed and compared in this chapter, with an emphasis on ease of use and *robustness*.

As a closing comment on hypothesis testing in general, none of the methods can really prove one hypothesis. Not only do all uncertainties and calculations

exclude the possibility of gross mistakes or wrong error estimates in their application or treatment of the data, more importantly alternate hypotheses derived from completely different models could produce the same experimental signature. This problem is of vital importance in the work presented, as quark compositeness and quantum gravitational signatures are compared, with the conclusion that they can not be distinguished easily using jet data only. Thus any limits on model parameters or discoveries have to be interpreted as results under the assumption that a possible deviation from Standard Model QCD behavior is the result of the hypothesis under investigation.

Outlook

One further consideration regarding confidence levels and statistics is that all analyses presented in the following have at least one free parameter, usually an event selection criterion. That parameter is envisioned to be selected depending on the actual hypothesis under investigation, including its parameters like e.g. the compositeness scale.

The goal of these parameters is to optimize the significance of comparing one single new physics hypothesis with the null hypothesis. The number of Monte Carlo events used herein is significantly higher than the number of events expected to be ever measured by ATLAS, and statistical errors have been scaled down to simulate smaller samples without dropping any events. Hence it is expected that optimizing these analysis parameters with Monte Carlo data is sufficiently insensitive to statistical fluctuations, and the results are a reasonably good and unbiased choice.

These parameters can not be optimized using a sample of experimental data, as doing so can heavily bias the result. It would be equivalent to conducting several hundred experiments and only selecting results where the measured significance due to statistical fluctuations is maximal, negating any validity of p-values, confidence limits and intervals. As a result the general strategy for ATLAS data is to optimize the analysis using a high statistics Monte Carlo sample and up to date experimental and theoretical uncertainties, and then apply the analysis unchanged to the actual data.

6.2 Quark Compositeness

While comparing jet measurements to simulated QCD data can provide very valuable information regarding parameters of the theory, one big question at ATLAS will be if the Standard Model and perturbative QCD are in agreement to the data at all.

One possible signal for comparison with pure QCD in inclusive jet spectra is the model of quark compositeness, using an effective theory expressed as a contact interaction, as introduced in chapter 2.

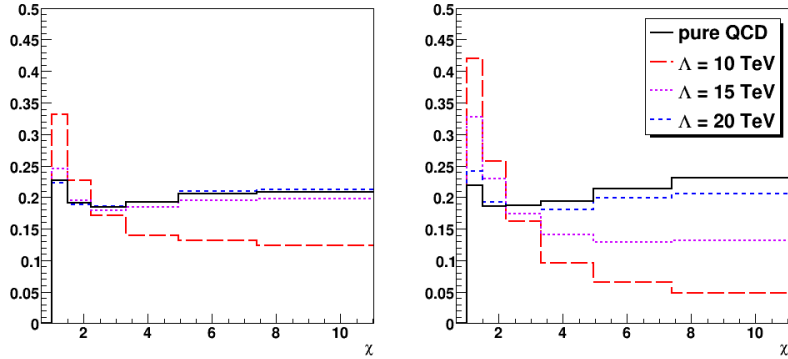


Figure 6.1: Expected distributions of $\chi = e^{|\eta_1 - \eta_2|}$, with an event selection on M_{jj} greater than 3 TeV on the left and 6 TeV on the right

The influence of a possible quark substructure is approximated by adding an effective term to the Lagrangian of quark-quark scattering. In the following the left-left isoscalar model with destructive interference is used. This is a common convention for the comparison of limits derived by the quark-quark coupling. The effective Lagrangian is:

$$\mathcal{L} = \mathcal{L}_{\text{QCD}} + \mathcal{L}_{\Lambda} \quad \text{with} \quad \mathcal{L}_{\Lambda} = \frac{4\pi}{2\Lambda^2} (\bar{q}_L \gamma^\mu q_L) (\bar{q}_L \gamma_\mu q_L) \quad (6.5)$$

For the calculation of cross sections this leads to an interference term of QCD and the contact interaction, dependent on $\frac{1}{\Lambda^2}$, plus a pure contact interaction term proportional to $\frac{1}{\Lambda^4}$. In addition to a change of the inclusive jet cross section another expectation is a change in jet angular distributions, as e.g. visible in figure 6.1.

6.2.1 Monte Carlo Data

If not explicitly stated otherwise, the following Monte Carlo samples were used for the study of quark compositeness vs. QCD. Event generation was done using the PYTHIA generator, version 6.412. The samples of pure QCD were created with the standard settings for inclusive QCD jet production at the LHC, including underlying event and multiple interactions. Pile-up was not included. The detector simulation was done using the fast ATLAS detector simulation ATLFAST (version 13.0.40 of the ATLAS software), as the required statistics can not be provided using the full detector simulation. 10 million pure QCD events with differing limits on jet p_T on generator level were generated and simulated. Afterwards the generated samples were weighted by their cross sections and merged. The result is a continuous jet sample starting at a jet p_T of 560 GeV.

For the compositeness samples a PYTHIA switch to include anomalous couplings was set. The quark substructure is implemented as the left-left isoscalar model with destructive interference. Only the u and d are assumed to be composite, and compositeness is included for the following processes:

- $q_i q_j \rightarrow q_i q_j$
- $q_i \bar{q}_i \rightarrow q_k \bar{q}_k$

To get a consistent sample of high p_T jets a number of standard processes were added:

- $q_i \bar{q}_i \rightarrow gg$
- $q_i g \rightarrow q_i g$
- $gg \rightarrow q_k \bar{q}_k$
- $gg \rightarrow gg$

24 million events were generated with compositeness scales Λ of 3, 5, 10, 15, 20 and 25 TeV.

Furthermore another 11 million events were produced with a center of mass energy of 10 TeV instead of 14 TeV, to evaluate the potential of early ATLAS data that might be taken with 5 TeV proton beams.

Jets are found and reconstructed starting from $p_T = 10$ GeV and for pseudorapidities $|\eta| \leq 5$, using a seeded cone algorithm with $R = 0.4$.

6.3 Inclusive Jet Spectra

Given the effective Lagrangian, the first obvious choice to search for quark compositeness are inclusive jet spectra. The expected inclusive jet p_T spectrum is displayed as an example in figure 6.2, for pure QCD and compositeness with varying scale parameters Λ .

But a search for quark compositeness to either claim a discovery or estimate exclusion limits on the compositeness scale depends on a comparison between data and theory. Thus in addition to experimental uncertainties there are large theoretical uncertainties on the inclusive jet production cross section at the LHC, introduced in chapter 4. These limit the sensitivity of ATLAS to new physics, as e.g. an excess of events at high jet p_T values could also be attributed to Standard Model corrections that are not known precisely.

Likewise the jet energy scale at ATLAS will never be known exactly, but can only be constrained to lie inside some bounds.

Analyses on inclusive jet cross section spectra are very sensitive to the mentioned

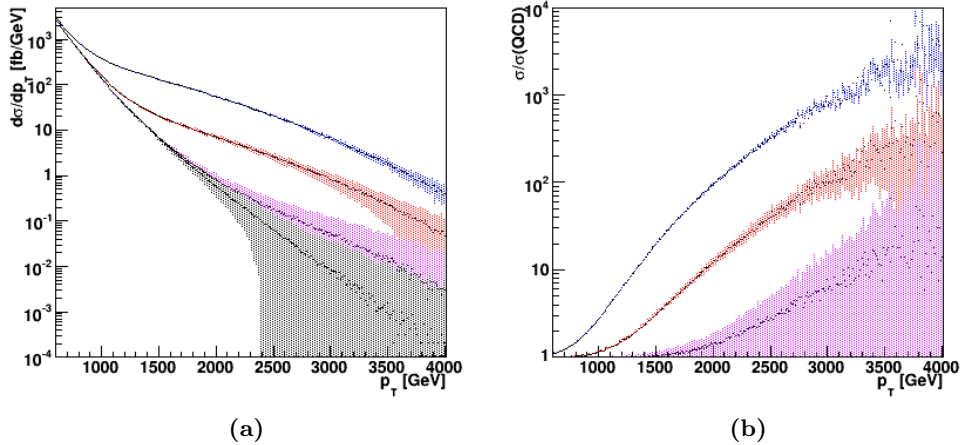


Figure 6.2: Inclusive jet spectra for (from top to bottom) Λ of 3, 5 and 10 TeV and QCD. Shown are (a) the respective cross sections and (b) the cross sections normalized to the QCD expectation. Error bands represent statistical errors with 1 fb^{-1} of data

factors, while the alternative of using jet angular distributions, described in section 6.4, is more robust in that aspect. Jet angular distributions result in higher exclusion limits for the compositeness scale Λ in case the data is QCD only and systematic uncertainties are not negligible. They are studied in more detail in the respective section, and are also used to estimate the discovery potential of ATLAS. Inclusive jet cross-sections nonetheless provide valuable information and act as a cross check. This is especially important in the case of evidence for new physics. Hence analyses on inclusive jet spectra are also covered in the following.

As a start four analysis prototypes are presented. One of these is then generalized to include all relevant systematic uncertainties, with a special focus on the JES. The in-situ calibration chapter of this dissertation already hinted that especially nonlinearities of the JES can severely restrict the reach of ATLAS in the parameter Λ if inclusive jet spectra are used for analysis. This has been one major motivation to develop the multi-jet bootstrapping calibration method which was presented in the previous chapter.

6.3.1 Λ -fit of jet spectra

One challenge in acquiring confidence limits by comparing the data with theory is that only a limited number of simulated samples can be produced, corresponding to distinct parameters of the theory. But the goal is to be able to compare the data with a prediction that is continuous in the parameters of the theory.

For the compositeness case this problem was solved by a fit of the jet spectra

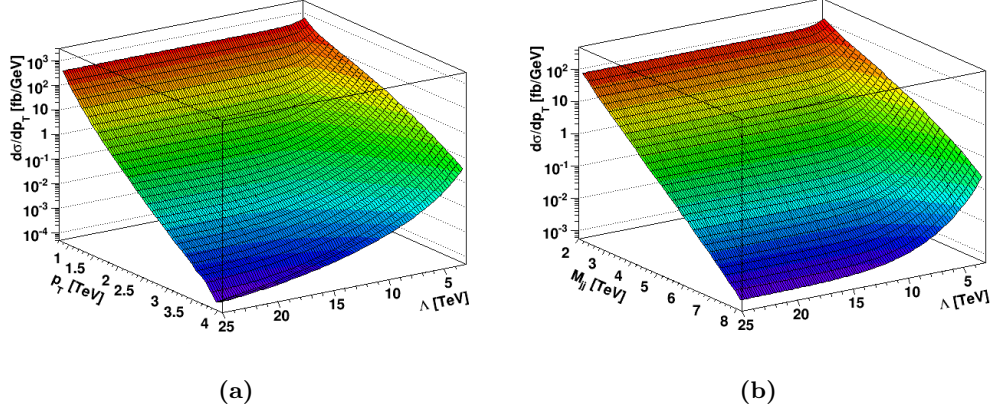


Figure 6.3: The expectation of the inclusive spectra of (a) jet p_T and (b) M_{jj} derived from a fit of the samples with distinct values of Λ

in dependence of the compositeness scale Λ . The spectra of the inclusive jet cross section and dijet invariant mass were divided into intervals of p_T or respectively M_{jj} . For each of these intervals the number of expected events given a certain Λ was fitted with the following function:

$$N(x) = A + B x + C x^2 \quad (6.6)$$

where A , B and C are free parameters and $x = \frac{1}{\Lambda^2}$. The choice of x is motivated by the effective Lagrangian for the production of the compositeness samples, shown in equation 6.5 on page 111. As in a single p_T or M_{jj} interval the contribution from the particle distribution functions can be assumed to be limited due the fixed scale, the Λ dependence of the matrix elements dominates the expected cross section and leads to the above ansatz.

Figure 6.3 presents the fit results for the inclusive jet cross section and M_{jj} . For the distinct simulated values of Λ , the differences between the actual values and the fits are below 1% up to jet p_T (M_{jj}) of 2 TeV (4 TeV) and generally below 3%. The dominant source of these differences is the statistical error of the Monte Carlo samples. The errors of the fit are neglectable in comparison to other experimental and theoretical errors encountered in the analyses.

In conclusion the fit is very efficient in reproducing the simulated samples, additionally providing spectra for any arbitrary value of Λ .

6.3.2 Analysis Prototypes

Two different statistical approaches, p-values and a Bayesian method, were used to construct four analyses and acquire expected exclusion limits. These prototypes use statistical errors plus a simple JES error of 10%, excluding other systematic

uncertainties. The sensitivity of the exclusion limits to this JES error was determined by applying the analyses to samples where the JES has been shifted up and down by a constant 10%.

The only event selection criterion used for the analyses is the requirement that the pseudo-rapidity $|\eta|$ of the two jets with the highest values of p_T is required to be lower than 2.

Bayesian Analyses

The first analysis prototype, based on Bayesian concepts, was done using both the inclusive jet and invariant dijet mass spectra. The normalized p_T (M_{jj}) spectrum is subdivided into intervals with a width of 100 GeV (200 GeV), starting at 1 TeV (2 TeV). The distributions acquired by the Λ -fit are used to calculate the probability P_i for a single event to be measured in the interval i . N_i are numbers of events in the i th interval for the weighted QCD jet sample, treated as experimental data corresponding to a certain integrated luminosity $\int \mathcal{L}$. Hence, the likelihood of the data if the hypothesis H is true can be written as:

$$L(data|H) \propto \prod_i P_i^{N_i} \quad (6.7)$$

This product was cut off at the lowest number i where N_i is below 1. The above can not be determined numerically in the case of very large N_i , due to the limited precision of numerical calculations. Instead the logarithm of the likelihood is used:

$$\ln(L(data|H)) = C + \sum_i N_i \ln P_i \quad (6.8)$$

where C is a normalization constant. The hypothesis H is defined by a parameter depending on the compositeness scale. For several reasons this parameter was chosen as $\frac{1}{\Lambda^2}$ instead of Λ . Firstly, it is helpful to be able to calculate $L(data|H)$ for hypotheses H with Λ up to infinity, as an infinite compositeness scale is identical to pure QCD. As a compositeness case with very high Λ can not be distinguished from pure QCD, the likelihood would, starting from some Λ , be positive and constant up to infinity and thus unintegrable. While a posterior probability distribution $P(\Lambda|data)$ based on such a likelihood can be made integrable by the choice of a suitable prior, choosing $\frac{1}{\Lambda^2}$ as variable is more elegant. Secondly $\frac{1}{\Lambda^2}$ is the parameter actually used in the effective Lagrangian and for the fit of the spectra.

To arrive at values for the posterior probability distribution $P(\frac{1}{\Lambda^2}|data)$ the likelihood is multiplied by a prior $P(\frac{1}{\Lambda^2})$, equivalent to adding a term to $\ln(L)$. This prior was chosen to be constant, and thus does not influence the results.

For each $\ln(L)$ function the highest value is determined and added to the function as a constant, resulting in likelihood values between 0 and 1 after applying

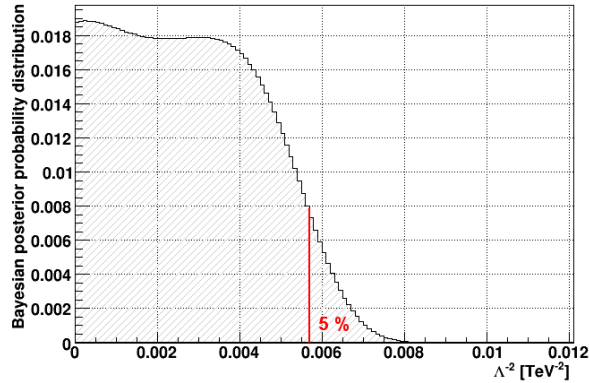


Figure 6.4: An example for a Bayesian posterior probability distribution for $\frac{1}{\Lambda^2}$

$L = e^{\ln L}$. All likelihood functions are lastly normalized to one. Together with the constant prior the Bayesian probability $P(\frac{1}{\Lambda^2}|data)$ of the parameter $\frac{1}{\Lambda^2}$ being true given the data, is thus equivalent to the normalized $L(data|\frac{1}{\Lambda^2})$.

$P(\frac{1}{\Lambda^2}|data)$ is calculated in the described way for different integrated luminosities of the simulated data sample and $0 < \frac{1}{\Lambda^2} < 0.12$ (corresponding to $2.9 < \Lambda < \infty$). Figure 6.4 is an example for a resulting posterior probability distribution.

Using

$$\int_0^{x_{lim}} P(x|data)dx = 95\% \quad x = \frac{1}{\Lambda^2} \quad (6.9)$$

a 95% confidence upper limit for x and thus lower limit for Λ can be acquired.

Exclusion limits using the simulated QCD sample as data are summarized in the following table:

$\int \mathcal{L} \text{ [fb}^{-1}\text{]}$	limit on Λ [TeV]	
	based on M_{jj}	based on p_T
0.1	7.0	10.1
0.3	7.2	11.2
1	7.4	11.7
3	7.5	12.0
10	7.6	12.3
30	7.6	12.5

The limits obtained using an inclusive jet spectrum in p_T are significantly higher than those obtained using the M_{jj} spectrum. Hence the inclusive jet p_T spectrum is used in the following. As a side note, the maxima of the exclusion

limits for each method are essentially the result of a scale Λ where the JES error of the sample is indistinguishable from quark compositeness of that scale.

As an alternative a second prototype analysis was tested, identical to the first one except for the p_T intervals defined. The number of intervals in equation 6.7 on page 115 is now set to two. As the QCD and compositeness spectra are expected to diverge at different points depending on Λ , the border p_T^{cut} to attribute events to one of the resulting p_T intervals is a free parameter during the analysis.

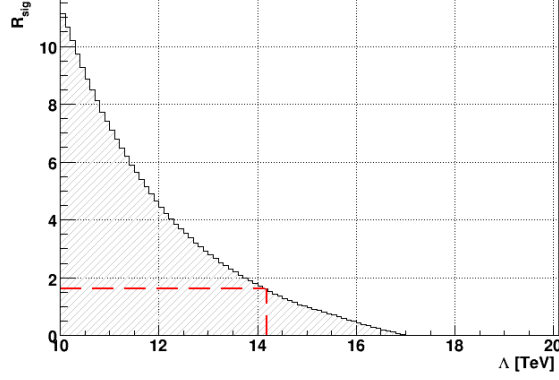
For each integrated luminosity and scale Λ the optimal choice for p_T^{cut} , resulting in the best exclusion limit, is determined and used. The analysis is done using a high statistics Monte Carlo sample with weighted statistical errors as data, thus the optimization is viable as real statistical fluctuations are very small. The p_T^{cut} values acquired from simulations would need to be used for actual data, as the optimization is not valid using experimental data of limited statistics.

Results based on the discrimination of jets whether their p_T is above or below p_T^{cut} , together with the optimal values for p_T^{cut} are:

$\int \mathcal{L} [\text{fb}^{-1}]$	$\Lambda_{limit} [\text{TeV}]$	$p_T^{cut} [\text{TeV}]$
0.1	11.5	2.0
0.3	12.6	2.3
1	13.7	2.6
3	14.6	2.8
10	15.4	3.1
30	16.0	3.1

The obtained exclusion limits are significantly higher than for the last case. Both analyses were investigated with respect to their robustness by using a smaller JES uncertainty and excluding a JES error, leading to the conclusion that the last method is more robust against a miscalibration of the JES than the before described use of a large number of small intervals in p_T , which provides higher limits for a perfectly calibrated sample.

The conclusion is that whereas the method using finer subdivisions of the spectra is more sensitive to quark compositeness if systematic errors are highly constrained, it is also more sensitive to an underestimation of systematics or JES nonlinearities. With the focus on early data the simplified approach appears to be more robust.

Figure 6.5: Significances R_{sig} for 3 fb^{-1}

P-Value and the Ratio

Lastly an analysis prototype using p-values was developed, based on the second Bayesian analysis. A ratio R of the number N of jets below and above p_T^{cut} is defined, including a lower cutoff at 1 TeV:

$$R = \frac{N_{events}(1TeV \leq p_T \leq p_T^{cut})}{N_{events}(p_T > p_T^{cut})} \quad (6.10)$$

The following variable is calculated for a set of integrated luminosities and Λ values between 3 and 25 TeV:

$$R_{sig} = \frac{|R^{QCD} - R^\Lambda|}{\sqrt{\sigma_{QCD}^2 + \sigma_\Lambda^2}} \quad (6.11)$$

Indices of Λ denote the expectation for compositeness acquired with the fits of the spectrum, QCD the Monte Carlo sample with statistical errors being weighted to represent experimental data of a certain integrated luminosity. As no theoretical uncertainties are included in this simple prototype, $\sigma_\Lambda = 0$.

For each integrated luminosity and hypothesis, the p_T^{cut} providing the highest R_{sig} is used.

A result for one sample with an integrated luminosity of 3 fb^{-1} is shown in figure 6.5, using the optimal parameters for each Λ .

Requiring 95% confidence for a lower limit corresponds to a p-value of 0.05, resulting in a requirement of 1.64σ , or $R_{sig} = 1.64$ for a one sided exclusion interval. For a set of integrated luminosities the compositeness hypothesis with the highest Λ meeting this requirement is determined. These exclusion limits, together with the optimal analysis parameters, can be found in the following table:

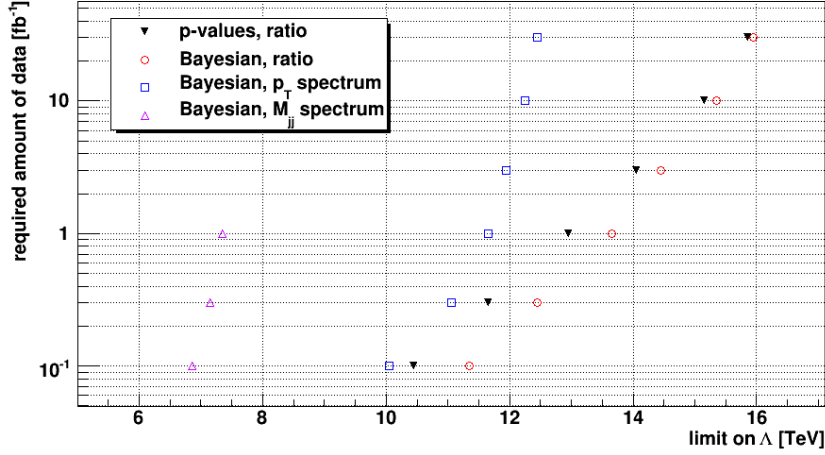


Figure 6.6: 95% exclusion limits on Λ derived with the analysis prototypes, values left of the curves are excluded

$\int \mathcal{L} [\text{fb}^{-1}]$	$\Lambda_{limit} [\text{TeV}]$	$p_T^{cut} [\text{TeV}]$
0.1	10.5	2.0
0.3	11.7	2.3
1	13.0	2.6
3	14.1	2.8
10	15.2	3.1
30	15.9	3.1

The value of p_T^{cut} rises with the limits, which is caused by the QCD and compositeness spectra diverging at higher scales for higher values of Λ . This can e.g. be seen in figure 6.2 on page 113.

The results of all four different approaches are summarized in figure 6.6. The method presented last and its respective Bayesian analysis are comparable in their results. A detailed study of the Bayesian method would have to include uncertainties of the exclusion limits due to the ambiguities in the selection of integrating variable and prior, though. The method of the p-value analysis is unambiguous in that respect. Thus p-values using the ratio of events selected on p_T are the basis for a study including all relevant systematic uncertainties.

Systematic Errors and Uncertainties

Predictions of the inclusive jet production cross section at the LHC currently contain a number of sizable uncertainties. These were introduced in chapter 4, where their detailed influence on the inclusive jet p_T spectrum can be found. In

the following they are shortly revisited with respect to their influence on the ratio R used for the analysis.

Uncertainty of the Luminosity Measurement and Trigger Efficiency To determine a cross section for jet production, a precise knowledge of the acquired integrated luminosity is needed as well as the trigger efficiency to select a QCD jet event.

The trigger efficiency for events containing jets above 1 TeV transverse momentum is considered to be constant and practically 1. The measured luminosity is a factor independent of jet p_T , and furthermore only the ratio of events above and below some jet p_T is used as input into the analysis. Hence both these factors can be neglected.

PDF uncertainties The uncertainty of the expected cross section for inclusive jet production at the LHC resulting from the proton parton distribution functions CTEQ6M1 goes up to a factor of two for the highest jet momenta. This results in uncertainties on R of up to 20%, depending on the p_T^{cut} .

NLO k-Factors The datasets to acquire the expectations of spectra for the different hypotheses were generated at leading order of perturbation theory. To compare them to experimental data they have to be corrected to at least next-to-leading order (NLO) by applying k-factors. The choice of scale for the calculation of these k-factors introduces an uncertainty. The scale dependency of the NLO k-factors was studied in [33] using the program NLOJET++. The result is that the uncertainties of the k-factors are up to 40% for compositeness searches. This introduces an uncertainty of 5% to 10% on the ratio R , depending on the parameter p_T^{cut} .

Comparison with the Full Simulation of ATLAS As the hypotheses were obtained using the fast and simplified simulation of the ATLAS detector, slightly different spectra are expected for experimental data. Using a sample of 470000 fully simulated events the uncertainty arising from this difference was estimated. Depending on the parameter p_T^{cut} an uncertainty of up to 40% results for the ratio.

The R ratios in dependence of p_T^{cut} can be seen in figure 6.7 for both full and fast simulation. This uncertainty is very uneven in p_T , as both full and fast simulation samples have been stitched together from several samples, and actual statistics of the Monte Carlo samples were used, resulting in a changing agreement and changing errors.

As this uncertainty was only determined for pure QCD Monte Carlo data, the assumption has to be made that it can, at least approximately, also be assigned to compositeness data. For the actual optimized p_T^{cut} values it is not the dominant uncertainty, only having a small influence on resulting limits, hence the exact validity of this assumption is not critical.

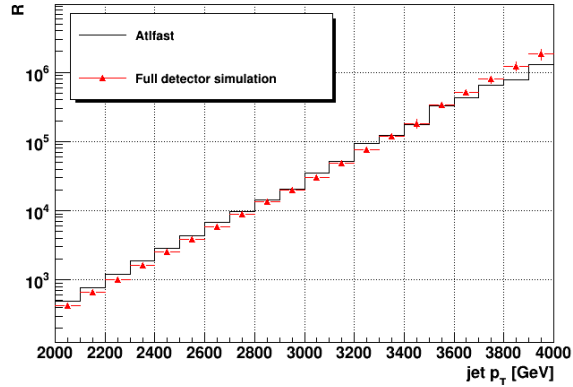


Figure 6.7: Comparison of the ratio R derived from the full and fast simulation of ATLAS

Compositeness Monte Carlo samples using the full detector simulation are starting to become available at the time of writing. Furthermore a new version of the fast detector simulation is in the validation process, and will provide results much closer to the full simulation. This new fast simulation should be ready for use before the start of data taking, hopefully resulting in smaller uncertainties, hence improving the results presented in this thesis.

Electroweak corrections Virtual electroweak corrections, discussed in section 4.1.2, might become important at the LHC. These could result in a change of cross-sections by up to 40%. As this is not fully understood at the moment, this uncertainty is not included in the analysis at first. A rough estimate of its effect will be given later. The onset of these corrections, as the jet transverse momenta become far larger than the W mass, may have been already measured at the Tevatron. Thus with the first LHC data of jets above 500 GeV transverse momentum it should hopefully be possible to study and constrain this uncertainty.

All systematic errors and uncertainties described so far are errors of the expectation and are thus applied to the predictions of the spectrum for the different hypotheses.

Jet Energy Scale Uncertainty As a very simple model, the JES is again scaled up and down by constant values to determine the dependence of the exclusion limits on a 10% JES uncertainty. The influence of JES errors will be examined shortly.

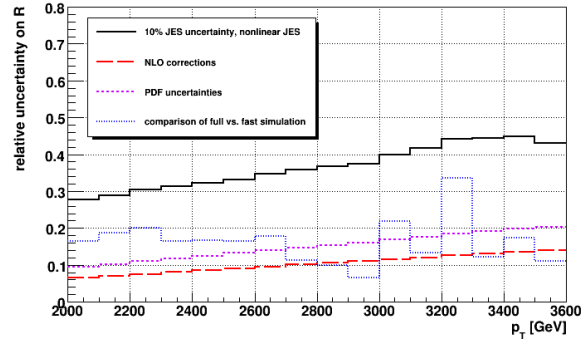


Figure 6.8: Relative uncertainties on R , shown for different sources

6.3.3 Expected Exclusion Limits

Figure 6.8 summarizes the relative influence on the ratio R for the above mentioned systematic errors, including the effect of a JES nonlinearity that will be studied next. Resulting expected exclusion limits for several integrated luminosities can be found in the following table and figure 6.9 on page 124.

$\int \mathcal{L}$ [fb $^{-1}$]	Λ_{limit} [TeV]	p_T^{cut} [TeV]
0.1	10.1	2.1
0.3	11.4	2.4
1	12.5	2.7
3	13.6	2.9
10	14.4	3.0
30	14.8	3.2
100	15.3	3.6
300	15.5	3.6

The limits including systematic uncertainties are up to 1 TeV lower than those determined with the analysis prototype. Furthermore the above table includes results for higher integrated luminosities than for the prototypes. These are not able to significantly increase the exclusion limits though, as systematic errors start to become dominant.

p_T Spectra and Jet Energy Scale Nonlinearities

So far the simple assumption was used that the absolute jet energy scale is unknown, with an uncertainty of 10%, but that it is perfectly constant and independent of jet p_T values. This is hardly a realistic assumption. In the previous chapter, the problems posed by nonlinearities of the JES were quoted as a motivation for the in-situ multi-jet bootstrapping method. One focus of that method

is to linearize the JES with high precision, independent from any uncertainties of the absolute JES.

As an example the analysis was performed on a sample including a JES non-linearity that is in agreement with the uncertainty. The JES was globally set 5% too high and additionally a JES nonlinearity starts at a jet p_T of 2 TeV, steadily bringing the JES up to being 10% off at the highest scales. The results are included in figure 6.9 on page 124.

$\int \mathcal{L} [\text{fb}^{-1}]$	$\Lambda_{limit} [\text{TeV}]$	$p_T^{cut} [\text{TeV}]$
0.1	9.8	2.1
0.3	10.8	2.4
1	11.9	2.7
3	12.8	2.9
10	13.5	3.0
30	13.8	3.2
100	14.2	3.6
300	14.3	3.6

As the JES non-linearity results in a rise of cross-sections similar to that of compositeness the exclusion limits are lower, by 0.3 TeV for low integrated luminosities and up to 1.2 TeV for larger datasets and higher limits. For higher Λ values the hypothesis to be rejected becomes increasingly similar to the JES error.

The results show that for a large JES uncertainty, a simple uncertainty is not fully sufficient to make robust measurements, but also its nonlinearities need to be strongly constrained. If this is not case actual limits derived from experimental data will have a broad spread around the expected limits due to JES errors.

Inclusion of a Possible Uncertainty of Standard Model Electroweak Corrections

Finally a very rough estimate of a possible uncertainty due to Standard Model electroweak corrections modifying jet production cross sections was included, in addition to the JES nonlinearity above. This uncertainty is simply assumed to be of equal size to the uncertainty following from NLO corrections. The result is that all limits are 0.1 TeV lower. Hence it can be concluded that while such corrections can play a vital role for an actual measurement of the jet spectrum, for the ratio used in this analysis an additional uncertainty of this size is not expected to be significant compared to sum of the other systematic uncertainties.

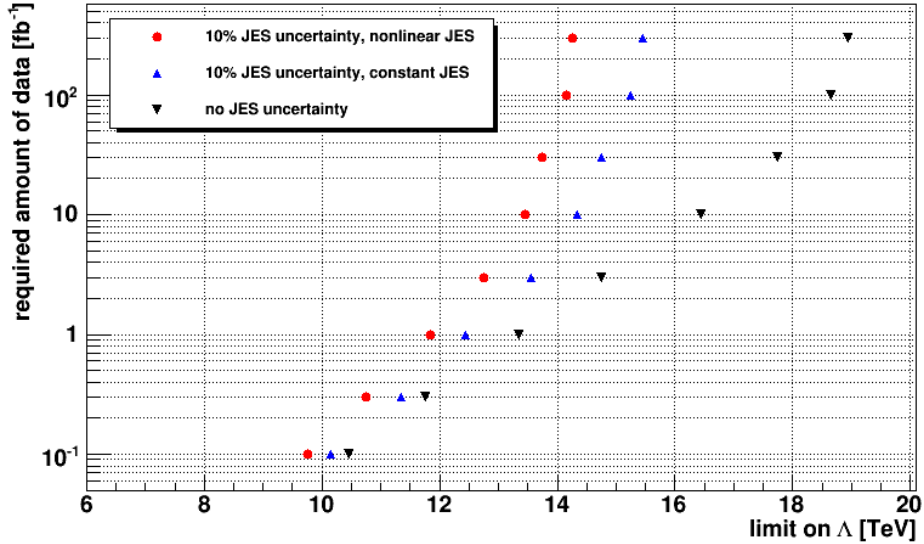


Figure 6.9: Expected 95% exclusion limits using a p-value analysis on a ratio derived from jet p_T spectra

Summary and Conclusion

Figure 6.9 includes three results of the above analysis. One was obtained excluding any JES uncertainty or error, one assuming that the JES is constant but has a global uncertainty of 10%, and one that includes an actual JES non-linearity in the data. It can be concluded that for early data, the analysis method presented is relatively insensitive to constant and global JES errors due to its construction, and the reach of the analysis is limited by statistics and theoretical uncertainties. For hypothesis with higher values of the compositeness scale Λ , the JES uncertainty makes gradually harder to distinguish the hypotheses from QCD, and the JES uncertainty becomes the dominant factor.

Additionally, if there is an actual JES non-linearity present in experimental data, it could fake a compositeness signal. This leads to a number of conclusions. Firstly any increase in the number of measured events can not increase the exclusion limits beyond the Λ that is faked by the JES error. Secondly an actual unexpected JES error that is not covered by the JES uncertainty can easily fake a compositeness signal. Hence any discoveries made using inclusive jet spectra have to be checked very carefully.

As the JES is generally assumed to be constant, another possibility is that a JES non-linearity hides a compositeness signal, leading to exclusion limits that are too high. The non-linearity would have to start exactly at the point where QCD and compositeness spectra diverge. While this is not very probable, it is a valid

worst case scenario and still the exclusion limits obtained from data could be too high due to such an effect.

This is not seen as critical as a faked signal, though, and the best exclusion limits are also expected to be derived from jet angular distributions.

Lastly, for large ATLAS data samples expected to be available in 5 to 10 years, JES errors could be highly suppressed by multi-jet bootstrapping, and theoretical uncertainties much better constrained. This could lead to the actual exclusion limits derived from the above analysis by far surpassing the presented expectations based on our current knowledge.

Cutting all systematic uncertainties in half and assuming a negligible JES uncertainty the expected exclusion limit for 300 fb^{-1} of ATLAS data is 20.4 TeV using the presented method.

6.4 Jet Angular Distributions

In the previous section it was shown that while inclusive jet p_T distributions are a useful probe for quark compositeness, their power is highly dependent on the uncertainty of the JES and the level to which the required Standard Model corrections are known. Thus in the following an alternate approach will be presented based on the analysis of jet angular distributions. Quark compositeness is expected to produce an excess of events with high scattering angles in the center of mass system of an event compared to QCD jet production which is comparatively forward peaked due to the dominant t-channel gluon exchange. While measured angular distributions are not immune to afore mentioned uncertainties, their susceptibility is significantly lower, giving rise to the hope that obtained discovery and exclusion limits are better and more stable, also with respect to incorrect estimates of the uncertainties. This is especially important for early ATLAS data where the JES will not be well constrained.

The most useful feature of jet angular distributions is that for QCD jet production all parameters and spectra determined from experimental data are expected to be independent of the probed dijet mass scale. Thus it is in principle impossible that an excess of events in the angular distributions is caused or hidden by the JES, in contrast to inclusive cross section spectra, where new physics can be feigned or hidden by JES nonlinearities.

The common concepts to measure jet angular distributions in a proton-proton collider experiment were introduced in chapter 4. One fundamental obstacle is that the final jets in a proton-proton collision are indistinguishable and can not be uniquely attributed to one of the incident particles. This results in an ambiguity of a measurement of scattering angles θ^* in the center of mass system. The only θ^* that can be explicitly measured in the laboratory system is 90° .

The first common method is to calculate the ratio R_η of events with leading

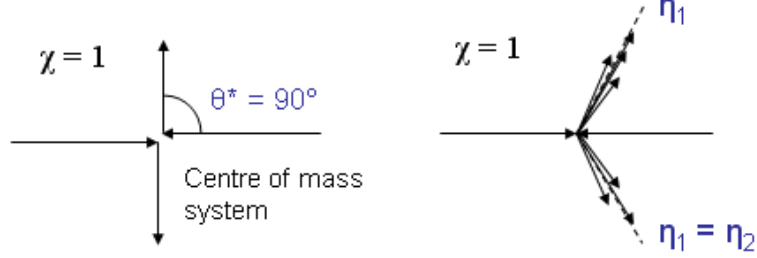


Figure 6.10: Sketch of a dijet event with a $\chi = 1$, on the left in the center of mass system and one possible configuration in the laboratory system on the right

jets in a pseudorapidity range between 0 and 0.5, and those between 0.5 and 1:

$$R_\eta = \frac{N_{events}(0 < |\eta| < 0.5)}{N_{events}(0.5 < |\eta| < 1)} \quad (6.12)$$

After an event selection cut on the invariant dijet mass, the expected QCD value is around 0.6, and any deviation from this value hints at new physics.

A simple implementation of a second method can be done in a way that also results in a ratio of events satisfying certain η requirements. The main difference is that the η difference of the two leading jets is used instead of their absolute η . Secondly, through the definition of the parameter χ , a relation to the scattering angle θ^* in the center of mass system of the two initial state partons can be established:

$$\chi = e^{|\eta_1 - \eta_2|} \quad \text{and} \quad \chi = \frac{1 + |\cos \theta^*|}{1 - |\cos \theta^*|} \quad (6.13)$$

The only unambiguous case, $\chi = 1$, is sketched in figure 6.10 for the center of mass system and one possible configuration in the experimental system. Topologies in the laboratory system can differ due to the boost of the center of mass of the two incident partons in the direction of the beam axis.

The option to do a fit or likelihood comparison of the full χ distribution of events is explored later, for now a ratio R_χ is defined using an arbitrary χ_{cut} :

$$R_\chi = \frac{N_{events}(\chi \leq \chi_{cut})}{N_{events}(\chi > \chi_{cut})} \quad (6.14)$$

This approach is effectively equivalent to the ratio of events above and below a certain η difference of leading jets, with an $\Delta\eta_{cut} = \ln \chi_{cut}$:

$$\Delta\eta = \ln \chi = |\eta_1 - \eta_2| \quad \text{and} \quad R_\chi = \frac{N_{events}(\Delta\eta \leq \Delta\eta_{cut})}{N_{events}(\Delta\eta > \Delta\eta_{cut})} \quad (6.15)$$

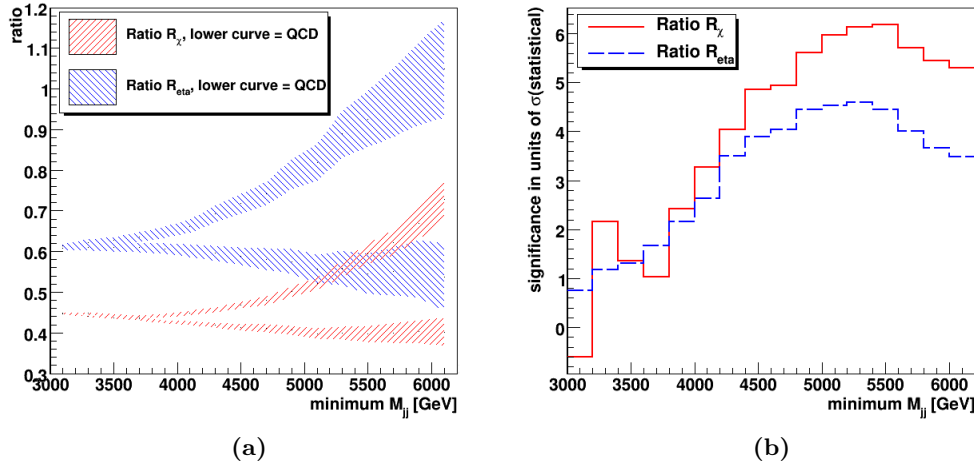


Figure 6.11: Comparison of the ratios R_χ and R_η , (a) their values for $\Lambda = 15$ TeV and pure QCD together with statistical errors for 100 fb^{-1} , (b) the difference of QCD and compositeness expressed in multiples of its statistical error

Comparison of the Two Ratios For both ratios a lower limit on the invariant dijet mass M_{jj} has to be set during event selection, as the data would else be dominated by events with low momentum transfers, where no influence of new physics is expected. Furthermore only by using such a criterion the expectation of QCD behavior, either $R_\eta = 0.6$ or that $\frac{dN}{d\chi}$ is roughly independent of χ , is valid, as seen in section 4.3.4. The position of this limit is an optimization problem as moving it to higher values results in a larger fraction of events exhibiting characteristics of new physics, but also increases statistical and systematic uncertainties. In Monte Carlo data it is thus treated as a free parameter in the analyses.

For inclusive QCD jet production both ratios are believed to be independent of the lower M_{jj} limit, at least on the parton level.

Figure 6.11 (a) contains the expected values of the two ratios together with statistical errors for a sample of 100 fb^{-1} of integrated luminosity, in dependence of the event selection on M_{jj} . Results for compositeness with a scale $\Lambda = 15$ TeV and pure QCD jet production are given. For the χ method the $|\eta|$ of the leading jets is required to be below 2, and the χ distributions were cut off at 10.

Both ratios clearly increase for compositeness when the event selection criterion M_{jj} is increased. The statistical significance, defined by the difference to QCD divided by the statistical error of that difference, is shown in figure 6.11 (b). R_χ exhibits a considerably higher significance.

Additionally the full χ distributions could contain additional information compared to a ratio, and χ is more approachable from theory as it can be calculated

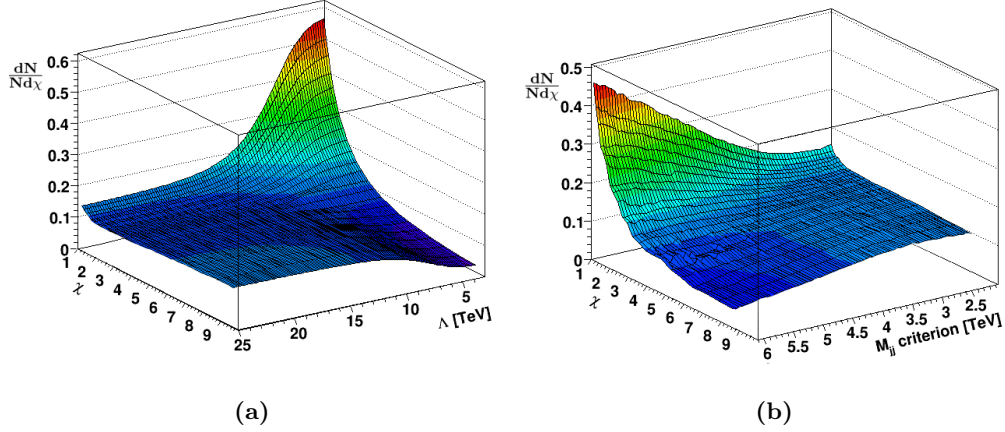


Figure 6.12: Results of the fit of the normalized χ spectra, (a) for a fixed M_{jj} criterion of 4 TeV, (b) for a fixed Λ of 10 TeV

from measured quantities in the laboratory system and the scattering angle in the center of mass system alike. Thus it was decided to utilize χ for jet angular distribution studies.

6.4.1 Fit of the Λ Dependence of χ Spectra

One problem concerning all compositeness analyses is that simulated samples can only be produced for a finite number of discrete compositeness scales Λ , while the goal is to acquire precise exclusion limits on any Λ for any given dataset. The same solution as for the jet cross section spectra was used, namely to perform a fit in Λ .

Using high statistics Monte Carlo samples the χ spectra, additionally depending on the lower limit on M_{jj} , were fitted to result in smooth functions in the parameter Λ . The fit was performed for each individual bin of the angular spectra and a range of M_{jj} criteria, using the following function which is similar to a Fermi Function:

$$f(x) = D + C(1 + e^{A(B - \ln x)})^{-1} \quad (6.16)$$

where A, B, C and D are free parameters and $x = \frac{1}{\Lambda^2}$. This function nicely matches the Monte Carlo results, providing a constant bin content for large compositeness scales, close to pure QCD behavior, a different constant for low compositeness scales and a smooth transition between these two.

The change of the normalized χ spectrum with Λ for one invariant dijet mass limit is shown in figure 6.12 (a). A clear rise towards low values of χ is visible

for low Λ , for higher values the spectrum becomes similar to the expected flat distribution of pure QCD jet production.

Figure 6.12 (b) shows the dependence of the χ spectrum on M_{jj} , with a fixed Λ . At low M_{jj} selection criteria the expected excess at low χ is not clearly visible, while with rising M_{jj} the proportion of events exhibiting compositeness characteristics rises, making the signal much more prevalent. With an actual data sample this results in an optimization problem as a higher M_{jj} criteria lead to lower statistics and thus larger statistical errors, in addition to higher systematic uncertainties.

For the distinct simulated datasets the difference between the fit functions and measured values is below 1% for single bins, and hence negligible in comparison to other errors encountered during analysis.

Using the fit functions a χ spectrum can be obtained for any arbitrary value of Λ .

6.4.2 Comparison of Analysis Prototypes

As in the last section several prototype analyses resulting in expected exclusion limits at ATLAS were done before including all systematic uncertainties. The three alternatives checked are an analysis using p-values and the simple angular ratio defined above, a Bayesian approach also utilizing the ratio, and a Bayesian analysis making use of the χ spectra with full granularity.

P-Value Analysis using the Angular Ratio

This analysis prototype is based on the ratio R_χ defined by equation 6.14. To measure a single value of the ratio R_χ a number of event selection criteria have to be defined:

- A fixed constraint on the leading jets: $|\eta| < 2$
- A selection on the invariant dijet mass M_{jj} that is used as a free parameter, to be optimized depending on available data and the hypothesis
- A limit χ_{cut} , necessary to calculate the ratio, likewise used as a free parameter to optimize significances

As mentioned in the statistical introduction the two free parameters have to be determined using Monte Carlo data, as optimizing them based on experimental data would invalidate the results by being overly sensitive to statistical fluctuations.

The goal of this analysis prototype is to define expected exclusion limits on quark compositeness by comparing a Monte Carlo sample of QCD jet production, treated as the experimental data, with a continuum of compositeness hypotheses depending on the scale Λ .

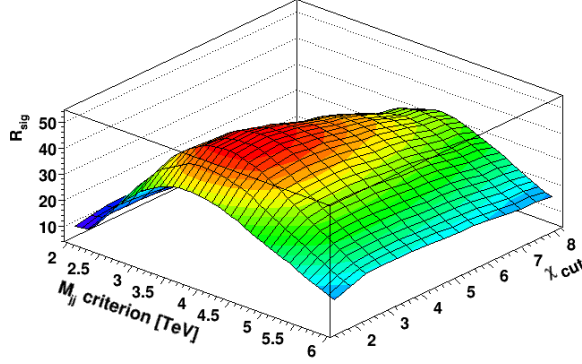


Figure 6.13: Graphical representation of one optimization of χ_{cut} and M_{jj}

Similar to the prototypes for the cross section spectra in the last section, statistical errors for different integrated luminosities plus a JES error of 10% are included. The sensitivity to the JES error was tested by using samples which include an actual error.

For a range of selection parameters M_{jj} from 2 to 6 TeV, χ_{cut} values for the calculation of the ratio between 1.1 and 9, and events up to a χ of 10, the variable R_{sig} is calculated for compositeness hypotheses with Λ between 3 and 25 TeV:

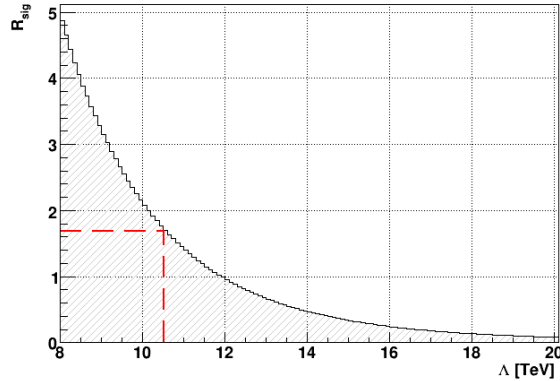
$$R_{sig} = \frac{|R_{\chi}^{QCD} - R_{\Lambda}^{QCD}|}{\sqrt{\sigma_{QCD}^2 + \sigma_{\Lambda}^2}} \quad (6.17)$$

The index QCD denotes the weighted simulated sample used as data, Λ the compositeness hypotheses. As no uncertainties on the predictions of the hypotheses was included, σ_{Λ} is set equal to 0 for now.

For each integrated luminosity and hypothesis, the combination of a χ_{cut} and M_{jj} limit that provides the highest R_{sig} is used. One example plot illustrating this selection is shown in figure 6.13.

Figure 6.14 is the result obtained for an integrated luminosity of 300 pb^{-1} using the optimal parameters for each Λ .

Requiring 95% confidence for an upper exclusion limit corresponds to a p-value of 0.05, resulting in a requirement of $1.64 \sigma = R_{sig}$ for a one sided exclusion interval under the assumption of a Gaussian error. For a set of integrated luminosities the highest Λ of a compositeness hypothesis where this requirement is met was determined. The resulting exclusion limits together with the optimal analysis parameters can found in the following table:

Figure 6.14: Resulting significances R_{sig} for 300 pb^{-1}

$\int \mathcal{L} [\text{fb}^{-1}]$	$\Lambda_{limit} [\text{TeV}]$	χ_{cut}	$M_{jj} [\text{TeV}]$
0.1	9.2	3.0	4.0
0.3	10.5	3.0	4.2
1	12.1	3.0	4.2
3	13.6	3.0	4.2
10	15.4	3.0	4.2
30	17.2	2.5	4.8

Bayesian Analyses

Two prototype analyses were done using the Bayesian approach. The first one only uses two possible outcomes to classify the χ found in a single event, namely if it is above or below some χ_{cut} , being similar to a simple “coin drop experiment”. It is thus very similar to the above described first prototype. Using statistical uncertainties only, their results should agree. This prototype is not described in full detail, as it is a straight-forward simplification of the second Bayesian analysis discussed in the following. The only additional concept required for the use of a ratio is again the inclusion of the free parameter χ_{cut} , to be optimized during analysis.

The second Bayesian prototype utilizes the full available granularity of the χ distributions, sorting events into intervals with borders of $\chi = e^{0.1i}$, for $0 \leq i \leq 23$. This granularity is derived from characteristics of the ATLAS jet reconstruction and calorimeters, and is explained in section 4.3.2.

The determination of a likelihood of the data given the hypotheses is analogous to the analysis prototype using the inclusive jet p_T spectrum in section 6.3.2. In short the likelihood is defined as:

$$L(data|H) \propto \prod_i P_i^{N_i} \quad (6.18)$$

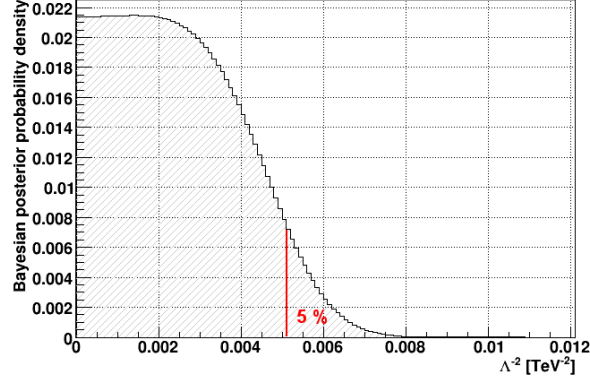


Figure 6.15: An example for a Bayesian posterior probability distribution for $\frac{1}{\Lambda^2}$, limit on $M_{jj} = 4$ TeV

where P_i is the probability for one event to be in the i -th interval, predicted by the hypothesis, and N_i is the number of events in the i -th interval in the simulated QCD data sample. For technical reasons instead of $L(data|\frac{1}{\Lambda^2})$ its logarithm is computed:

$$\ln(L(data|H)) = C + \sum_i N_i \ln P_i \quad (6.19)$$

For each $\ln(L(data|H))$, its highest value is determined and added as a constant, resulting in likelihood values between 0 and 1 after applying $L = e^{\ln L}$. To arrive at values for the posterior probability distribution $P(\frac{1}{\Lambda^2}|data)$ of the parameter $\frac{1}{\Lambda^2}$ the likelihood was multiplied by a constant factor. Lastly the Bayesian probability distributions $P(\frac{1}{\Lambda^2}|data)$ of the hypothesis being true given the data were normalized to an area of one.

The result for an integrated luminosity of 3 fb^{-1} and M_{jj} criterion of 4 TeV is shown in figure 6.15.

Using

$$\int_0^{x_{lim}} P(x|data) dx = 95\% \quad (6.20)$$

with $x = \frac{1}{\Lambda^2}$, a 95% confidence exclusion limit for x and thus also for Λ can be acquired. For each integrated luminosity the M_{jj} selection resulting in the highest limit was used.

The following table contains the Bayesian result using two bins only, together with the optimal parameters:

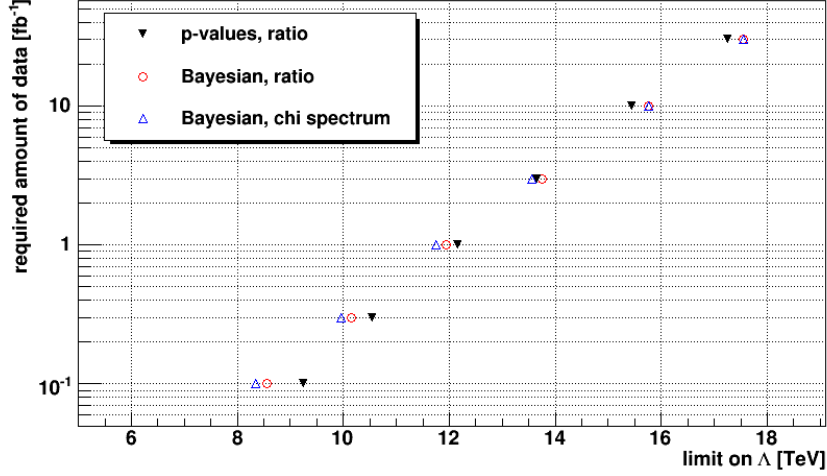


Figure 6.16: 95% exclusion limits on Λ derived with the analysis prototypes, values left of the curves are excluded

$\int \mathcal{L} [\text{fb}^{-1}]$	$\Lambda_{limit} [\text{TeV}]$	χ_{cut}	$M_{jj} [\text{TeV}]$
0.1	8.7	2.7	3.2
0.3	10.2	2.7	3.6
1	12.0	2.7	4
3	13.9	2.7	4.2
10	15.8	2.7	4
30	17.7	2.7	4

The Bayesian comparison of the full spectra results in:

$\int \mathcal{L} [\text{fb}^{-1}]$	$\Lambda_{limit} [\text{TeV}]$	$M_{jj} [\text{TeV}]$
0.1	8.5	3.2
0.3	10.0	3.4
1	11.9	3.8
3	13.6	4
10	15.8	4.4
30	17.7	4.4

Conclusion and Analysis Concept Chosen

The different expected exclusion limits, obtained from simulated Monte Carlo datasets using the above three prototype analyses, are summarized in figure 6.16.

While the number of events in the simulated samples is very high (4 to 10 million per sample) the expected limits, especially for high M_{jj} event selection

parameters, are not fully insensitive to statistical fluctuations. Thus the differences seen in the figure are believed to be mainly of statistical nature.

It is expected that both methods using a simple ratio R_χ perform very similar. But the fact that no additional sensitivity to distinguish the data sample from the hypotheses can be gained using smaller intervals in χ was unexpected at first.

The conclusion is that no additional information is contained in the χ spectra compared to a ratio. This is equivalent to the possibility to parametrize the spectra as a function of χ using only a single parameter. This parameter could be identically obtained by the second Bayesian analysis, in principle comparable to a full fit of the function, or a single observable like the ratio of events left and right of a sensibly chosen χ value.

In chapter 7, where a signal effectively describing the onset of possible quantum gravitational effects is studied, this conclusion is further fortified, as a single χ spectrum contains no distinguishing power between these effects and quark compositeness whatsoever.

The above study has shown that all three analysis prototypes perform very similarly. But for the Bayesian analyses a single function was used as a prior, and a single choice of variable for integration. Other sensible choices exist and result in comparable but not identical limits. Hence for a full analysis an uncertainty would have to be added to the limits due to the ambiguity present in these choices.

As a conclusion the first prototype, based on the ratio R_χ and p-values, was chosen to build the analysis including all systematic uncertainties on, being more robust in this aspect.

6.4.3 Exclusion Limits Using Angular Distributions

After the selection of a general analysis strategy systematic uncertainties need to be addressed. In the following these are shortly introduced and quantified. Afterwards the refined analysis is outlined and described in more detail than given for the prototype, and the procedure to establish exclusion limits with experimental data is discussed.

Systematic Errors and Uncertainties

All systematic uncertainties influencing the inclusive jet p_T spectrum were already listed. But as they influence the ratio R_χ differently, the relevant ones are shortly reexamined in the following.

PDF Uncertainties and NLO k-factors A detailed study of uncertainties of the proton parton distribution functions and the uncertainty of the NLO k-factor due to the choice of the factorization and renormalization scale for jet χ distributions has been done for ATLAS [33]. Generally, depending on the minimum allowed M_{jj} during event selection and χ_{cut} , the uncertainty on R_χ caused by PDF

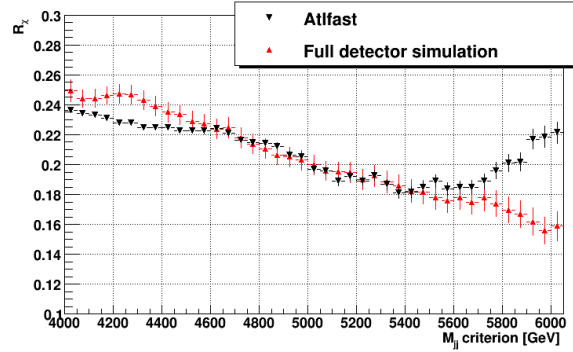


Figure 6.17: Comparison of the ratio R_χ derived from the full and fast simulation of ATLAS, for $\chi_{cut} = 2.7$

uncertainties is between 3% and 14%, while being between 5% and 8% for NLO k-factors.

Accuracy of a Jet η and ϕ Measurement The performance of η and ϕ measurements for jets were studied in section 4.3.2. It is assumed that the full simulation of ATLAS is practically identical to the real detector in that aspect, as the simulation is modeled to describe the detector characteristics as accurately as possible with the available knowledge. This has to be checked in-situ with experimental data, though.

Any residual differences are expected to be negligible with respect to the significant ones arising from the comparison of predictions using the fast simulation of ATLAS to experimental data. These are included in the next uncertainty.

Comparison of the Full and Fast Simulation of ATLAS As the expected ratios for compositeness are based on the simple fast simulation of ATLAS, differences to experimental data are expected. These differences were evaluated comparing Monte Carlo QCD samples that were either using the full or fast simulation of the ATLAS detector. One example is shown in figure 6.17. The difference between these two samples, and the statistical error of that difference, were considered to be the uncertainty of a comparison of compositeness and QCD Monte Carlo generated samples to experimental data.

Depending on the event selection on M_{jj} and the parameter χ_{cut} the uncertainty attributed to the comparison of Monte Carlo data using the fast detector simulation to experimental data is found to be between 10% and 20%. This is the dominant uncertainty for this analysis, as can be seen in figure 6.18 on page 136. As it currently can only be acquired using simulated QCD data, the assumption has to be made that this effect at least has the same order of magnitude for compositeness samples.

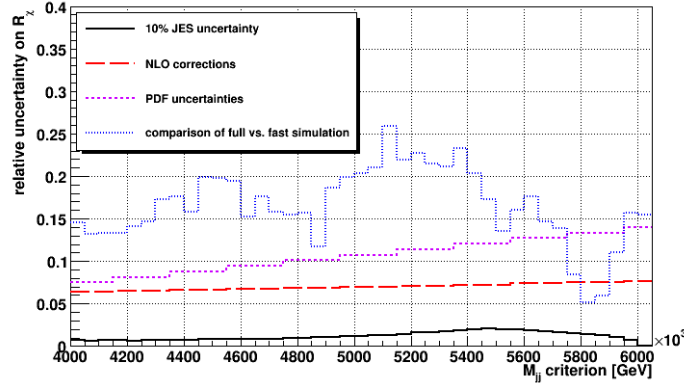


Figure 6.18: Relative uncertainties on R_χ , for different sources; shown is $\chi_{cut} = 10$, the JES effect is an experimental uncertainty and shown for 10 fb^{-1}

As mentioned in section 6.3.2 this estimate will soon be outdated with the arrival of fully simulated compositeness samples and the extended fast simulation of the ATLAS detector hopefully significantly reducing uncertainties.

Electroweak Corrections Possible electroweak corrections to QCD jet production may become important at the LHC, as has already been discussed in the last section. It is again assumed that an effect is of similar size to the uncertainty introduced by NLO corrections. Exclusion limits for integrated luminosities below 3 fb^{-1} were unchanged by this additional uncertainty. For larger sets of ATLAS data, the expectation is that possibly required electroweak corrections are much better constrained. Hence this systematic uncertainty was not included in the analysis.

Jet Energy Scale In contrast to the analysis based on inclusive jet cross section at ATLAS, no specific worst case scenario of possible JES errors was found. Especially for the null hypothesis R_χ is in principle constant independently of the event selection on M_{jj} . Hence it is impossible to feign a significant rise as expected for compositeness with a JES error or nonlinearity. The obtained exclusion limits were found to be only sensitive to the JES for jets close to the event selection limit. Thus the simple parametrization of a 10% JES uncertainty, assuming an essentially constant but wrong JES, is sufficient. The sensitivity of pure QCD results to the JES is mainly caused by a decrease of statistics for a JES that is too low, in addition to small fluctuations of R_χ . If compositeness is included in the data, the JES does influence R_χ for a range of limits on M_{jj} .

The relative influence of the above systematic uncertainties on a sample R_χ ratio is shown in 6.18.

Analysis Outline and Limit Determination

The following analysis is based on the distribution of the event parameter χ . A ratio R_χ of events with χ below χ_{cut} to those above that limit is used:

$$\chi = e^{|\eta_1 - \eta_2|} \quad R_\chi = \frac{N_{events}(\chi \leq \chi_{cut})}{N_{events}(\chi > \chi_{cut})} \quad (6.21)$$

where η_1 and η_2 are the measured pseudorapidities of the two leading jets in each event. For the analysis using Monte Carlo data only, values of the parameter $\chi_{cut} = e^{(0.1i)}$ with $1 \leq i \leq 22$ are used. The event selection criterion of minimum allowed invariant dijet mass M_{jj} is varied between 2 TeV and 6 TeV in steps of 0.05 TeV.

To obtain exclusion limits on the compositeness scale Λ a Monte Carlo data sample of QCD jet production is compared to compositeness hypotheses with a scale Λ between 3 TeV and 25 TeV, in steps of 0.1 TeV. The expected χ spectra of the hypotheses are derived from the the fit functions introduced in section 6.4.1 on page 128.

To define p-values, measured ratios R_χ are assumed to be approximately spread around the expected value for a given true hypothesis by a Gaussian distribution, its width defined by the statistical and systematic errors. Again, with QCD denoting the QCD sample and Λ the different compositeness hypotheses, a value R_{sig} is determined:

$$R_{sig} = \frac{|R_\chi^\Lambda - R_\chi^{QCD}|}{\sqrt{\sigma_\Lambda^2 + \sigma_{QCD}^2}} \quad (6.22)$$

The statistical errors and the JES uncertainty are included in σ_{QCD} , all other systematic uncertainties are applied to the predictions of the hypotheses and included in σ_Λ .

For example a R_{sig} value of 1 corresponds to the possible result R_χ of a measurement differing from the expectation by one total error σ , under the assumption that the hypothesis is true. A p-value is the probability that a hypothesis results in a measurement of a given R_χ or one that is more extreme. As p-values are commonly defined using a Gaussian, a direct relation between R_{sig} and the p-value follows. The probability that a value R_χ is greater than or equal to the measured R_χ is the p-value for that hypothesis. For the exclusion of a hypothesis a p-value of 0.05 is required, corresponding to a measured R_{sig} of 1.64 or higher, as a one-sided limit is defined.

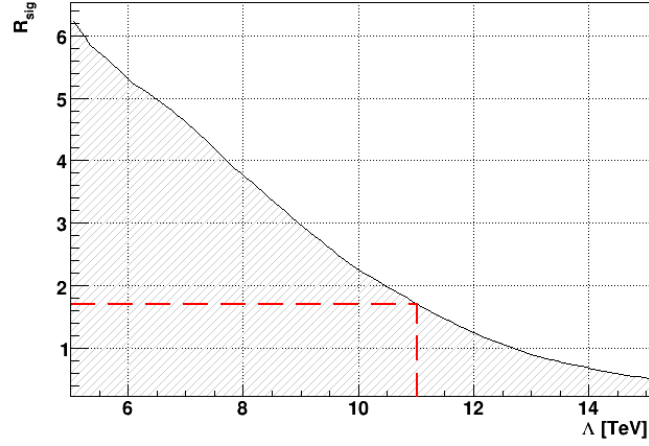


Figure 6.19: Resulting significances R_{sig} for 300 pb^{-1}

Using high statistics Monte Carlo data of QCD jet production, R_{sig} is calculated for all combinations of M_{jj} criterion and χ_{cut} , and for a set of different integrated luminosities.

For each integrated luminosity and Λ , the highest R_{sig} is chosen. The result is the distribution of R_{sig} depending on Λ , e.g. shown in figure 6.19 for 300 pb^{-1} . For each integrated luminosity the highest Λ with $R_{sig} \geq 1.64$ is the 95% confidence exclusion limit on Λ .

The results are summarized in the following table:

$\int \mathcal{L} [\text{fb}^{-1}]$	$\Lambda_{limit} [\text{TeV}]$	χ_{cut}	$M_{jj} [\text{TeV}]$
0.1	9.6	2.46	4.20
0.3	11.0	2.46	4.65
1	12.6	3.00	5.80
3	14.2	4.06	6.00
10	15.6	4.06	6.00
30	16.6	2.72	5.90
100	17.2	2.23	5.90
300	17.5	2.23	5.90

The limits thus obtained are partially higher than for the analysis prototypes, despite the inclusion of the afore mentioned systematic errors. This is firstly explained by the robustness of the analysis with respect to the systematic errors, especially for small data samples where the statistical error dominates. Secondly all parameters in the analysis were allowed to vary in smaller steps, resulting in a higher optimization of parameters.

Generally the obtained limits are higher than for the analysis using the inclusive jet cross section. This is not the case for the smallest data samples, but especially there possible JES nonlinearities could play a large role. Hence the conservative decision is to use the method which is far less sensitive to such effects, especially concerning the possibly feigning of new physics.

The Tevatron limit obtained via inclusive jet production and the same model is 2.7 TeV [8]. The expected exclusion limits for an integrated luminosity of 100 pb⁻¹ at ATLAS, estimated to result from the first few months of data taking, exceed this Tevatron limit on the compositeness scale by a factor of 3.

Assuming a jet energy scale uncertainty of 1.5% and a reduction of theoretical uncertainties by a factor of 2 before acquiring 300 fb⁻¹ of ATLAS data, the final reach of this analysis in Λ is expected to be 20.4 TeV. This is identical to the value derived from the analysis based on inclusive jet p_T spectra, as the performance of the two analyses is very similar if systematic effects are negligible in comparison to statistical errors.

Expected Limits for a 10 TeV LHC Run

The first collisions measured at ATLAS are not expected to be at a center of mass energy of 14 TeV. The plan is that a run using 5 TeV proton beams is done first, resulting in a 10 TeV center of mass energy.

The integrated luminosity that is expected to be collected in this mode is at least 100 pb⁻¹. Hence another 5 million QCD and 6 million compositeness events were generated with a center of mass energy of 10 TeV during Monte Carlo generation. The compositeness samples were produced with $\Lambda = 3, 5, 7.5, 10, 12.5$ and 15 TeV.

The compositeness hypotheses are analogously determined by a fit of the χ spectra with respect to Λ . The systematic uncertainties are used unchanged, except for the JES uncertainty which is increased to 15%. By applying the analysis to the simulated QCD data and hypotheses, the following expected exclusion limits are obtained:

$\int \mathcal{L} \text{ [fb}^{-1}\text{]}$	$\Lambda_{limit} \text{ [TeV]}$	χ_{cut}	$M_{jj} \text{ [TeV]}$
0.03	5.5	3.00	3.50
0.1	6.8	3.00	3.60
0.3	7.9	3.32	3.80
1	9.4	2.46	4.10
3	10.1	2.46	3.95

These are about 3-4 TeV lower than for 14 TeV data. Nonetheless even for 30 pb⁻¹, anticipated to be collected in the first weeks or, at the most, months of data taking, the expected limit exceeds the current Tevatron limit of 2.7 TeV by a factor of 2.

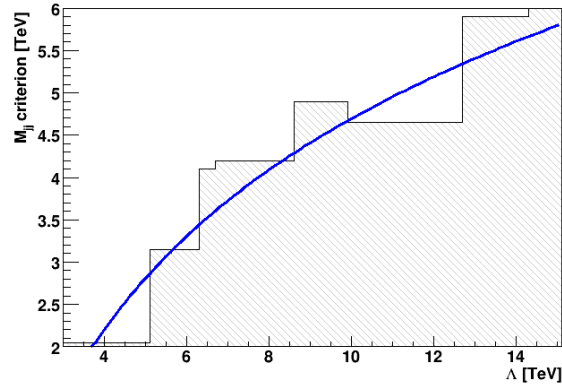


Figure 6.20: Relation between Λ of a hypothesis and the optimized lower limit on M_{jj} , for 300 pb^{-1} , including a fit (blue line)

Exclusions Limits Based on Experimental Data

Once first experimental data is available, another challenge arises that was so far only hinted at. The basic issue is that the optimal values for the parameter χ_{cut} and the lower limit on M_{jj} can not be obtained from data.

For all results above, a sample corresponding to 940 fb^{-1} was used. The statistical errors were increased to be equal to the expectation for the integrated luminosities quoted in the results, while all simulated events were used. This procedure ensured that the exclusion limits given are expected limits, meaning the average of the limits that would result if the ATLAS experiment is repeated several times with the total amount of data being subdivided into sets of e.g. 1 fb^{-1} .

Actual experimental limits will of course be subject to statistical fluctuations. An optimization of the analysis parameters using experimental data would pick out parameter sets where statistical fluctuations towards the desired result are highest, invalidating the analysis.

Therefore these parameters have to be obtained using Monte Carlo data only, ideally including up to date estimates of systematics. To study this procedure the optimal parameters were extracted from the above results.

Figure 6.20 shows the selected lower limits on M_{jj} in dependence of Λ for one integrated luminosity. The distribution of selected values is quite bumpy, mainly due to the systematic uncertainty of the comparison of the fast simulation of ATLAS with data, which is not rising continuously with M_{jj} . In Figure 6.18 on page 136 distinct dips in the uncertainty can be seen. As a result the analysis, with that uncertainty being dominant, uses a single M_{jj} criterion for many Λ values until statistics force the selection to the next minimum.

An improvement of that uncertainty is expected before data-taking, hence the distribution was smoothed by a fit for the presentation of the following procedures.

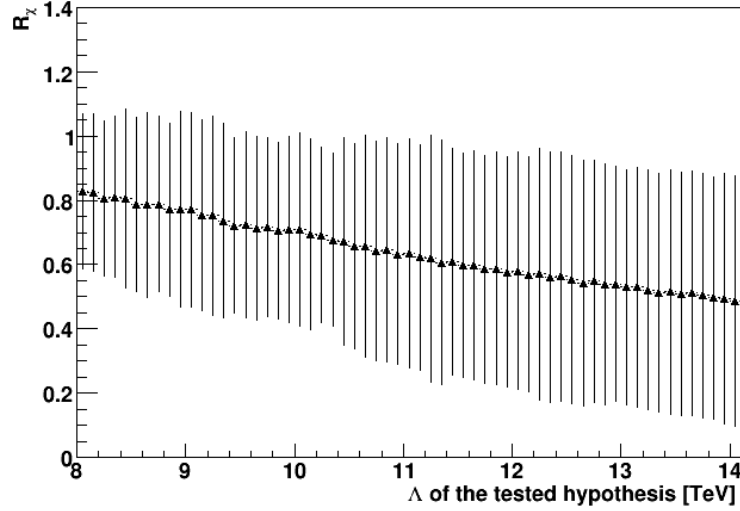


Figure 6.21: R_χ^{theory} together with errors corresponding to $1.64 \sqrt{\sigma_{theory}^2 + \sigma_{data}^2}$, for different hypothesis referred to by their Λ

This is the expected result if the uncertainty of the comparison between fast and full simulation is either a more steady curve, or does not dominate the total uncertainties. As evident from the results this fit is also viable for an analysis including the large uncertainty due to the use of the fast simulation.

As R_{sig} is generally not very sensitive to small changes of χ_{cut} , as e.g. can be seen in figure 6.13 on page 130, a constant χ_{cut} value is chosen for one data sample.

The second challenge arises in the application of the parameters to data. While optimal values for the two parameters can be obtained from Monte Carlo data, to actually select a lower limit on M_{jj} the Λ in the data is required. But Λ is the parameter under study and thus unknown. To solve this problem the following concept was developed² for the presented analysis. While being done by an algorithm and not by eye, it is advantageous to represent it graphically in order to explain its use.

The value required for hypothesis testing is R_{sig} , with the definition:

$$R_{sig} = \frac{|R_\chi^{theory} - R_\chi^{data}|}{\sqrt{\sigma_{theory}^2 + \sigma_{data}^2}} \quad (6.23)$$

²Inspired by the Neyman construction to provide exact coverage for confidence intervals in classical frequentist statistics

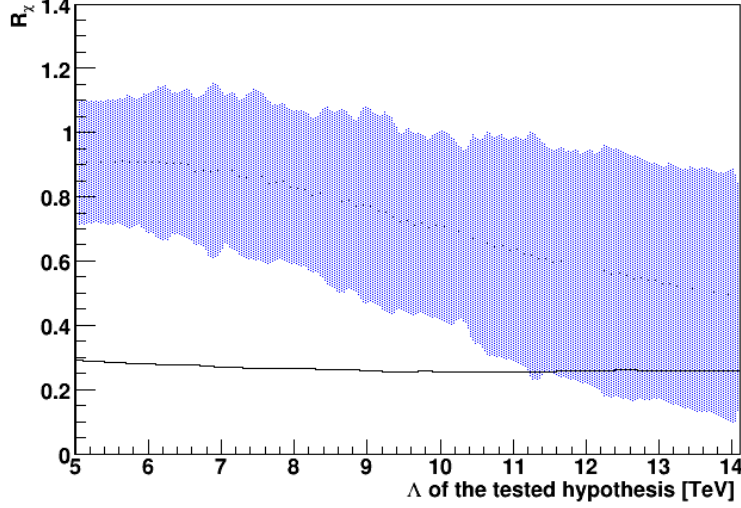


Figure 6.22: Comparison of R_χ^{theory} (blue band) and R_χ^{data} (solid line) for 300 pb^{-1} , including the requirement of $R_{sig} \geq 1.64$

where 'theory' represents one hypothesis.

The basic idea is not to measure a single R_χ^{data} to compare it to different R_χ^{theory} values, but to compare a large number of measured R_χ^{data} values to a large number of hypothesis using different limits on M_{jj} . For the graphical representation the requirement of $R_{sig} \geq 1.64$ can be written as satisfying one of two inequalities:

$$R_\chi^{theory} + (1.64\sqrt{\sigma_{theory}^2 + \sigma_{data}^2}) \leq R_\chi^{data} \quad (6.24)$$

$$R_\chi^{theory} - (1.64\sqrt{\sigma_{theory}^2 + \sigma_{data}^2}) \geq R_\chi^{data} \quad (6.25)$$

In figure 6.21 the left side of both inequalities is shown as a band around R_χ^{theory} . The horizontal axis displays the dependence on Λ and every data point is the R_χ^{theory} for the hypothesis with the corresponding Λ . These values are not constant, but depend on Λ . Additionally they were calculated using the optimal lower limit on M_{jj} . Optimal means that it was found to be the best value to distinguish a Monte Carlo QCD jet sample from the hypothesis of that Λ .

The right side of the two inequalities is a plain value, with no attributed error, as its error is already included on the left side.

Figure 6.22 shows the left side as a blue band, and R_χ^{data} as a solid line. While one could naively expect R_χ^{data} to be constant, as it is measured from a fixed data sample and is not dependent on any hypothesis, this is not the case. In figure 6.22 R_χ^{data} was calculated for each comparison to a Λ hypothesis using the same

M_{jj} limit as for R_χ^{theory} . With a change of Λ the M_{jj} limit changes, and thus also R_χ^{data} . As the data is QCD jet production, R_χ^{data} is roughly independent of M_{jj} , though, and only small fluctuations are visible.

A thin horizontal slice of figure 6.22 hence represents a single test of R_{sig} . If $R_{sig} \geq 1.64$ then R_χ^{data} lies outside the band.

As a result we can reject any Λ where R_χ^{data} is below the error band with a confidence of 95%. For each of these hypotheses the probability that the data is a result of the hypothesis is below 5%. The Λ where R_χ^{data} just enters the band is the 95% exclusion limit.

The above presented construction elegantly circumvents the problem that it is not optimal to simply compare a measured ratio R_χ with a number of hypothesis to find the one just satisfying our 95% confidence requirement. The lower limit on M_{jj} during event selection has to be adjusted to be sensitive to differing hypotheses. The described approach allows the use of optimized analysis parameters obtained from Monte Carlo data for every single hypothesis without making assumptions or introducing a bias in regard to a parameter in the data that is to be measured. Additionally it is a useful tool in case of a discovery. This is shown in the next section.

The exclusion limits obtained by the above method using the simulated instead of measured sample, which was already used to determine the parameters, are by design identical to the limits already given.

6.5 Discovery Reach of the Analysis

6.5.1 Basic Strategy

In this section randomly chosen subsets of the simulated compositeness samples are used to estimate the discovery reach of ATLAS concerning quark compositeness. Subsets were used to have different statistical deviations than those already included in the fits of the spectra that represent the hypothesis. As motivated in the introduction of this chapter, the planned procedure for experimental data is as follows:

- Search for a $3\text{-}\sigma$ evidence of new physics, if none is found, exclusion limits at 95% confidence level are defined
- In case of an evidence for new physics:
 - A confidence interval for the model parameter Λ is established
 - All systematic errors are reexamined in detail for the likely hypotheses, attempting to constrain them more precisely

Thus a broad search for an evidence is done first. In the case of an evidence, already providing a likely range of the parameter Λ , a thorough reanalysis is done with an emphasis on the analysis parameters and likely hypothesis in the hope

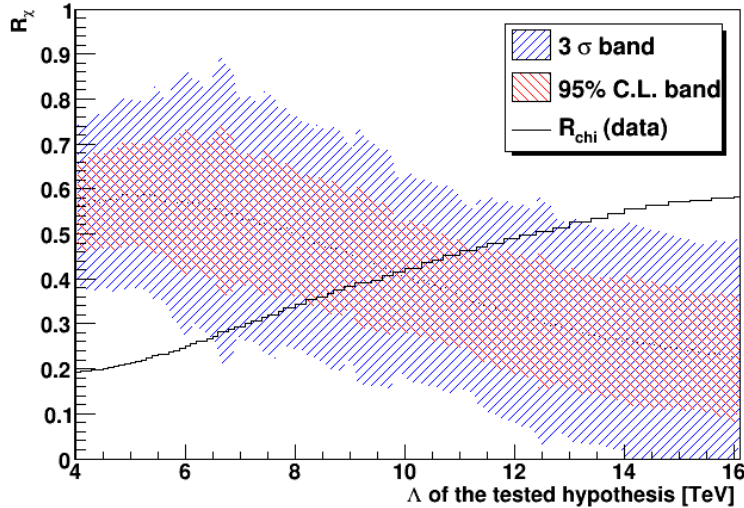


Figure 6.23: Test of R_χ^{theory} vs. R_χ^{data} using the total error, for a sample with $\Lambda = 10$ TeV and 10 fb^{-1}

to either exclude new physics or reach a $5\text{-}\sigma$ discovery. Additional data or a comparison of different analysis concepts may be required to reach that decision.

6.5.2 $3\text{-}\sigma$ Evidence for Compositeness and Confidence Intervals

The search for a $3\text{-}\sigma$ evidence of compositeness faces the same challenge as exclusion limits, namely that different lower limits on the invariant dijet mass M_{jj} are required during event selection to be sufficiently sensitive to different hypotheses. Thus the same method is used, namely calculating the measured R_χ for a range of hypothesis and corresponding limits on M_{jj} . The M_{jj} event selection criterion that is assumed to be optimal is again determined from Monte Carlo data only, to avoid a bias.

The actual procedure to determine the M_{jj} values for the hypotheses is slightly different here. Instead of optimizing the significance of a comparison of QCD data with compositeness hypotheses, the significance of a comparison of expected compositeness data of parameter Λ with the null hypothesis of pure QCD is optimized.

Furthermore an R_{sig} of 3 is required. Figure 6.23 is the graphical representation of results for a simulated data sample with a compositeness scale $\Lambda = 10$ TeV. Every thin vertical slice of this plot again represents a comparison between the measured R_χ , shown as a solid line, and, this time, a $3\text{-}\sigma$ error band around the theoretical prediction of R_χ . If the line is outside the error band for one value of Λ this corresponds to the p-value of that hypothesis being below 0.3% . If the

hypothesis would be true, the probability to obtain that measurement is below 0.3%.

In the example the p-value is below 0.3% for all hypothesis with $\Lambda > 13$ TeV. This is equivalent to a 3- σ upper limit of 13 TeV on Λ , and thus an evidence for new physics. After an evidence has been established the p-value can be relaxed to 5% to define a confidence interval, shown as the red inner band in figure 6.23. The solid line crosses this band at 8.2 TeV and 11.4 TeV. As only hypothesis with a Λ inside this interval are compatible with the measured R_χ with 95% confidence level, this interval is defined to be the 95% confidence interval for Λ . As a side note, as can be seen comparing figure 6.23 with figure 6.22 on page 142, a R_χ line resulting from pure QCD jet production is essentially flat, independently from M_{jj} and thus the JES. Hence it can not result in a measured evidence of new physics due to a wrongly estimated JES uncertainty or unknown JES non-linearity.

For the distinct simulated compositeness sample with $\Lambda = 10$ TeV an integrated luminosity of 3 fb^{-1} is sufficient for an evidence of new physics, while the sample with $\Lambda = 5$ TeV leads to an evidence even with less than 100 pb^{-1} . As the actually simulated values of Λ are too few to provide a discovery reach for a set of integrated luminosities, pseudo-samples derived from the fit functions with the addition of a statistical error were used.

The resulting expectation of required integrated luminosity to claim an evidence for new physics can be found in the following table, for potential experimental data containing compositeness with the quoted values of Λ .

Λ [TeV]	6.8	8.2	9.6	11.2	12.7	14.1	15.2	15.7
$\int \mathcal{L} \text{ [fb}^{-1}\text{]}$	0.1	0.3	1	3	10	30	100	300

Under the assumption that all systematics can be reduced by a factor of 2, and that the parametrization of the systematic uncertainty as a Gaussian distribution is valid even far in the tails, the 5- σ discovery reach of ATLAS is roughly equivalent to the above quoted 3- σ reach with the current estimate of systematics. At least in regards to the JES and the uncertainty coming from the fast simulation of the detector, large improvements are expected to be possible.

With an LHC center of mass energy of 10 TeV, the expected reach for a 3- σ evidence is as follows:

Λ [TeV]	3.1	4.9
$\int \mathcal{L} \text{ [fb}^{-1}\text{]}$	1	3

Results comparable to the above presented can also be obtained using the ratio R and the p_T spectrum. This is not explicitly done here, but the procedure is identical and is used in chapter 7 in an attempt to distinguish between two similar signals of physics beyond the Standard Model.

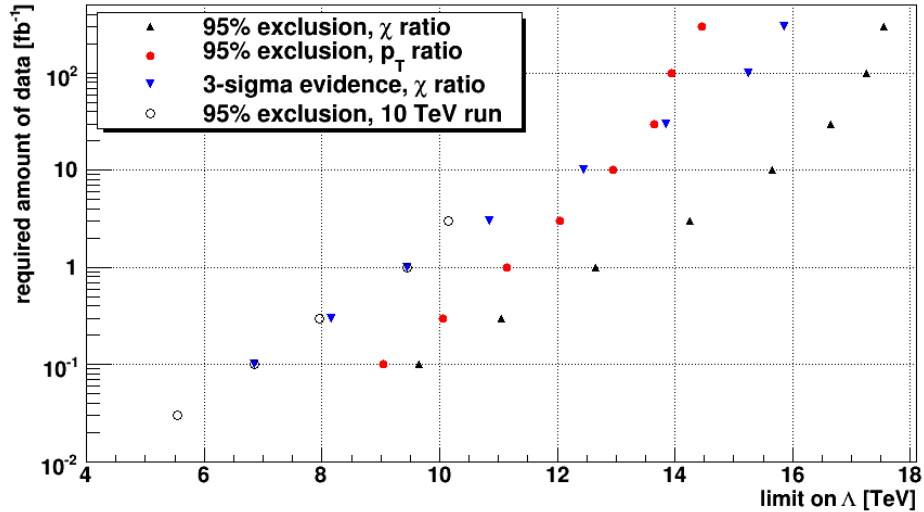


Figure 6.24: Expected reach in the compositeness scale Λ , 95% confidence exclusion limits for two analyses and an estimate of the reach for a $3\text{-}\sigma$ evidence

6.6 Summary of the Expected Sensitivity to Quark Compositeness

After an introduction of the statistical methods and the compositeness model that were used, two detailed analyses were presented. Their concepts were chosen based on a number of simple prototypes excluding most systematic uncertainties. The final refined analyses were used to determine expected 95% confidence exclusion limits on the compositeness scale Λ achievable at ATLAS, including all relevant systematic effects. One challenge that was overcome is the problem that different event selection criteria are required in order to be sensitive to different compositeness hypotheses, and that these can not be obtained from experimental data, nor easily applied to it as the Λ in data is the parameter under study and thus not known.

The expected exclusion limits on Λ are summarized and compared in figure 6.24 figure, for both the analysis based on the inclusive jet production cross section and on jet angular distributions. The analysis based on jet angular distributions was found to be less sensitive to systematic errors, and thus chosen for the determination of the discovery reach of ATLAS. An estimate of the $3\text{-}\sigma$ evidence reach based on pseudo-samples is also included in the figure. For the case of the distinct simulated data sample of $\Lambda = 10$ TeV, e.g. with a dataset corresponding to 10 fb^{-1} , Λ can be constrained to an interval from 8.3 TeV to 11.2 TeV with 95% confidence.

Even with early data corresponding to 100 pb^{-1} and the first months of data taking at a 10 TeV center of mass energy of the LHC, the Λ reach of ATLAS for the left-left isoscalar model of quark compositeness is about 7 TeV. It is thus by a factor of 2 higher than the current best exclusion limit of 2.7 TeV by the Tevatron experiments. The final Λ reach, assuming reduced uncertainties by a factor of 2 compared to our current knowledge, and a very precise JES, is estimated to be roughly 20 TeV.

Chapter 7

Quantum Gravitational Dijet Signatures

This chapter studies the expected parameter exclusion and discovery reach of ATLAS for another effective model of physics beyond the Standard Model, the onset of quantum gravity. As introduced in chapter 2 extra spatial dimensions could lead to a reduced Planck scale M_D , possibly down to the TeV regime. A Planck scale in that regime allows the production of micro black holes or other quantum gravitational effects at the LHC in certain models. From the exclusion or discovery of such a signal parameters of the potential higher dimensional space can be deduced.

First the Monte Carlo samples including an effective implementation of possible quantum gravitational effects are presented, produced by the BlackMax Monte Carlo generator [34]. Afterwards an analysis is performed on these samples, based on the analyses developed in the last chapter to search for quark compositeness, as the expected signal is very similar. The details of the analysis concept can thus be found in section 6.4.3, and only a short overview is given here.

After providing expected exclusion limits for different integrated luminosities of data collected at ATLAS, the analysis strategy for experimental data is discussed. An important aspect is that not only the physics parameters in experimental data are unknown, but also which physics hypothesis to apply. Thus the challenge is to distinguish between different models.

An outlook concludes this chapter, emphasizing that a discovery of new physics at the LHC might require significant additional data or studies to be attributed to a model.

All results in this chapter are considered to be preliminary. The Monte Carlo generator BlackMax that was used to acquire the predictions for dijet production in scenarios with extra dimensions is a very recent development. It generates these predictions using a simple effective model, and furthermore is still in the validation process, which is done by the Heidelberg ATLAS group together with

the BlackMax authors. The following analyses are the first experimental studies performed on BlackMax dijet data, and consequently also the first based on the experimental signals of quantum gravity proposed by P. Meade and L. Randall [10]. Additionally the included systematic uncertainties are only a rough estimate based on the compositeness analysis and simulated QCD data, as no systematics study has been done for BlackMax yet.

The author is of the opinion that nonetheless valuable estimates and conclusions can be obtained using BlackMax, even at this early stage. As there are significant uncertainties regarding the production cross section of micro black holes, all limits given in this chapter should currently be considered to be ballpark figures only when compared to results not based on collider data.

7.1 General Study

7.1.1 Theory and Monte Carlo

The underlying theory for quantum gravitational effects like micro black holes in the TeV regime has already been introduced in chapter 2. Only a brief recapitulation is provided here. Afterwards the simulated data samples and their production is described. This section concludes with a fit of the Monte Carlo predictions with respect to one theory parameter, to be able to check data samples against a large number of hypotheses.

Introduction

In chapter 2 the ADD model of large extra dimensions was introduced. The basic concept is that finite extra spatial dimensions that are smaller than 1mm but significantly larger than the electroweak symmetry breaking range $\sim 10^{-19}m$ can lower the fundamental Planck scale from 10^{16} TeV down to order of 1 TeV. This would put quantum gravitational effects into the range of the LHC. The assumption that semi-classical micro black holes decaying into events with high particle multiplicities are at least highly suppressed at the LHC is adopted here [10]. Consequently the term black hole is used rather loosely to describe a so called Planckian black hole, which is any quantum gravitational resonance or effect.

The Monte Carlo generator BlackMax is used for the presented study. It is a recently developed black hole event generator including the simulation of Planckian black holes in brane world models with low-scale quantum gravity. Details and its exact features can be found in [34]. The expectation of the effective model for dijet like Planckian black holes is an enhancement of the $2 \rightarrow 2$ cross section at the reduced Planck Scale M_D . BlackMax uses the following cross section on parton level, for center of mass energies $\sqrt{s} = M_{BH} > M_D$:

$$\sigma \approx \pi R_S^2 P_2 \quad \text{where} \quad P_2 = e^{-\langle N \rangle} \sum_{i=0}^2 \frac{\langle N \rangle^i}{i!} \quad (7.1)$$

$\langle N \rangle$ is the expected number of particles and R_S is the Schwarzschild radius given as:

$$R_S = \frac{1}{M_D} \left[\frac{M_{\text{BH}}}{M_D} 2^n \pi^{(n-3)/2} \frac{\Gamma[(n+3)/2]}{n+2} \right]^{\frac{1}{n+1}} \quad (7.2)$$

where n is the number of extra dimensions. BlackMax uses the Particle Data Group definition of M_D :

$$M_D^{n+2} = \frac{(2\pi)^n}{8\pi G_D} \quad (7.3)$$

This definition results in cross sections that are up to a factor of 9 higher than those using the Dimopoulos/Landsberg definition:

$$M_{\text{DL}}^{n+2} = \frac{1}{G_D} \quad (7.4)$$

As a conservative estimate this definition is used in the following, and the fundamental $(n+3)$ dimensional Planck scale is written as M_{DL} to avoid any confusion. The cross sections were converted to agree with this definition for each n [35].

Monte Carlo Samples

The Monte Carlo generator BlackMax produces pure samples of dijet-like events produced by micro black holes. To obtain a consistent sample as expected from experimental data, these events have to be mixed with QCD jet production. 10 million QCD jet events using differing selection intervals on jet p_T on generator level were produced with the PYTHIA Monte Carlo generator and the fast simulation of the ATLAS detector. These events were weighted by their cross sections and merged, resulting in a continuous sample starting at a jet p_T of 560 GeV and corresponding to 930 fb^{-1} of ATLAS data. Statistically smaller samples were emulated by an increase of statistical errors instead of reducing the amount of events.

For each micro black hole scenario 1 million events were generated, resulting in a total of 18 Million BlackMax events. The parton level output of BlackMax was interfaced with PYTHIA and the ATLAS Offline Software for decay or hadronization of the final state partons and the simulation of the ATLAS detector and reconstruction. As the Planck scale is the natural cut-off no further event selection was done on generator level. The micro black hole events were merged with the above QCD samples to result in consistent samples of high p_T jet production in a micro black hole scenario.

Concerning this simple merge, the black hole production is in the non-perturbative regime, thus it is unknown how to treat interference. There is e.g. the possibility

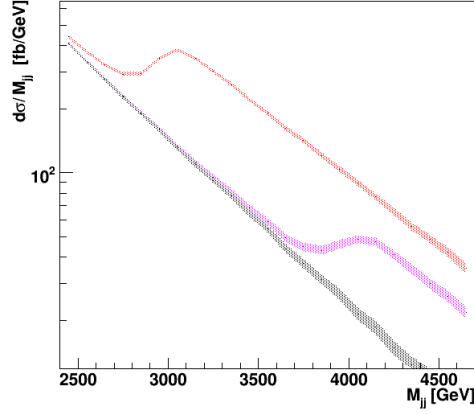


Figure 7.1: Expected M_{jj} spectrum for (top to bottom) $M_{DL} = 3$ TeV, 4 TeV and QCD

that QCD jet production is suppressed at high scales, assuming a basic geometrical cross section for micro black hole production. For all partons entering their combined event horizon black hole production could be the only process possible, which is often called the end of short-distance physics. For the samples used the cross sections are of the order of the QCD expectation in the black hole signal region. Hence the QCD contribution is not negligible and an uncertainty of the expected total cross section for jet production results from the simple merge of samples.

For all samples jet finding and reconstruction was done using a seeded cone algorithm with $R = 0.4$, and jets are reconstructed starting at $p_T = 10$ GeV and $|\eta| \leq 5$.

The example of an inclusive M_{jj} spectrum is shown in figure 7.1.

Fit of the Angular Spectra

The samples that were produced for the quantum gravity hypotheses are classified by two parameters. The first one is the number n of extra-dimensions in the model. The second one is the reduced $(3+n)$ dimensional Planck scale M_{DL} .

To obtain a prediction of jet angular distributions for any M_{DL} inside a given range, the χ spectra were fitted analogous to the quark compositeness case, by the function:

$$f(x) = D + C(1 + e^{A(B - \ln x)})^{-1} \quad (7.5)$$

where A , B , C and D are free parameters and $x = \frac{1}{M_{DL}^2}$. This fit was done for every value of n and for all lower limits on M_{jj} used during event selection.

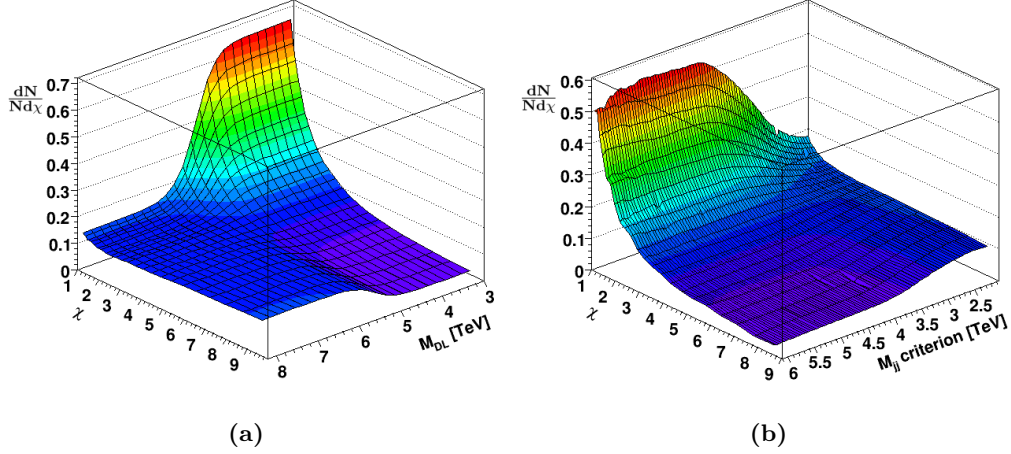


Figure 7.2: Results of the fit of the χ spectra, (a) for a fixed M_{jj} criterion of 4 TeV, (b) for a fixed M_{DL} of 5 TeV

For the distinct simulated values of M_{DL} the results of the fit agree with the measured value with a precision of 2%, being negligible to other systematic errors. An example result is displayed in figure 7.2.

By use of this fit, data sets can be compared with a hypothesis of any arbitrary value M_{DL} .

7.1.2 Exclusion Limits Based on Angular Distributions

Dijet production via micro black holes results in a more isotropic distribution of jets, in contrast to the forward peaked distribution of the dominant t-channel gluon exchange of QCD jet production, as visible in figure 7.3. Based on this an analysis on a given data set can be performed analogous to the compositeness case, as presented in the previous chapter.

For each event a parameter χ is determined, and for each sample after event selection on M_{jj} a parameter R_χ :

$$\chi = e^{|\eta_1 - \eta_2|} \quad R_\chi = \frac{N_{events}(\chi \leq \chi_{cut})}{N_{events}(\chi > \chi_{cut})} \quad (7.6)$$

where χ_{cut} is an arbitrary parameter.

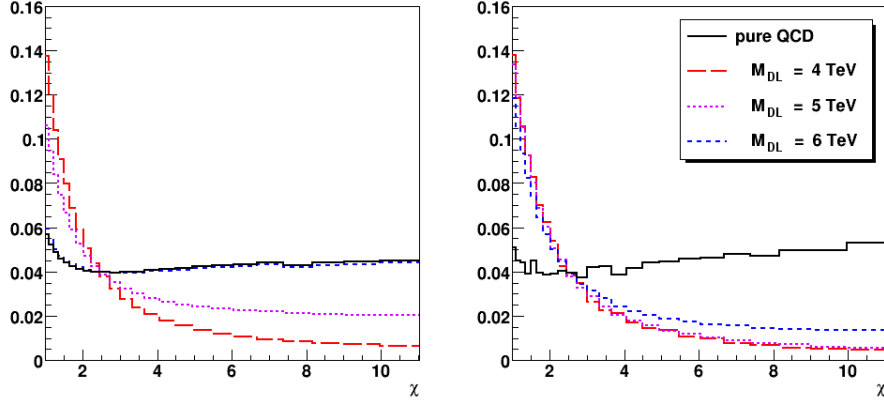


Figure 7.3: Expected distributions of $\chi = e^{|\eta_1 - \eta_2|}$, with an event selection on M_{jj} greater than 3 TeV on the left and 5.5 TeV on the right, $n = 4$

Systematic Uncertainties

The same systematic uncertainties as for the compositeness analyses were used, which can be found in section 6.4.3:

- Accuracy of the jet η and ϕ measurement
- PDF uncertainties and NLO k-factors
- Comparison of the full and fast simulation of ATLAS
- A jet energy scale uncertainty of 10%

One item of note are the uncertainties of PDFs and the NLO corrections. These have not been studied for the BlackMax Monte Carlo generator yet, as it is still in the validation process. Thus the results obtained for QCD jet production were applied as theoretical uncertainties. For the case of PDF uncertainties this is in principle a sensible, if imprecise, approach. Concerning uncertainties of the NLO corrections this is more critical, though. In addition to the use of the simple cross section for micro black holes we do expect that perturbative QCD breaks down at the onset of quantum gravity. Hence QCD NLO corrections basically should not be applied to micro black hole events. The data samples do also contain a large number of QCD jet events, though, and applying an additional uncertainty to the micro black hole events can be seen as a conservative precaution. The uncertainty on the total cross section due to possible interference of quantum gravity and QCD is e.g. expected to be roughly of the same order of magnitude as the NLO correction uncertainties for QCD.

Additionally there are large uncertainties on the black hole production cross section coming e.g. from:

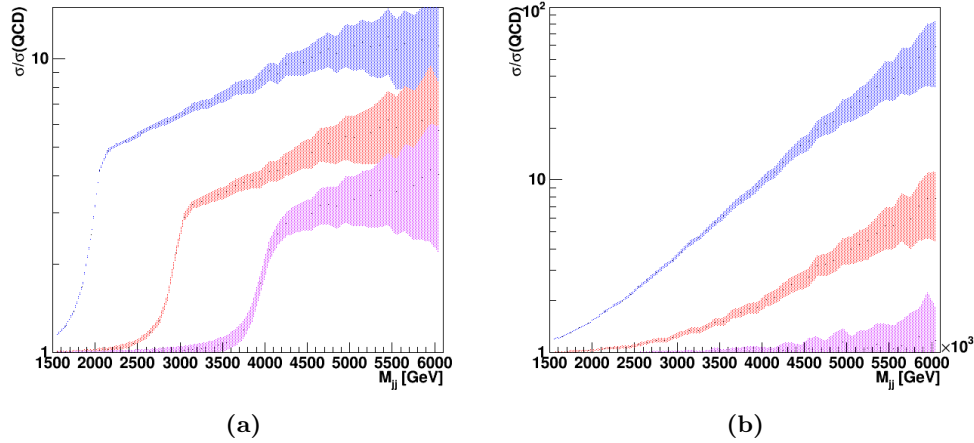


Figure 7.4: Inclusive M_{jj} spectra divided by the QCD expectation for (from top to bottom) (a) micro black holes with M_{DL} of 2, 3 and 4 TeV, (b) compositeness with Λ of 3, 5 and 10 TeV. Error bands represent statistical errors with 1 fb^{-1} of data

- Planck scale definition: cross sections differ by a factor 1.4 to 9 for common definitions and $n = 2$ to 7
- Theoretical uncertainties in the dynamics of production process, e.g. including a form factor in hard-disk cross sections can change them by a factor of about 2
- Cross sections could be up to 6 orders of magnitude lower if not all energy is trapped behind the apparent horizon

The above effects are not included as theoretical uncertainties in the analysis due to their size, as including them would prevent any predictions. Concerning the definition of the Planck scale the Dimopoulos/Landsberg definition was conservatively chosen, resulting in significantly lower cross-sections for the same Planck Scale M_D of the Particle Data Group definition (by a factor of up to 9). For the other effects, the choices used in the BlackMax Monte Carlo generator are treated as fixed assumptions of the studied model. Hence any predictions are made for the model including these assumptions.

As current analyses using the Hawking Radiation phase of classical micro black holes have the same uncertainties of the production cross sections, their results can be compared to those given in this chapter.

As the simulated micro black hole signal has a short and steep rise roughly at $M_{jj} = M_{DL}$ (figure 7.4), in comparison to the slow steady rise of compositeness

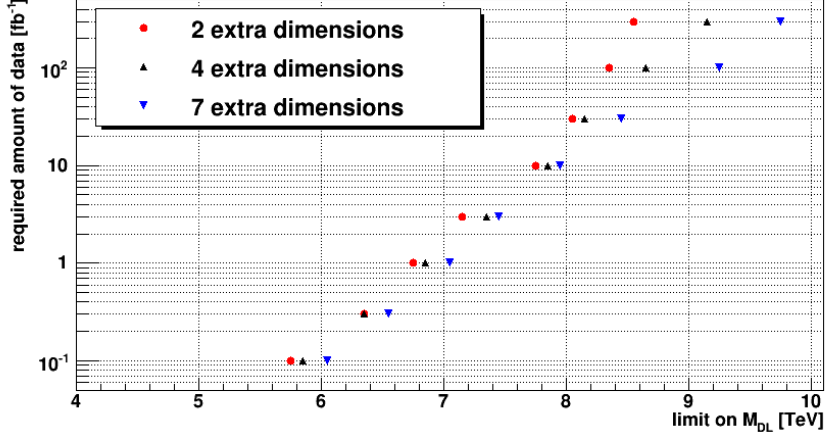


Figure 7.5: Expected reach for M_{DL} , 95% confidence exclusion limits

cross sections starting far below Λ , the maximum allowed M_{jj} criterion plays a larger role. Thus the included systematic uncertainties were assumed to increase linearly from M_{jj} of 6 TeV to 7 TeV, and the allowed range of the M_{jj} criterion was increased to 7 TeV.

A dedicated systematics study for this signal should explore even higher M_{jj} values, as the maximum for this event selection criterion has an effect on the reach concerning micro black holes.

Resulting Exclusion Limits on M_{DL}

The pure QCD jet production sample is compared to the hypotheses by calculating:

$$R_{sig} = \frac{R_{\chi}^{BH} - R_{\chi}^{QCD}}{\sqrt{\sigma_{BH}^2 + \sigma_{QCD}^2}} \quad (7.7)$$

where an index of BH denotes one hypothesis of additional dijet events through micro black hole production. M_{DL} is varied between 3 TeV and 10 TeV and values of the parameter $\chi_{cut} = e^{(0.1i)}$ with $1 \leq i \leq 20$ are used. The event selection criterion of minimum allowed invariant dijet mass M_{jj} is varied between 3 TeV and 7 TeV in steps of 0.05 TeV.

R_{sig} is determined for all possible combinations of M_{DL} , M_{jj} , χ_{cut} , and a set of integrated luminosities. For each integrated luminosity and M_{DL} the parameters M_{jj} and χ_{cut} were selected to result in a maximum of R_{sig} .

Resulting expected exclusion limits on M_{DL} are given in the following table and figure 7.5, for n extra dimensions.

$\int \mathcal{L} [\text{fb}^{-1}]$	lower limit on M_D [TeV]		
	n = 2	n = 4	n = 7
0.1	5.7	5.8	6.0
0.3	6.3	6.3	6.5
1	6.7	6.8	7
3	7.1	7.3	7.4
10	7.7	7.8	7.9
30	8.0	8.1	8.4
100	8.3	8.6	9.2
300	8.5	9.1	9.7

The optimal event selection limits on M_{jj} are around 5 TeV for 0.1 fb^{-1} , steadily rising to 6.5 TeV at 3 fb^{-1} , and close to the maximum allowed value of 7.0 TeV for higher integrated luminosities. The χ_{cut} is around 3 up to 30 fb^{-1} and goes down to 2 for the largest samples.

The above limits are significantly higher than expected limits obtained by classical micro black hole analyses. As these search for classical black holes far above the Planck scale M_{DL} , the kinematic limit at the LHC effectively constrains their reach to below $M_{DL} = 2 \text{ TeV}$. Current experimental limits from collider experiments are 1.6 TeV for $n = 2$, 1.2 TeV for $n = 4$ and 0.8 TeV for $n = 7$.

7.1.3 Strategy for Experimental Data

For experimental data the same challenges arise as in the compositeness case, described in the previous chapter. As a summary, the event selection on M_{jj} needs to be varied depending on the hypothesis to achieve the best limits for the $(3+n)$ dimensional Planck scale M_{DL} , but as the M_{DL} in the data is unknown beforehand, the correct optimal parameter determined from Monte Carlo samples is not known. As a solution the comparison of data and hypothesis is done for a large number of hypotheses, using the optimal value for each hypothesis. This procedure is visualized in figure 7.6. The solid line represents the measured value while the error band is the prediction for different hypotheses including all experimental and theoretical errors and uncertainties. Each thin vertical slice of the figure is one comparison to a single hypothesis using one event selection criterion. All hypotheses with an M_{DL} where the measured value is outside the error band exclude that the measured value is a result of the hypothesis, with 95% confidence.

The highest M_{DL} value where the measured R_χ is still outside the error band is the sought after 95% upper exclusion limit for that data sample. All limits on M_{DL} have to be acquired in dependence of the number of extra dimensions of the hypothesis.

7.1.4 Discovery Considerations

As discussed in the previous chapter, the above approach can also be applied to data containing evidence of new physics. The determination of the optimal event

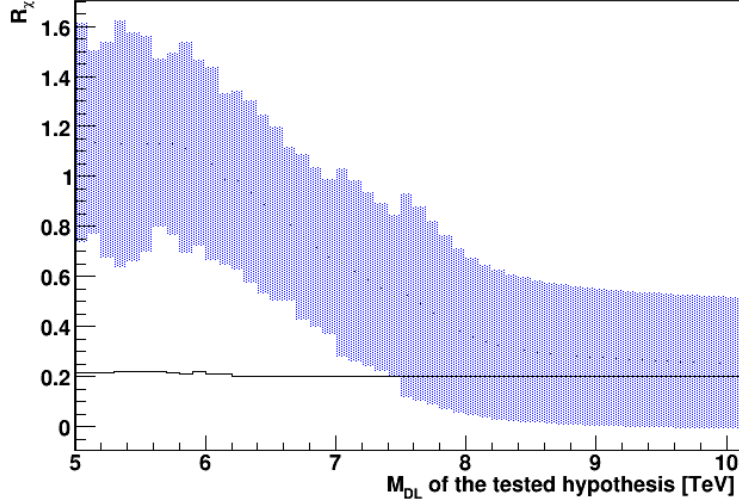


Figure 7.6: Comparison of R_χ^{theory} (blue band) and R_χ^{data} (solid line) for 10 fb^{-1} , including the requirement of $R_{sig} \geq 1.64$, $n = 4$

selection on M_{jj} is redone with Monte Carlo samples, this time optimizing the significance of comparing simulated new physics data derived from the fit functions to the expectation of the null hypothesis.

Figure 7.7 graphically shows the result for a simulated data sample with $n = 4$ and $M_{DL} = 6 \text{ TeV}$. The requirement on R_{sig} is 3 for the outer band and 1.64 for inner band. The values determined from the sample lie above the outer band for $M_{DL} > 7.3 \text{ TeV}$, defining a 3 sigma upper limit for M_{DL} which is an evidence for new physics. With the inner band a 95% confidence interval on M_{DL} can be given, from 5.4 to 6.7 TeV.

The expected discovery reach for the case of $n = 4$ extra dimensions is:

$M_{DL}[\text{TeV}]$	5.1	5.4	5.8	6.9	7.6	8.2	8.7	8.9
$\int \mathcal{L} [\text{fb}^{-1}]$	0.1	0.3	1	3	10	30	100	300

The expected experimental signals of dijet micro black holes and quark compositeness concerning inclusive jet production are very similar. This has the advantage that the same type of analysis can be applied to define exclusion limits for both models. However in case of an evidence for new physics the challenge is to distinguish the two concepts.

7.1.5 Comparison Using χ Based Analyses

To illustrate the above challenge a simulated micro black hole sample with $M_{DL} = 6 \text{ TeV}$, $n = 4$ and corresponding to 3 fb^{-1} of integrated luminosity was used as ex-

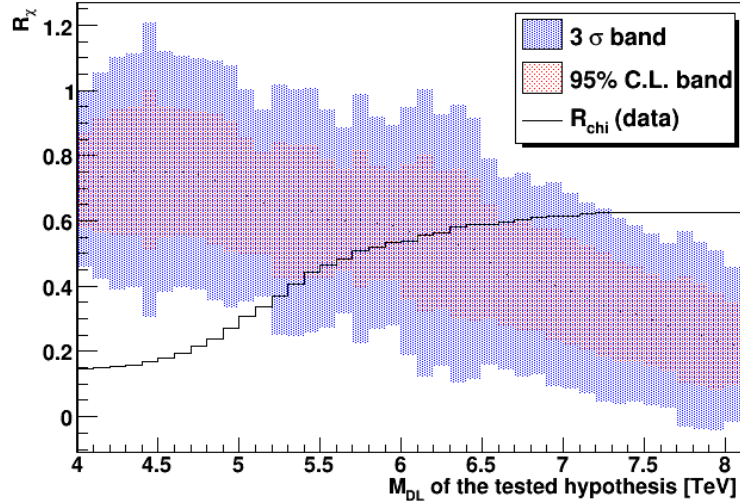


Figure 7.7: Test of R_χ^{theory} vs. R_χ^{data} using the total error, for a sample with $M_{DL} = 6$ TeV, $n = 4$ and 100 fb^{-1}

perimental data for the compositeness analysis using angular distributions, which was described in the last chapter. Using the analysis described in this chapter the sample leads to an evidence of new physics. The result of the compositeness analysis for this sample is visualized in figure 7.8. It also reveals evidence for new physics, and provides a confidence interval for the compositeness scale Λ , from 9.7 to 12.4 TeV, resulting in a central value of $\Lambda = 11$ TeV. This is not a contradiction considering the data sample that was analyzed, as the confidence interval is only valid under the assumption that the model of quark compositeness is true. The analysis, being used for both types of signals, is of course sensitive to both even when using the wrong hypothesis.

Figure 7.9 shows the actual χ spectra for the data sample and for the compositeness hypothesis with Λ equal to the determined central value, both for the optimized M_{jj} criterion of 4.5 TeV. The two spectra are very similar. Thus, even by analyzing the full χ spectrum instead of the ratio R_χ , no distinguishing power between the two models can be gained.

One option is to attempt to gain additional information from the inclusive jet production cross section. If this leads to a contradiction of the confidence intervals for one model, it can be interpreted as a hint that the data is not in good agreement with one of the models. E.g. if the compositeness search sets Λ to 8 TeV and 12 TeV using the two approaches, while the micro black hole hypothesis results in $M_{DL} = 6$ TeV in both cases, the micro black hole model would describe the data more consistently.

Evidence of new physics and confidence intervals were not studied using the

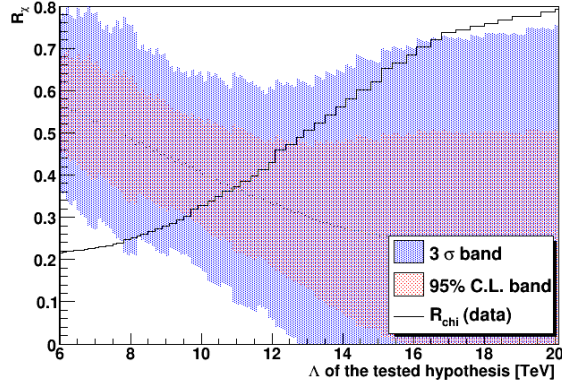


Figure 7.8: R_{χ}^{data} vs. R_{χ}^{theory} including the total error, for a sample with $M_{DL} = 6$ TeV, $n = 4$ and 3 fb^{-1} , using quark compositeness hypotheses

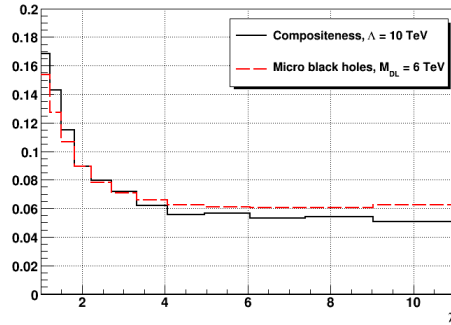


Figure 7.9: Example comparison of χ spectra of micro black holes with $n = 4$ and quark compositeness, the minimum M_{jj} used for event selection is 4.5 TeV

inclusive jet cross section spectra in the previous chapter, but results with the ratio R defined there can be obtained in analogy to angular distributions. Figure 7.10 is the result of a search for compositeness based on the jet p_T spectrum and using the simulated micro black hole sample as data. The 95% confidence interval is determined as 8.6 to 11.5 TeV. Hence the result is consistent with the that of the χ based analysis.

Using a simple ratio of events above and below a limit in jet p_T is not able to provide any distinguishing power.

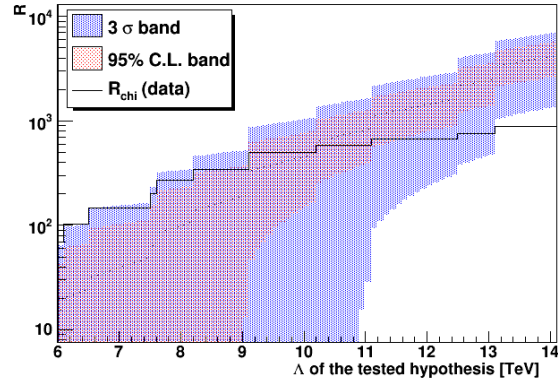


Figure 7.10: The black hole sample plugged into a compositeness analysis using a ratio of events defined on the jet p_T spectrum

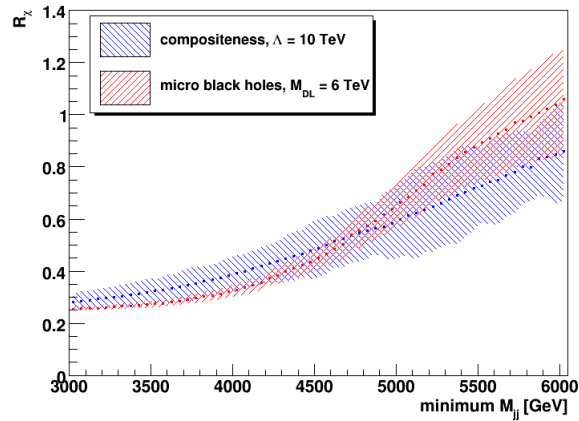


Figure 7.11: R_χ in dependence of the M_{jj} criterion, for compositeness including the theoretical uncertainties, and for micro black hole including the experimental uncertainties

The Scaling of R_χ with M_{jj}

With the optimized event selection on the invariant dijet mass M_{jj} it is not possible to distinguish the sample of dijet-like black hole events from quark compositeness using the χ spectrum. As additional information is required one option is the scaling of R_χ with M_{jj} .

Principally, a steeper rise is expected for the black hole case, and can indeed be seen in figure 7.11. The error band on the micro black hole case is one sigma of the statistical and experimental error, while the one sigma band around the

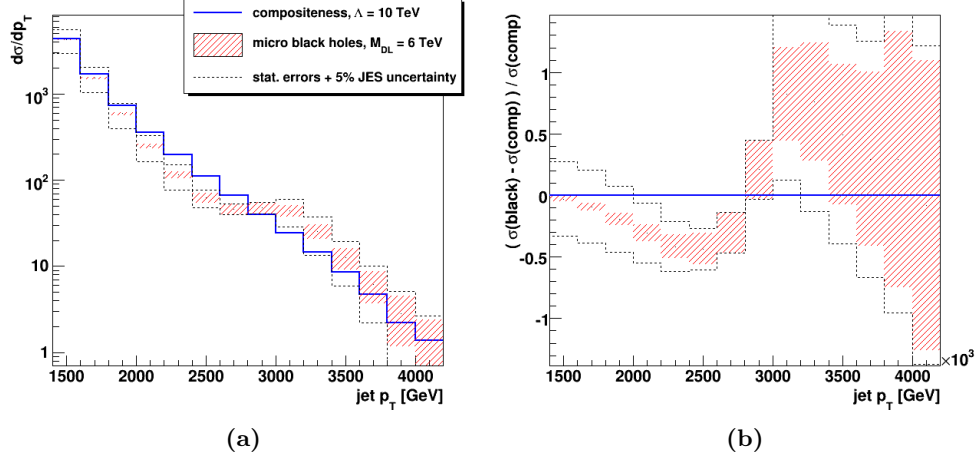


Figure 7.12: Inclusive jet production cross section of the micro black hole sample, compared to the compositeness hypothesis, (a) the respective jet p_T spectra (b) the relative difference of the black hole spectrum to the compositeness expectation. Error bands represent statistical errors with 3 fb^{-1} of data

compositeness prediction represents the theoretical uncertainties. Including these uncertainties, no decision can be made.

7.1.6 Study of the p_T Spectrum

Figure 7.12 compares the ratio of inclusive jet production cross sections for the two models of new physics including statistical errors. The p_T spectrum was subdivided into broad intervals to reduce the statistical uncertainty. The effect of the addition of an example JES uncertainty of 5% is also shown.

In addition theoretical uncertainties have to be considered. For the compositeness hypothesis the combination of uncertainties of the PDFs, the NLO corrections and possible electroweak Standard Model corrections result in an uncertainty of the cross section of up to 80%. While these uncertainties are not likely to cause a sudden jump of the cross section, the expectation is that compositeness can not be clearly ruled out as the source for the signal. Only hints towards the more likely model can be determined, e.g. using a fit.

7.1.7 Alternative Approaches

Due to the above presented challenge to distinguish the two presented effective models of new physics in experimental data, it may be necessary to investigate alternative approaches. One such approach, proposed in [10], is to additionally utilize lepton channels. Another possibility is to study the fractions of different quark types in dijet events, as quantum gravitational effects could possibly result

in a higher fraction of heavy quarks compared to quark-quark scattering in the compositeness case.

At the time of writing no studies of these approaches exist.

7.1.8 Conclusions

The analyses presented in this thesis are robust against systematic uncertainties and provide a very good reach for the exclusion or discovery of new physics in dijet-like events. But they are not sufficient to distinguish between different models. Even a detailed study of additional information obtained from inclusive jet spectra might not be sufficient in the case of an evidence of new physics, and new approaches would have to be developed based on different topologies or signatures. The dominating factor leading to this conclusion are mainly theoretical uncertainties. But if these are significantly reduced the number of events to distinguish the two models is still expected to be considerably higher than that required to discover the evidence for new physics.

7.2 Summary

In this chapter dijet-like micro black hole events that could result from a reduced $(3+n)$ dimensional Planck scale M_{DL} were studied using simulated data generated by the BlackMax Monte Carlo generator. Expected exclusion limits on M_{DL} and the discovery potential were determined for different numbers of extra dimensions. These results are considered to be preliminary due to the Monte Carlo generator and physics model still being a very recent development. The insight was gained that micro black hole events having a dijet topology are not only similar to quark compositeness events, but may be indistinguishable in experimental data using purely jet based analyses.

But most importantly it has been shown that analyses developed to search for quark compositeness are in principle very powerful tools to look for micro black holes and quantum gravity at the LHC, having a very high reach in M_{DL} of up to 10 TeV. Compared to classical black hole analyses this is a gain by a factor of 5.

Even for very early ATLAS data the expected limits on the Planck scale M_{DL} are a factor of 4 to 6 higher than the current experimental limits of 1.6 to 0.8 TeV (for 2 to 7 extra dimensions) [11]. The different expected exclusion reaches for the parameter M_{DL} in dependence of the number of extra dimensions are summarized in figure 7.13, together with the exemplary estimate of the reach for a 3-sigma evidence for 4 extra dimensions.

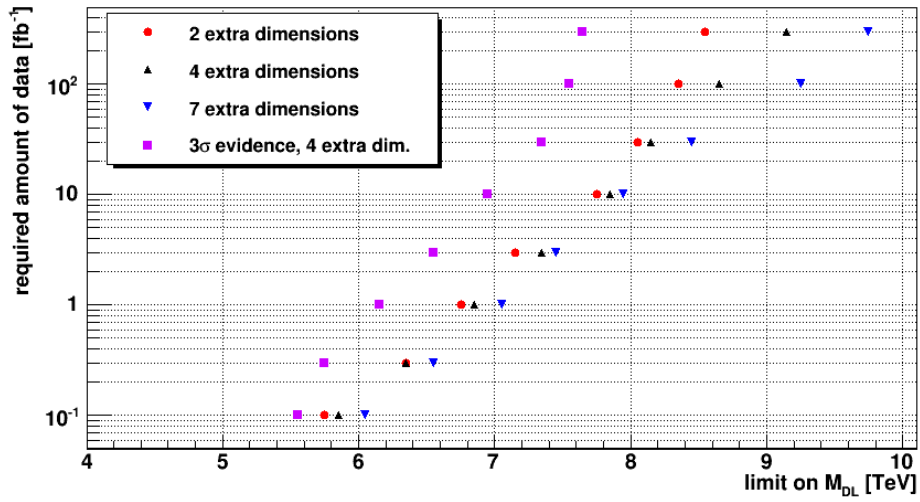


Figure 7.13: Expected reach in the $(n+4)$ dimensional Planck scale M_{DL} , 95% confidence exclusion limits for $n = 2, 4$ and 7 and an estimate of the reach for a 3-sigma evidence for $n = 4$

Chapter 8

Summary and Outlook

This thesis was focused on jet physics at the ATLAS experiment. After a short physics introduction and the description of the ATLAS detector and the Large Hadron Collider (LHC), a short review of jet physics, their simulation and measurement was given.

Chapter 5 presented the concept of an inter-calibration of the jet energy scale (JES). The challenge posed by the difference between the comparatively low energy scale that can be verified by common in-situ methods and the highest energetic jets was overcome. This is possible by the use of the large Quantum Chromodynamics (QCD) jet production cross section, by selecting those events containing one jet that is at a significantly higher scale than all others. Based on Monte Carlo data the systematic uncertainties of the method are expected to be well under control, and the JES can be linearized up to transverse jet momenta of several TeV with a precision better than 3%. Utilizing an in-situ calibrated absolute JES at lower energies, the JES can be bootstrapped to far higher energies without a significant loss of accuracy. Systematic effects have to be reevaluated with the first collision data, but the prospects of the proposed method are very promising.

In chapter 6 the focus was on physics measurements. Several prototype analyses were presented to study inclusive jet cross sections and angular distributions, leading to the selection of two analyses for an in-depth study, one based on the differential jet cross section $\frac{d\sigma}{dp_T}$ and one based on angular jet distributions. The general conclusion derived from the results is that at least for early data taking at ATLAS, analyses based on angular distributions are more promising due to their lower susceptibility to systematic errors. Estimated 95% exclusion limits on the compositeness scale Λ , for the left-left isoscalar compositeness model with destructive interference, are above 5 TeV even for earliest collision data, and are expected to be above 15 TeV in the long term. Expected 3- σ discovery reaches are of the same order. This surpasses the current best limits of 2.7 TeV, based on the quark-quark coupling, by a factor of 2 to 6. Thus the validity of perturbative QCD and the Standard Model can be probed at ATLAS up to unprecedented scales with a good precision.

The hypotheses for new physics were supplemented by an effective model of quantum gravity in chapter 7. Simulated data containing ADD black hole behavior in a brane world scenario with extra dimensions was tested against QCD behavior using the analyses developed for the compositeness case. The analyses were shown to be viable for the micro black hole scenario, and values of the $(n+3)$ dimensional Planck Scale of 5.7 to 9 TeV can be probed, depending on the available integrated luminosity and for $n = 4$ to 7 extra dimensions. Furthermore it was shown that despite a clear difference between these spectra and the compositeness case, systematic and statistical errors severely limit the ability to distinguish between the two models in case of an evidence of new physics in experimental data. To gain significant distinguishing power complementary approaches to inclusive jet measurements are required.

In conclusion jet data even from an early phase of ATLAS and the LHC is a very powerful experimental probe. Until the arrival of the first data theoretical uncertainties should be reexamined, with the expectation that further simulated data and the most recent PDF sets can lead to a significant reduction. The main challenge after the start of data taking will be to constrain experimental uncertainties like the JES error, e.g. using the proposed multi-jet bootstrapping method.

Bibliography

- [1] Derek Greenwood W. Cottingham. *An Introduction to the Standard Model of Particle Physics*. 1998.
- [2] Stephen P. Martin. *A Supersymmetry Primer*, 1997.
- [3] Greg Landsberg. Black Holes at Future Colliders and Beyond: a Topical Review. *J.PHYS.G*, 32:R337, 2006.
- [4] C. Amsler et al. Review of particle physics. *Phys. Lett.*, B667:1, 2008.
- [5] Jogesh C. Pati and Abdus Salam. Lepton number as the fourth "color". *Phys. Rev. D*, 10(1):275–289, Jul 1974.
- [6] Harari H. A schematic model of quarks and leptons. *Phys. Lett. B*, 86, April 1979.
- [7] Sundance O. Bilson-Thompson. A topological model of composite preons, 2005.
- [8] D0 Collaboration. The Dijet Mass Spectrum and a Search for Quark Compositeness in $p\bar{p}$ Collisions at $\sqrt{s} = 1.8$ TeV. *Physical Review Letters*, 82:2457, 1999.
- [9] Nima Arkani-Hamed, Savas Dimopoulos, and Gia Dvali. The Hierarchy Problem and New Dimensions at a Millimeter. *Physics Letters B*, 429:263, 1998.
- [10] Patrick Meade and Lisa Randall. Black Holes and Quantum Gravity at the LHC, 2007.
- [11] D. M. Gingrich. Experimental Limits on the Fundamental Planck Scale in Large Extra Dimensions. 2008.
- [12] G Aad. The ATLAS Experiment at the CERN Large Hadron Collider. *J. Instrum.*, 3:S08003, 2008.
- [13] J. M. Campbell, J. W. Huston, and W. J. Stirling. Hard Interactions of Quarks and Gluons: a Primer for LHC Physics. *REPT.PROG.PHYS.*, 70:89, 2007.

-
- [14] *ATLAS Level-1 Trigger Technical Design Report*. Technical Design Report ATLAS. CERN, Geneva, 1998.
- [15] *ATLAS high-level trigger, data-acquisition and controls : Technical Design Report*. Technical Design Report ATLAS. CERN, Geneva, 2003.
- [16] R. P. Feynman. Proceedings of the 3rd Topical Conference on High Energy Collision of Hadrons. 1969.
- [17] Murray Gell-Mann. A Schematic Model of Baryons and Mesons. *Phys. Lett.*, 8:214–215, 1964.
- [18] G. Zweig. Preprint CERN-8182/Th.401 and CERN-8182-TH-401. 1964.
- [19] S. D. Drell and Tung-Mow Yan. Partons and their applications at high energies. *Ann. Phys.*, 66:578, 1971.
- [20] Daniel Stump, Joey Huston, Jon Pumplin, Wu-Ki Tung, H. L. Lai, Steve Kuhlmann, and J. F. Owens. Inclusive Jet Production, Parton Distributions, and the Search for New Physics. *JHEP*, 0310:046, 2003.
- [21] Torbjorn Sjostrand, Stephen Mrenna, and Peter Skands. PYTHIA 6.4 Physics and Manual. *JHEP*, 0605:026, 2006.
- [22] A. D. Martin, R. G. Roberts, W. J. Stirling, and R. S. Thorne. Physical Gluons and High E_T Jets. *Physics Letters B*, 604:61, 2004.
- [23] P. M. Nadolsky, H. L. Lai, Q. H. Cao, J. Huston, J. Pumplin, D. Stump, W. K. Tung, and C. P. Yuan. Implications of CTEQ global analysis for collider observables, 2008.
- [24] S. Moretti, M. R. Nolten, and D. A. Ross. Weak corrections and high E_T jets at Tevatron. *Physical Review D*, 74:097301, 2006.
- [25] Yu.L. Dokshitzer. Report of the Hard QCD Working Group. In *Proc. Workshop on Jet Studies at LEP and HERA*, Durham, Dec 1990.
- [26] Gerald C. Blazey, Jay R. Dittmann, Stephen D. Ellis, V. Daniel Elvira, K. Frame, S. Grinstein, Robert Hrosky, R. Piegaiia, H. Schellman, R. Snihur, V. Sorin, and Dieter Zeppenfeld. Run II Jet Physics: Proceedings of the Run II QCD and Weak Boson Physics Workshop, 2000.
- [27] *ATLAS detector and physics performance: Technical Design Report*. Technical Design Report ATLAS. CERN, Geneva, 1999.
- [28] P. Loch. Hadronic calibration with early data. In *ATLAS Calorimeter Calibration Workshop*, Costa Brava, Sep 2006.

- [29] S. Agostinelli et al. G4—a simulation toolkit. *Nuclear Instruments and Methods in Physics Research Section A: Accelerators, Spectrometers, Detectors and Associated Equipment*, 506(3):250 – 303, 2003.
- [30] Pavel Weber. *ATLAS Calorimetry: Trigger, Simulation and Jet Calibration*. PhD thesis, Kirchhoff-Institut for Physics, Heidelberg, 2008.
- [31] The ATLAS Collaboration. Jet Energy Scale: In-situ Calibration Strategies in ATLAS, 2008.
- [32] M. L. Mangano and M. Moretti and F. Piccinini and R. Pittau and A. D. Polosa. ALPGEN, a generator for hard multiparton processes in hadronic collisions. *JHEP*, 0307:001, 2003.
- [33] L. Pribyl. Quark Compositeness in ATLAS in release 11.0.4X. 2008.
- [34] De-Chang Dai et al. BlackMax: A black-hole event generator with rotation, recoil, split branes, and brane tension. *Phys. Rev. D*, 2008.
- [35] V. Lendermann. Definitions of D-dimensional Planck scale.

Acknowledgements

After the presentation of my work of the last years, it is my pleasure to thank those who supported me and thus made this thesis possible.

First I would like to express my gratitude to Prof. Karlheinz Meier, for giving me the opportunity to work on this thesis, his contagious enthusiasm for particle physics and all the guidance over the years.

I am also very grateful that Prof. Carlo Ewerz kindly agreed to act as a referee for this thesis. Many thanks for the time and effort required for this task!

Further thanks go to all people I have directly worked with in the last years. Of special mention are Dr. Victor Lendermann, Prof. Hans-Christian Schultz-Coulon and Dr. Pavel Weber for the countless and fruitful discussions providing insight and guidance. But the support from the whole KIP ATLAS group and also my colleagues in the ATLAS Jet Performance group and the Exotic Physics group should not go unmentioned.

Concerning the trigger and commissioning work early in my thesis, not included in this dissertation, my utmost gratitude goes to Klaus Schmitt, Dr. Paul Hanke and Prof. Eike-Erik Kluge for their continual support.

For the excellent company and, especially towards the end, significant effort spent and outstanding moral support I would like to thank my officemates Christoph Anders, Michael Henke and Felix Müller. Likewise for always enduring my often prevalent incompetence in foosball, despite all the training.

During the last years many people joined and left the KIP particle physics group, too many to name them all. I have to mention Victor Andrei, Andreas Jung and Klaus Urban, though, who especially have made the group a friendly and supportive environment.

Special thanks also go to my family and friends. First of all to Wilhelm Seifarth, my granddad, for being a role model for all my life. Likewise to my parents, without them none of this would have been possible.

My last, but dearest thanks go to Heidrun. She has my unending gratitude for all her support, her tolerance, and last but not least just being herself. She is the joy of my life.